Small Molecule Heterojunction Solar Cells Employing Mixed Donor-Acceptor Active Regions and Buffer Layers

by

Xin Xiao

A dissertation submitted in partial fulfillment
of the requirements for the degree of
Doctor of Philosophy
(Electrical Engineering)
in The University of Michigan
2015

Doctoral Committee:

Professor Stephen R. Forrest, Chair
Professor L. Jay Guo
Professor Jamie D. Phillips
Associate Professor Max Shtein

ACKNOWLEDGMENTS

First and foremost, my deepest appreciation goes to my advisor Professor Stephen Forrest for his guidance through my entire research at UM. I am very fortunate to have an opportunity to conduct my doctoral research in such a wonderful group with a perfect combination of freedom and guidance. Your enthusiasm on science, the highest standards of research, great scientific taste and sense of humor inspire me to achieve the level that I could never dream before and will definitely have an intense impact in my future career. Thank you, sir, for everything.

I would also like to thank other committee members, Professor Jay L. Guo, Professor Jamie D. Phillips, Professor Max Shtein, for their time, encouragement and insightful suggestions on my thesis.

I always owe a lot to my colleagues at OCM for their help and friendship. I feel honored to work with so many talented scholars. I would like to thank Ning Li, Jeramy Zimmerman, Guodan Wei and Brian Lassiter who served as my mentors at my early stage in the group and taught me a lot about organic photovoltaics both in theory and experiment. I am especially indebted to Kyusang Lee who is not only my best friend in graduate school but also helps me a lot in research. I also benefit significantly from the other OCM members, particularly Yifan Zhang, Kyle Renshaw, Greg Mcgraw, Michael Sloosky, Xiaoran Tong, Cedric Collins, Xiaozhou Che, Xiao Liu, Anurag Panda, Jaesang Lee, Quinn Burlingame, Kevin Bergemann,

TABLE OF CONTENTS

CHAPTER

LIST OF FIGURES

x

LIST OF TABLES

LIST OF APPENDICES

ABSTRACT

Organic photovoltaic (OPV) cells are considered as a promising candidate for renewable energy sources of the next generation due to their advantages of low cost, light weight and mechanical flexibilities. This dissertation targets on the development and understanding of high efficiency and large area small molecule OPV cells with mixed donor-acceptor heterojunctions (HJ) and buffer layers.

The first part of this thesis focuses on a mixed HJ OPV cell employing tetraphenyldibenzoperiflanthene (DBP) and C_{70} as donor and acceptor. We systematically analyze loss mechanisms inside the mixed HJ cell. A hybrid planar-mixed heterojunction (PM-HJ) structure is employed to reduce exciton quenching at the MoO_3/organic interface, whereas an exciton blocking/electron conducting buffer comprised of wide energy gap molecules and C_{60} is implemented to suppress bimolecular recombination and exciton-polaron quenching. The optimized DBP:C_{70} PM-HJ cell achieves power conversion efficiency (PCE) = 8.1 ± 0.4 % under simulated AM 1.5G illumination at one sun intensity.

In the second part of this thesis, we employ DBP:C_{70} mixed HJ as a blue-green absorbing sub-cell in the tandem paired with various near infrared(NIR)-absorbing sub-cells. A solution-processed blended functionalized squaraine/C_{70} bilayer HJ is employed as a NIR-absorbing sub-cell. To further enhance the absorption in NIR, we use a vacuum-deposited DTDCTB:C_{60} PM-HJ in the tandem, leading to PCE = 10.0 ± 0.2%. Furthermore, we develop triple and four-

junction OPV cells to enable the photon harvesting at the second order interference maxima, resulting in a significant improvement in *EQE* and *PCE*. In addition, we develop inverted semitransparent OPV cells using both mixed and PM-HJ structures along with a semitransparent tandem cell.

Finally, we study the scalability of OPV cells. Multi-junction OPV cells exhibit reduced loss in *PCE* for large area devices compared to single junction cells due to the lower current and higher voltage during operation. We further fabricate organic solar modules consisting of 25, 1 cm^2 discrete multi-junction cells connected in a series-parallel circuit configuration with a yield of 100% for discrete cells and a deviation of *PCE* from cell to cell of <10%.

Chapter I

Introduction to Organic Photovoltaics

Tremendous effort has been devoted to the development of renewable energy since the shortage of energy has become a critical issue for our well-being. Organic photovoltaic (OPV) cells are considered as a promising candidate of renewable energy sources for the next generation due to their low-cost, light weight and mechanical flexibility. Since the donor/acceptor heterojunction was first introduced in OPV cells by Tang [1] three decades ago, significant progress has been made in the field of OPVs[2-6]. The power conversion efficiency (*PCE*) has soared from less than 1% in the early days[1], up to >10%[7-11] very recently, whereas the operational lifetime of OPV cells has been extended from a few hours to several years of the state-of-the-art OPV cells[12-16]. Also, the size of OPV cells has increased from ~1 mm^2 for discrete cells in the lab, to the module scale for practical applications[13, 17-19]. This chapter aims to lay down the fundamentals of these advances. We begin with a general introduction of organic semiconductors. Next, we present working principles of OPV cells with an emphasis on the differences with their inorganic counterparts. Then we discuss a variety of device architectures for OPV cells. Finally, we summarize the latest progress in the field of small molecule OPV cells followed by an outline of this thesis.

1.1 Fundamentals of organic semiconductors

Organic molecules consist of carbon, hydrogen and other elements, e.g. N, O and so on. Carbon, a basic element of organic molecules, has a ground state electronic configuration of $1s^2 2s^2 2p^2$. While it is likely for the four outer shell electrons to be mixed to form four degenerate hybrid sp^3 orbitals, it is also possible for three electrons to form degenerate hybrid sp^2 orbitals[20]. Coplanar chemical bonds are formed by the hybrid sp^2 orbitals and the fourth one is perpendicular to the sp^2 plane, forming the so-called π-bond. The fourth electron associated with a π-bond, the "π-electron", is more delocalized than the other electrons and has profound impact on the physical properties of conjugated organic molecules. In this thesis, we focus on small molecule compounds characterized by a conjugation on the π-electron systems.

While the atoms in organic molecules are connected by covalent bonds (the intramolecular interaction), the molecules in organic solids are held together by the van der Waals force (the intermolecular interaction) which can be approximately described by a Lennard-Jones potential:

$$V(r) = 4\varepsilon[(\frac{\sigma}{r})^{12} - (\frac{\sigma}{r})^6],$$
(1.1)

where V is the potential, ε is the depth of the potential well, r is the distance between two molecules, σ is the finite distance at which the intermolecule potential is zero.

Compared to covalent bonds between atoms in inorganic semiconductors (e.g. Si, Ge), the intermolecular interaction between molecules in organic solids is much weaker. Therefore, instead of band transport in inorganic semiconductors, charge carriers hop between adjacent molecules in organic solids, resulting in significant lower charge carrier mobilities, usually on the order of 10^{-6} to 10^{-2} cm^2/(V·s), compared to their inorganic counterparts, ~10 to 10^3

cm^2/(V·s). The weak intermolecular interaction in organic semiconductors also leads to a weak electric field screening and low dielectric constants, usually between 3 to 6[2, 4]. Therefore, excitons, the electron-hole pairs bound by the Coulomb interaction, in organic solids have a large binding energy on the order of 0.1 to 1 eV, significantly higher than the thermal energy at room temperature (k_BT = 25.8 meV). These so-called Frenkel excitons, with a small radius ($\sim$ 0.5 nm) as schematically shown in Fig. 1.1, cannot dissociate into free charge carriers at room temperature owing to their large binding energy. In contrast, excitons in inorganic semiconductors, so-called Wannier-Mott excitons, have a large radius (~10 nm) and small binding energy ($<< k_BT$) (see Fig. 1.1), which can easily lead to a dissociation into free charge carriers at room temperature. In addition to these two types of excitons, there is an intermediate state, the charge-transfer exciton (CT exciton), which usually extends between two or more adjacent molecules as shown in Fig. 1.1.
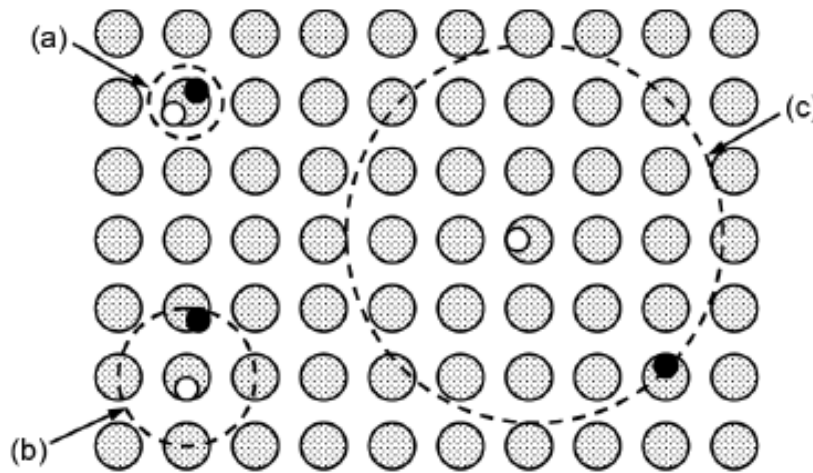
Figure 1.1 Schematic diagram of (a) Frenkel exciton; (b) charge transfer exciton; (c) Wannier-Mott exciton. [20]

3

1.2 Working principles of OPV cells

1.2.1 Photocurrent generation in OPV cells

Due to the excitonic nature of organic semiconductors, the working principle of OPV cells is significantly different from inorganic solar cells. In general, there are four consecutive steps for photocurrent generation in OPV cells as shown in Fig. 1.2 [2, 21]: (a) exciton generation by absorbing photons (η_A) ; (b) exciton diffusion to the donor/acceptor interface (η_{ED}); (c) exciton dissociation into free charge carriers (η_{CT}); (d) charge extraction by electrodes (η_{CC}). The external quantum efficiency (*EQE*), defined as the ratio of charge carriers collected at the electrodes to the incoming photons, is a product of the efficiencies of each step, namely, $\eta_{EQE} = \eta_A \times \eta_{ED} \times \eta_{CT} \times \eta_{CC}$.
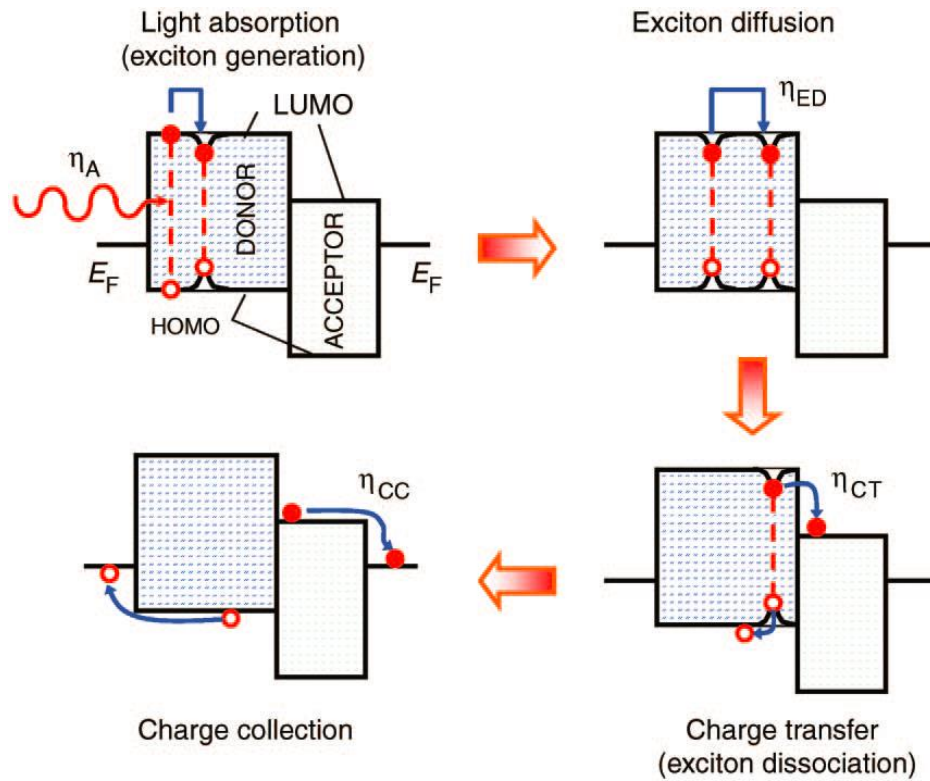
Figure 1.2 Schematics of four steps for photocurrent generation in an OPV cell. [21]

For planar OPV cells consisting neat donor and acceptor layers as photoactive regions, there is a tradeoff between the exciton diffusion length, L_D, and the absorption length, $1/\alpha$, where α is the absorption coefficient. The absorption coefficient of a photoactive layer with thickness, t, is given by $\eta_A = 1 - e^{-\alpha \cdot t}$ while the exciton diffusion efficiency $\eta_{ED} = e^{-t/L_D}$. L_D of almost all the organic molecules used in OPV cells is usually ~10 nm [2, 21] which is much smaller than the absorption length, on the order of a few 100 nms. Increases in layer thickness of the photoactive region larger than L_D leads to increased η_A but decreased η_{ED}, forming an 'exciton bottleneck' and, ultimately, limiting the device efficiency.

On the other hand, in a donor/acceptor mixed heterojunction structure[22], donor and acceptor molecules are mixed together with optimal domain sizes of $\sim L_D$ so that photogenerated excitons can efficiently diffuse to the donor/acceptor interface for dissociation. Thus, the thickness of donor/acceptor mixture is not limited by L_D but an increase in the thickness of photoactive layers results in a reduction in the charge collection efficiency, η_{CC}, due to the lack of charge carrier transport paths. We will further discuss the device architectures of OPV cells in detail in section 1.3.

1.2.2 Current density-voltage characteristics of OPV cells

The current density-voltage (J-V) characteristics of inorganic solar cells are usually described by Shockley equation[23]:

$$J(V) = J_S \left[\exp\left(\frac{V_a - J R_S}{\frac{n k_B T}{q}} \right) - 1 \right] - J_{ph}, \qquad (1.2)$$

where J_S is the saturation current, R_S is the series resistance, k_B is the Boltzman constant, T is the temperature, n is the ideality factor, q is the electronic charge and J_{ph} is the photocurrent. Due to the excitonic nature of organic semiconductors, Giebink *et al.* [24-25] developed a modified ideal diode equation to describe OPV cells:

$$J(V) = J_{sD}\left[\exp\left(\frac{V-JR_S}{\frac{n_D k_B T}{q}}\right) - \frac{k_{ppd}}{k_{ppd,eq}}\right] + J_{SA}\left[\exp\left(\frac{V-JR_S}{\frac{n_A k_B T}{q}}\right) - \frac{k_{ppd}}{k_{ppd,eq}}\right] - J_{ph}, \qquad (1.3)$$

where $J_{sD(A)}$ is the saturation current on the donor (acceptor) side, $n_{D(A)}$ is the ideality factor associated with trap-limited recombination in the donor (acceptor) side, k_{ppd} is the polaron pair dissociation rate, $k_{ppd,eq}$ is the polaron pair dissociation rate at equilibrium, and J_{ph} is the photocurrent. In this model, polaron pairs (PP) can either recombine and relax to the ground state or dissociate into free charge carriers at the donor/acceptor interface as shown in Fig. 1.3. The dynamics of polaron pairs at the donor/acceptor interface is of critical importance to determine the device performance of OPV cells.
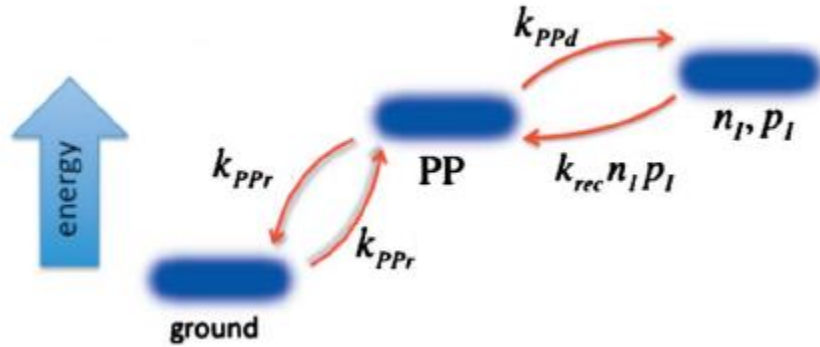
Figure 1.3 Schematics of polaron pair recombination and dissociation process inside OPV cells. [24]

1.2.3 Working principle of tandem OPV cells

Single junction OPV cells usually suffer from narrow absorption bands and thermalization loss. Different from inorganic semiconductors which absorb all photons with energy higher than the bandgap (such as Si, see Fig. 1.4 (a)), organic semiconductors usually possess narrow absorption bands (see Fig. 1.4(a)) due to discrete energy levels of organic molecules. Moreover, there is an energy loss when photons with higher energy than the optical gap relax to their lowest excited states, so-called thermalization loss, as schematically shown in Fig. 1.4 (b).
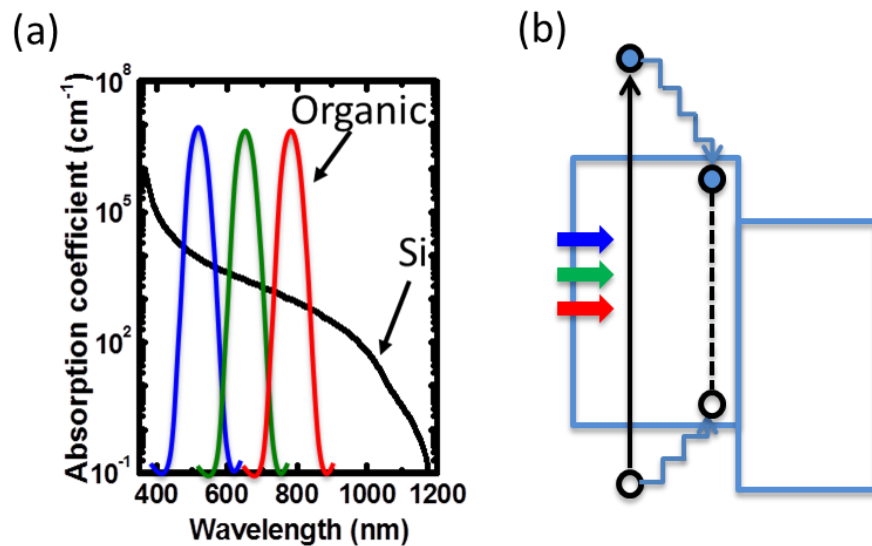
Figure 1.4 (a) Comparison of absorption spectra of organic and inorganic semiconductors; (b) schematic diagram of thermalization loss for single junction OPV cells.

To overcome these limits of single junctions, tandem and multi-junction structures have been developed for high efficiency OPV cells. In a tandem structure, two sub-cells with different absorption spectra are connected in series as shown in Fig. 1.5. Ideally, the absorption spectra of two sub-cells should cover a broad range of the solar spectrum with minimal absorption overlap.

Under operation, two sub-cells need to generate the same amount of current for charge conservation in the circuit. The charge generation layers (CGL) which connect two sub-cells also play an important role to determine the device performance of tandem cells. In the CGL, holes generated in the front sub-cell recombine with electrons from the back sub-cell such that the voltages of two sub-cells can sum to that of the tandem (see Fig. 1.5). An ideal CGL should be electrically lossless so that the open-circuit voltage (Voc) of the tandem cell equals to the sum of that of two sub-cells, and also highly transparent in the visible and near-infrared(NIR) spectral regions to minimize the optical loss.
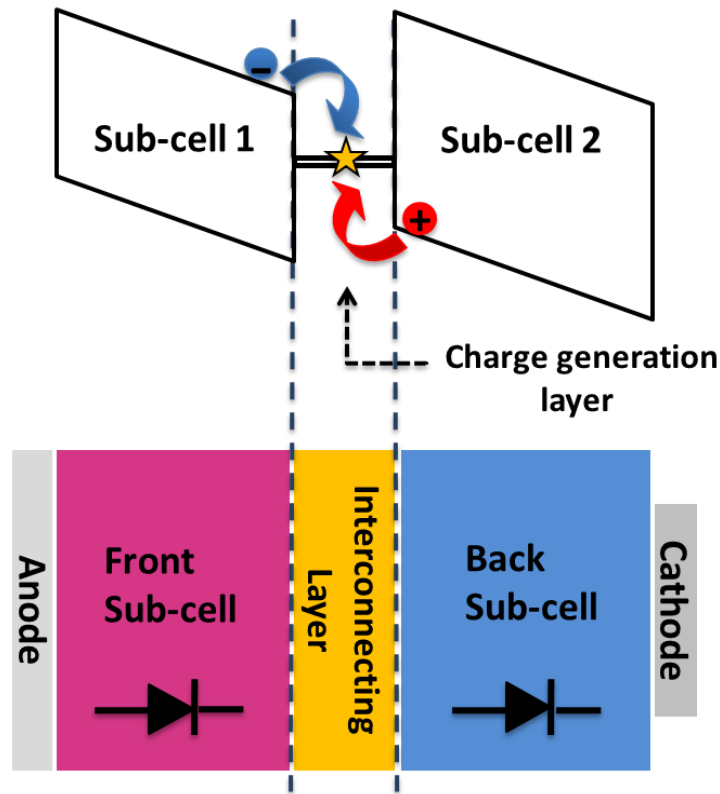
Figure 1.5 Working principle of a tandem OPV cell. (Top: schematic diagram of energy levels in a tandem cell; bottom: the device structure for a tandem cell)

1.3 Device architectures of OPV cells

An OPV cell consists of photoactive layers sandwiched by two electrodes, typically one semitransparent electrode to transmit light, such as indium tin oxide (ITO), and another low-work-function metal, such as Al. In general, there are two types of device architectures for small molecule OPVs, namely, planar and mixed heterojunction (HJ) structures as schematically illustrated in Fig. 1.6.
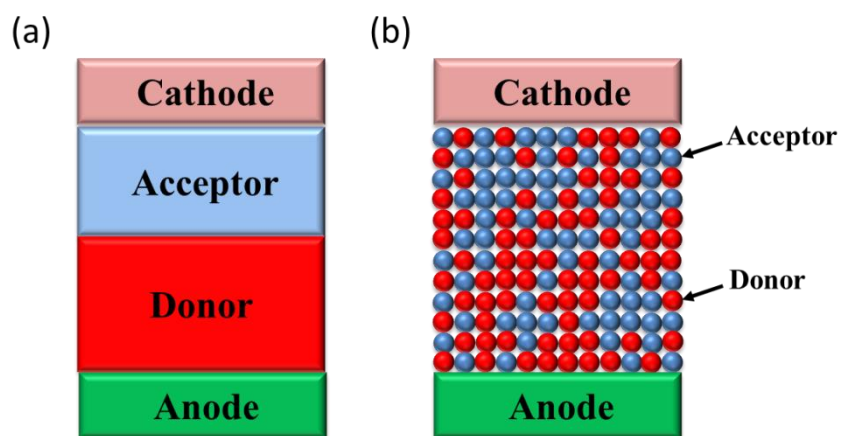
Figure 1.6 Schematic illustration of two types of device architectures for OPV cells: (a) planar HJ; (b) mixed HJ.

In a planar HJ OPV cell, the photoactive region consists of neat donor and acceptor layers with the layer thicknesses of $\sim L_D$ such that photogenerated excitons in the organic photoactive layers can efficiently diffuse to the donor/acceptor interface for dissociation. Since L_D of almost all the organic molecules used in OPV cells are on the order of ~ 10 nm, planar HJ OPV cells usually suffers from limited light absorption due to thin photoactive layers and limited donor/acceptor interface.

Several strategies have been developed to improve the device performance of planar HJ cells. For instance, thermal annealing has been applied on the functionalized squaraine, 2,4-bis [4-(N-phenyl-1-naphthylamino)-2,6-dihydroxyphenyl] squaraine (1-NPSQ), thin films to increase surface roughness and improve the crystallinity of the 1-NPSQ donor layers leading to enhanced short-circuit current density (J_{SC}) and fill factor (*FF*) as shown in Fig. 1.7[26]. Furthermore, Zimmerman *et al.* [27] developed a solvent annealing method of the entire donor/acceptor layers to preserve the donor/acceptor interface while enhancing the crystallinity of donor/acceptor layers, resulting in a significant improvement of photocurrent without reducing V_{OC} as shown in Fig. 1.8.
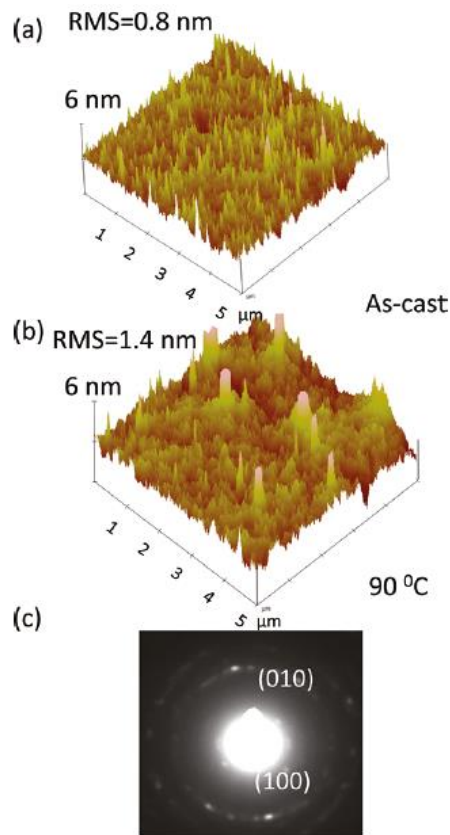
Figure 1.7 Atomic force microscopy (AFM) profiles of: (a) as-cast; (b) thermal annealed 1-NPSQ films. The RMS roughnesses for (a) and (b) are 0.8 nm and 1.4 nm, respectively. (c) Selected area electron diffraction (SAED) pattern of thermal annealed 1-NPSQ films. [26]
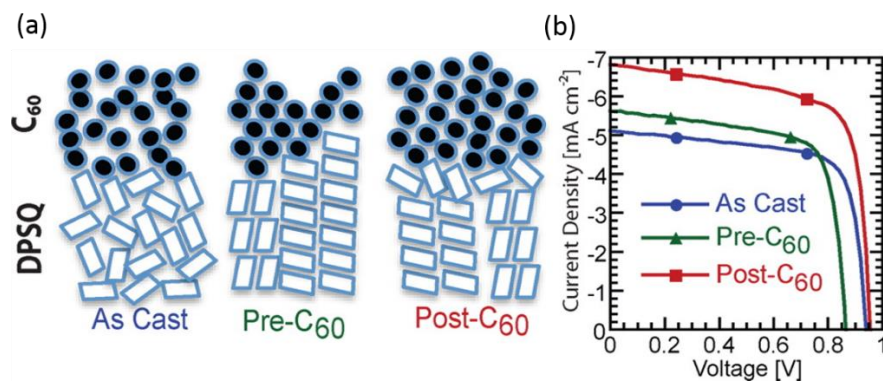
Figure 1.8 (a) Schematic illustration of DPSQ and C_{60} with different processing conditions; (b) *J-V* characteristics of DPSQ/C_{60} bilayer HJ cells with different processing conditions. [27]

In contrast to planar HJs, mixed HJ OPV cells possess a blend of donor and acceptor for the photoactive region, as shown in Fig. 1.6(b). An extensive donor/acceptor interface is present in the photoactive region of the mixed HJ cell for efficient exciton dissociation. In an ideal case, the scales of phase segregation in the donor and acceptor domains should be on the order of L_D so that all the photogenerated excitons in the domains can efficiently diffuse to a donor/acceptor interface for dissociation. Thus, the mixed HJ overcomes the exciton bottleneck of the planar HJ, but usually suffers from low charge collection efficiency due to the lack of continuous paths for charge extraction which ultimately leads to high resistance and, therefore, low *FF*.

To improve charge collection while maintaining high absorption, new architectures based on mixed HJs have been developed over the past few years. Xue *et al.* developed a planar-mixed heterojunction (PM-HJ) structure consisting of a donor/acceptor mixed layer sandwiched between neat donor and acceptor layers (see Fig. 1.9)[28]. The thicknesses of the neat donor and acceptor layers are within L_D of the donor and acceptor molecules. The reduction of donor/acceptor mixed layer thickness improves the charge collection efficiency while the neat donor and acceptor layers compensate the light absorption which, ultimately, increases the *PCE*.
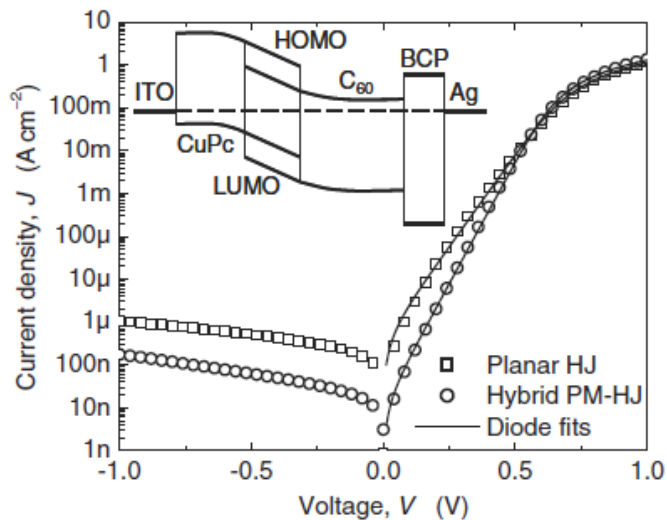
Figure 1.9 *J-V* characteristics of a planar HJ and a PM-HJ OPV cell. The solid lines represent diode fits for *J-V* characteristics. *Inset*: schematic diagram of energy levels for a PM-HJ cell.[28]

An alternative to improve charge collection in the mixed HJ is to employ a graded donor/acceptor mixed layer as the photoactive region. In a graded HJ, donor and acceptor compositions vary across the photoactive region. Pandey *et al.*[29] demonstrated that the continuously graded HJ using boron subphthalocyanine chloride (SubPc) and C_{60} form a donor/acceptor network for optimized exciton and charge carrier transport, leading to improved J_{SC} and *FF* compared to the uniformly mixed HJ .

In addition to the photoactive regions, buffer layers also play an important role in determining the device performance. The buffer layers usually have multiple functions, such as blocking excitons to prevent exciton quenching at the organic/metal interface, protecting organic photoactive layers from the damage of metal deposition, and acting as an optical spacer to optimize the optical field inside the organic photoactive region. There are, in general, three types of buffer layers as shown in Fig. 1.10. The first type consists of wide energy gap organic molecules, such as bathocuproine (BCP), commonly used in OPV cells. The charges are

12

conducted through defect states induced by the damage of metal deposition as shown in Fig. 1.10(a).[30] The second type consists of organic molecules with low highest occupied molecular orbital (HOMO) energies, such as tris-(acetylacetonato) ruthenium (III) [Ru(acac)₃], so that electrons from the acceptor can recombine with holes transported through the HOMO energy of Ru(acac)₃ (see Fig. 1.10(b)).[31] In the third type of buffer, the lowest unoccupied molecular orbital (LUMO) energies of organic molecules are aligned with that of the acceptor so that electrons can directly transport from the acceptor to the cathode without experiencing large energy barriers, as shown in Fig. 1.10(c).[32]
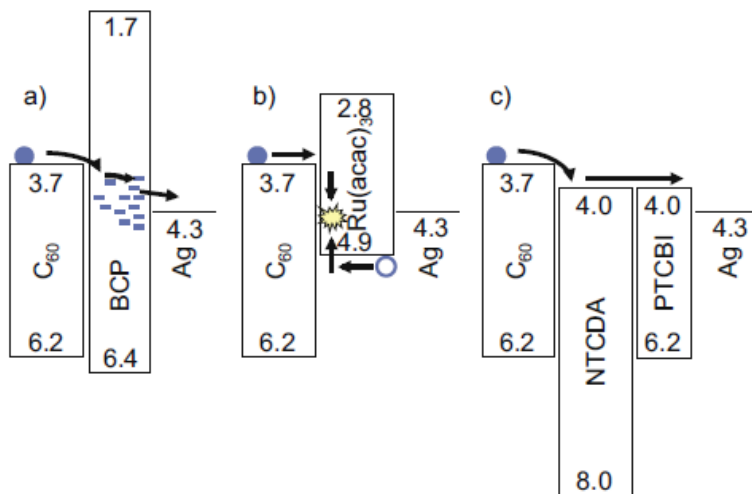
Figure 1.10 Energy level diagrams of three types of buffers with different charge transport mechanisms: (a) electron-conducting defect states induced by the metal deposition; (b) hole-electron recombination; (c) electron transport through LUMO of buffer layers.[32]

1.4 Latest developments in small molecule OPV cell technology

Small molecule OPV cells have attracted considerable research interest owing to their advantages of ultra-high material purity, ease of processing, and minimal batch-to-batch

variation in device performance. Efficiencies of small molecule OPV cells have increased rapidly over the past few years with extensive development on new materials and device structures. The device performances of state-of-the-art small molecule OPV cells are comparable or even better than their polymer counterparts.

1.4.1 Latest developments in single junction small molecule OPV cells

New donor molecules are a key to achieve high efficiency small molecule OPV cells. Promising donor molecules should meet three criteria: (a) high hole mobility; (b) deep HOMO level; (c) large absorption coefficient with a broad coverage of the solar spectrum. Tremendous effort has been devoted on the development of novel donor materials for high efficiency small molecule OPV cells.

Vacuum-deposited small molecule donors are of critical importance for high efficiency OPV cells. Hirade *et al.* employed tetraphenyldibenzoperiflanthene (DBP) as a donor molecule (see Fig. 1.11) paired with C_{60} as an acceptor in a planar HJ cell.[33] DBP has a HOMO level of -5.5 eV [34], relatively high hole mobility of $\sim 10^{-4}$ $cm^2/(V \cdot s)$ [33], and large absorption coefficient with a peak value of 4.2×10^5 cm^{-1} at a wavelength of $\lambda = 610$ nm. These superior physical properties of DBP make it a promising donor molecule for blue-green absorption. Using an exciton blocking layer at the anode, exciton quenching is reduced leading to improved J_{SC} and *FF*. *PCE* increases from $3.88 \pm 0.06\%$ for the cell without the blocking layer to $5.04 \pm 0.21\%$ for the cell with the blocking layer. In this thesis, we will use DBP as a primary donor for mixed and PM-HJ OPV cells.
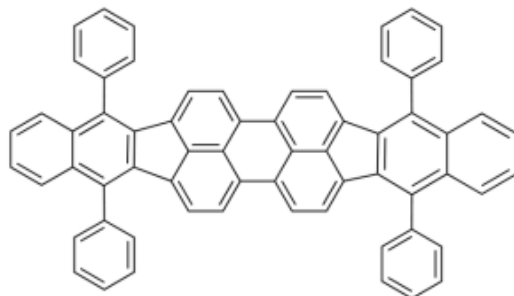
Figure 1.11 Molecular formula of DBP.

Fitzner *et al.* also developed a series of vacuum-deposited blue-green-absorbing donors, methyl-substituted dicyanovinyl-capped acceptor-donor-acceptor-type quinquethiophenes (DCV5T-Me, see Fig. 1.12(a)).[35] In particular, DCV5T-Me 3 exhibits a broad absorption spectrum as shown in Fig. 1.12 (b). The photoactive region of an optimized cell consists of a 30 nm thick mixture of DCV5T-Me 3:C_{60} at a 2:1 vol. ratio resulting in a *PCE* = 6.9%.
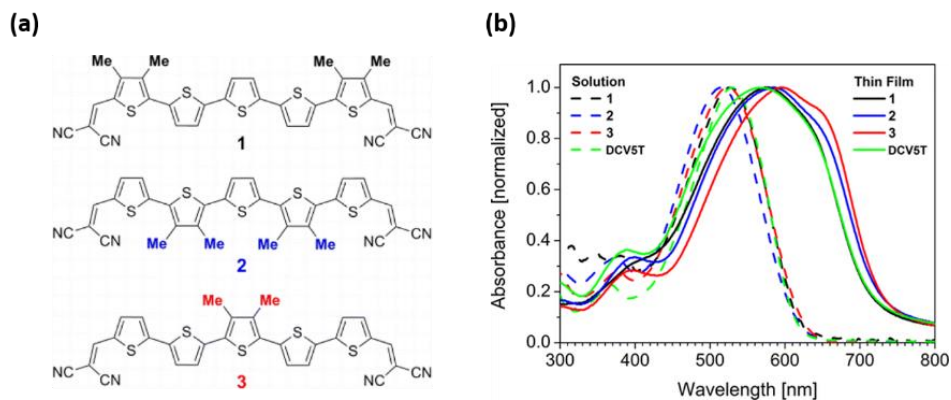
Figure 1.12 (a) Molecular formulae of DCV5T-Me 1-3. (b) Normalized absorption spectra of DCV5T-Me 1-3 in CH_2Cl_2 solution and thin films. [35]

In addition to blue-green-absorbing donors (e.g. DBP, DCV5T), vacuum-deposited donors with the absorption extended to the NIR spectral range also attract considerable interest not only for single junctions but also tandem/multi-junction OPV cells. Lin *et al.* demonstrated a donor-acceptor-acceptor-type donor molecule, 2-((7-(5-(dip-tolylamino) thiophen-2-yl)benzo

[c][1,2,5]thiadiazol-4-yl)methylene)malononitrile (DTDCTB), with the absorption extended to the wavelength of 900nm as shown in Fig. 1.13.[36]   A vacuum-deposited PM-HJ cell using DTDCTB as donor and C_{70} as acceptor achieves a *PCE* of 5.8% under simulated AM 1.5G illumination at one sun intensity. Furthermore, the same group modified the DTDCTB molecule and obtained a new molecule DTDCTP to further improve the V_{OC}, leading to a higher *PCE* = 6.4%.[37]

(a)   **(b)**
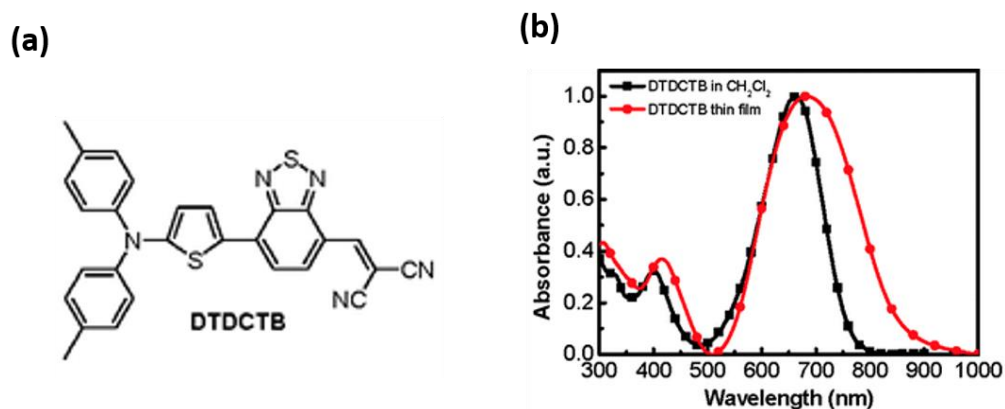
Figure 1.13 (a) Molecular formula of DTDCTB; (b) normalized absorption spectra of DTDCTB in CH_2Cl_2 and DTDCTB thin film. [36]

In addition to vacuum-deposited small molecule donors, considerable progress has been made on the development of solution-processed donor molecules over the past few years. Sun *et al.* report a solution-processed small molecule OPV cell based on the donor, 5;50-bisf(4-(7-hexylthiophen-2-yl)thiophen-2-yl)-[1,2,5]thiadiazolo[3,4-c]pyridineg-3;30-di-2-ethylhexylsilylene-2;20-bithiophene, DTS(PTTh2)2.[38] A small amount of solvent additive, 1,8-diiodooctane (DIO), is used to slow down the solvent evaporation process for the formation of ideal donor and acceptor domains, leading to *PCE* of 6.7% under simulation AM 1.5G illumination at one sun intensity. Furthermore, the same group synthesized a modified donor, 7,7′-(4,4-bis(2-ethylhexyl)-4H-silolo[3,2-b:4,5-b′]dithiophene-2,6-diyl)bis(6-fluoro-4-(5′-hexyl-

16

[2,2′-bithiophen]-5-yl)benzo[c][1,2,5] thiadiazole), p-DTS (FBTTh$_2$)$_2$, with deeper HOMO level and improved hole mobility.[39] They inserted a ZnO layer acting as both an optical spacer and a hole blocking layer between the photoactive layer and cathode to improve the charge collection and reduce the charge recombination. This resulted in *PCE* = 8.9% for an optimal OPV cell.[40]

On the other hand, Li *et al.* developed a Rhodanine-based small molecule donor, (5Z,5′Z)-5,5'-((3,3'''',3'''''',3'''''''',4',4''-hexaoctyl-[2,2':5',2'':5'',2''':5''',2'''': 5'''',2'''''':5'''''', 2''''''''-sepithiophene]-5,5''''''''diyl)bis(methanylylidene))bis(3-ethyl-2-thioxothiazolidin-4-one), DERHD7T (see Fig. 1.14 (a)), with a HOMO level of -5.2 eV, a hole mobility of 1.5×10^{-4} cm^2/(V·s) and an absorption peak of 7.2×10^4 cm^{-1} at the wavelength of λ = 618 nm.[41] Paired with PC$_{70}$BM as an acceptor, the optimized OPV cell achieves *PCE* = 6.1% limited by a low *FF* of 47%. Very recently, the DERHD7T molecule was modified by using a dicyanomethylene group to replace the thio group and a new donor molecule, DRCN7T, was obtained as shown in Fig. 1.14(a).[42] The DRCN7T molecule exhibits red-shifted absorption spectrum, improved hole mobility and similar HOMO level compared to the previous donor. Using thermal annealing to prompt the phase separation, the optimal OPV cell achieves a *PCE* = 9.30% with a V_{OC} = 0.91 V, J_{SC} = 14.87 mA/cm^2 and *FF* = 68.7% (see Fig. 1.14 (b)).
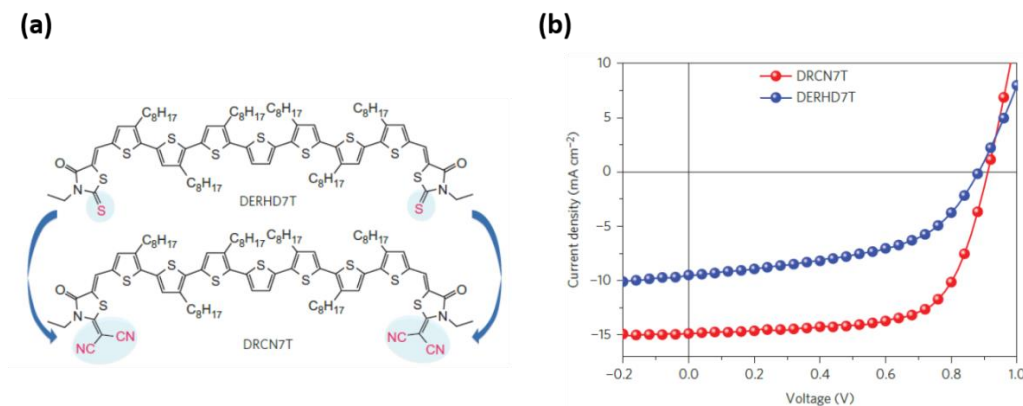
Figure 1.14 (a) Molecular formulas of DERHD7T and DRCN7T; (b) *J-V* characteristics of DERHD7T and DRCN7T-based OPV cells under simulated AM 1.5G illumination at one sun intensity. [42]

In addition to the extensive exploration of new materials, device architectures have also been developed for high efficiency OPV cells. One promising architecture is a multi-layer donor cascade structure in which energy transfer occurs across a stack of donors with monotonically decreased energy gaps. Excitons generated in each donor layer are transferred to the donor/acceptor interface for dissociation via the Förster energy transfer process. Griffith *et al.* demonstrated an efficient energy cascade structure using multiple donors paired with C_{60} as the acceptor.[43] Three donor molecules, namely, diphenyltetracene (DPT), rubrene (RUB), tetraphenyldibenzoperiflanthene (DBP), with monotonically decreasing optical gaps (see Fig. 1.15) are employed to form the energy cascade. The DPT/RUB and RUB/DBP interfaces block excitons while the DBP layer contributes most of the photocurrent and determines the V_{OC}. The optimized DPT/RUB/DBP/C_{60} cascade cell achieves $PCE = 7.1 \pm 0.4$ % significantly higher than that of cells with only a single donor. Likewise, Cnops *et al.* demonstrated a three-layer structure consisting of one donor and two non-fullerene acceptors in an energy cascade architecture.[44] Excitons generated in the remote acceptor are transferred to the adjacent acceptor layer via the

18

Förster energy transfer and dissociate at the donor/acceptor interface. The optimal cascade cell reaches $PCE = 8.4$ % with a high V_{OC} close to 1V.

Figure 1.15 (a) Molecular formulas of three donors; (b) Schematic diagram of energy levels of photoactive layers in an energy cascade structure. [43]

1.4.2 Latest developments in tandem/multi-junction small molecule OPV cells

Small molecule tandem cells have attracted considerable research interest in recent years due to their reduced thermalization loss along with a broad coverage of solar spectrum. The challenges of tandem OPV cells, however, are complicated optical designs and fabrication processes. Cheyns *et al.* developed an OPV tandem by stacking two planar HJ cells absorbing in different spectral regions with a broadened coverage of the solar spectrum.[45] Chloroboron subnaphthalocyanine (SubNc)/C_{60} planar HJ is employed as a NIR-absorbing subcell, whereas SubPc/C_{60} planar HJ absorbs in blue-green spectral region. The recombination zone consists of a multi-layer structure of 3,4,9,10-perylenetetracarboxylic bis-benzimidazole (PTCBI) (5 nm)/Ag(0.1 nm)/MoO$_3$(5 nm). The tandem cell has a complimentary coverage of the solar spectrum ranging from $\lambda = 400$ nm to 800 nm with a $PCE = 5.15\%$. On the other hand, Riede *et al.* stacked two vacuum-deposited mixed HJs for a tandem with a thick transparent optical spacer

19

between two sub-cells to fully absorb photons at each absorption maxima.[46] The optimized tandem achieves an efficiency of 6.07%.

Lassiter *et al.* developed an efficient tandem cell incorporating both solution and vacuum-deposited sub-cells with different absorption spectra.[47] SubPc:C_{60} graded HJ is used as a blue-green-absorbing sub-cell, whereas 2,4-bis[4-(N,Ndiphenylamino)-2,6-dihydroxyphenyl] squaraine (DPSQ)/C_{70} bilayer HJ is employed to harvest photons in NIR as shown in Fig. 16. The optimal tandem achieves $PCE = 6.6 \pm 0.1\%$ with $V_{OC} = 1.97 \pm 0.01$V. Meanwhile, a fully solution-processed small molecule tandem cells was developed by stacking two identical solution-processed small molecule bulk HJ together with a modified PEDOT:PSS as the charge generation layer, resulting in $PCE = 10.1\%$.[48]
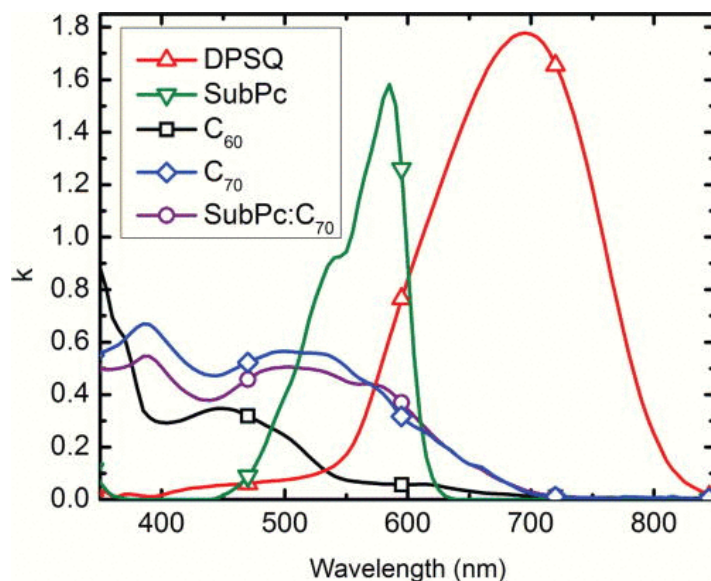
Figure 1.16 Extinction coefficients of donor and acceptor molecules in Ref. [47].

Very recently, triple junction OPV cells have started to attract considerable research interest due to their potential to achieve higher efficiencies. Chen *et al.* demonstrated an inverted triple-junction polymer OPV cell comprised of three sub-cells with different energy gaps.[10]

Three polymers with energy gaps of 1.9 eV, 1.58 eV and 1.4 eV, respectively, were employed in the triple-junction cell to harvest the photons in a broad range of solar spectrum. The optimized triple-junction cell achieves PCE = 11.55 % under 1 sun illumination. Meanwhile, Yusoff *et al.* [11] also developed an inverted solution-processed triple-junction polymer cell incorporating polymer donors with energy gaps ranging from 1.3 eV to 1.82 eV. The interconnecting layer consists of a transparent inorganic/organic mixture to reduce the optical and electrical loss leading to PCE = 11.83 %. In addition, small molecule triple junction cells were developed recently by stacking three identical DCV5T:C_{60} mixed HJ.[49] Due to microcavity effects in the stack, the EQE of each sub-cell, measured under different light bias, is spectrally shifted leading to a broadened coverage of the solar spectrum resulting in PCE = 9.7 %.

1.5 Thesis overview

In this thesis, we focus on the understanding and development of small molecule heterojunction OPV cells employing donor-acceptor mixed active regions and buffer layers. The first part of this thesis investigates the primary loss mechanisms within the mixed HJ cell with solutions provided to reduce these losses. In Chapter 2, we study the exciton dynamics at the MoO_3/organic interface. Due to the exciton quenching at this interface, a PM-HJ structure is employed to reduce the optical power at the interface, leading to an improved internal quantum efficiency (IQE) and, thus, PCE. Chapter 3 studies the bimolecular recombination and exciton-polaron quenching inside the PM-HJ cells. A novel buffer consisting of wide energy gap molecules and C_{60} is adjacent to the cathode to efficiently conduct holes and block excitons, resulting in an significant improvement in FF with PCE = 8.1 ± 0.4 % for an optimized OPV cell.

In the second part of this thesis, we employ DBP:C_{70} PM-HJ as a green-absorbing sub-cell paired with various NIR-absorbing subcells in tandem/multi-junction OPV cells. Chapter 4 presents a blended functionalized squaraine(fSQ)/C_{60} bilayer HJ which is used as a NIR-absorbing sub-cell in the tandem structure. The blend fSQ cell has a broadened coverage of the solar spectrum especially in the NIR, resulting in higher J_{SC}, V_{OC} and PCE than single fSQ donor cells. In Chapter 5, we first demonstrate a tandem cell incorporating blend fSQ/C_{60} bilayer HJ and DBP:C_{70} PM-HJ as sub-cells. To further improve the absorption in NIR, we replace the blend fSQ/C_{60} bilayer HJ with a vacuum-deposited DTDCTB:C_{60} PM-HJ, leading to a significant increase in J_{SC} with a $PCE = 10.0 \pm 0.2$ % for the optimal cell. Furthermore, we develop triple and four-junction structures to harvest photons at the second order optical interference maxima, resulting in a $PCE = 11.0 \pm 0.2$ % and 12.6 ± 0.2 %, respectively. In Chapter 6, we demonstrate inverted semitransparent OPV cells with mixed and PM-HJ structures. The PM-HJ cell shows improved charge extraction compared to the mixed HJ leading an increase in FF and PCE. The optimized DBP:C_{70} PM-HJ cell achieves a $PCE = 3.9 \pm 0.2$% with an average transmission of $\overline{T}$ = 51 ± 2% across the visible. We further develop an inverted semitransparent tandem incorporating two PM-HJ with different absorption spectra. The tandem cell reaches a $PCE = 5.3 \pm 0.3$% with $\overline{T} = 31 \pm 1$% across the visible.

Finally, we investigate the scalability of multi-junction OPV cells. Multi-junction cells exhibit reduced loss in PCE than single junction cells for large area cells due to higher operating voltage and lower current density. Further, we fabricated organic solar modules comprised of 25, 1 cm^2 discrete cells connected in a series-parallel circuit configuration. The module achieves a yield of 100% with a deviation of PCE from cell-to-cell of <10%.

Chapter II

DBP:C$_{70}$ planar-mixed heterojunction OPV cells

In this chapter, we study a hybrid planar-mixed heterojunction (PM-HJ) OPV cell using tetraphenyldibenzoperiflanthene (DBP) and C$_{70}$ with a power conversion efficiency (*PCE*) of up to 6.4 ± 0.3%. Optimized cells consist of a DBP:C$_{70}$ mixed layer at a volume ratio of 1:8 and a 9-nm thick C$_{70}$ cap layer. The external quantum efficiency (*EQE*) in the visible of the PM-HJ cell is up to 10% larger than the mixed-HJ cell that lacks a C$_{70}$ acceptor cap layer. The improvement in *EQE* is attributed to reduced exciton quenching at the MoO$_3$ anode buffer layer surface. This leads to an internal quantum efficiency (*IQE*) > 90% between the wavelengths of λ= 450 nm and 550 nm, suggesting efficient exciton dissociation and carrier extraction in the PM-HJ cell. The power conversion efficiency under simulated AM 1.5G, 1 sun irradiation increases from 5.7 ± 0.2% for the mixed-HJ cell to 6.4 ± 0.3% for the PM-HJ cell, with a short-current density (*J$_{SC}$*) of 12.3 ± 0.3 mA/cm^2, open circuit voltage (*V$_{OC}$*) of 0.91 ± 0.01 V, and fill factor (*FF*) of 0.56 ± 0.01.

2.1 Mixed HJ *vs.* hybrid planar-mixed HJ

To achieve higher efficiencies, limitations imposed by the trade-off between the exciton diffusion length (*L$_D$*) and optical absorption length must be overcome[21]. For this purpose, the

mixed-heterojunction (HJ) consisting of a uniformly blended donor/acceptor photoactive region can promote efficient exciton dissociation owing to close contact between the donor and acceptor molecules[38, 50]. This architecture, however, often suffers from a low fill factor (*FF*).

To circumvent the deficiencies of the mixed-HJ structure, the hybrid planar-mixed-HJ (PM-HJ) consisting of a mixed donor/accepter layer sandwiched between neat donor and acceptor layers with thicknesses ~ L_D, was introduced by Xue, *et al.*[28] The PM-HJ structure can improve the charge collection efficiency by reducing the thickness of the mixed layer while including neat donor and acceptor layers to compensate for the loss of light absorption in the thinner photoactive region. Since the neat layer thicknesses are ~ L_D, excitons can efficiently diffuse to an interface with the mixed region where they dissociate. The PM-HJ has advantages of high absorption, exciton dissociation, and charge collection efficiencies.

2.2 Physical properties of DBP and C_{70}

The donor, DBP [33-34, 51], absorbs from λ= 300 nm to 700 nm, with a peak of 4.2×10^5 cm^{-1} at λ= 610 nm (see Fig. 2.1). Further, it has a high hole mobility [33], ~10^{-4} cm^2/(V·s), a HOMO energy of -5.5 eV [34], and an exciton diffusion length of 16 ± 1 nm measured by spectrally resolved luminescence quenching [52], making it suitable for use with fullerene acceptors. The acceptor, C_{70}, broadly absorbs between λ= 350 nm and 700 nm[53]. Hence, blends of DBP and C_{70} strongly absorb between λ= 350 nm and 700 nm, as shown in Fig. 2.1 for a 1:8 (by volume) mixture.
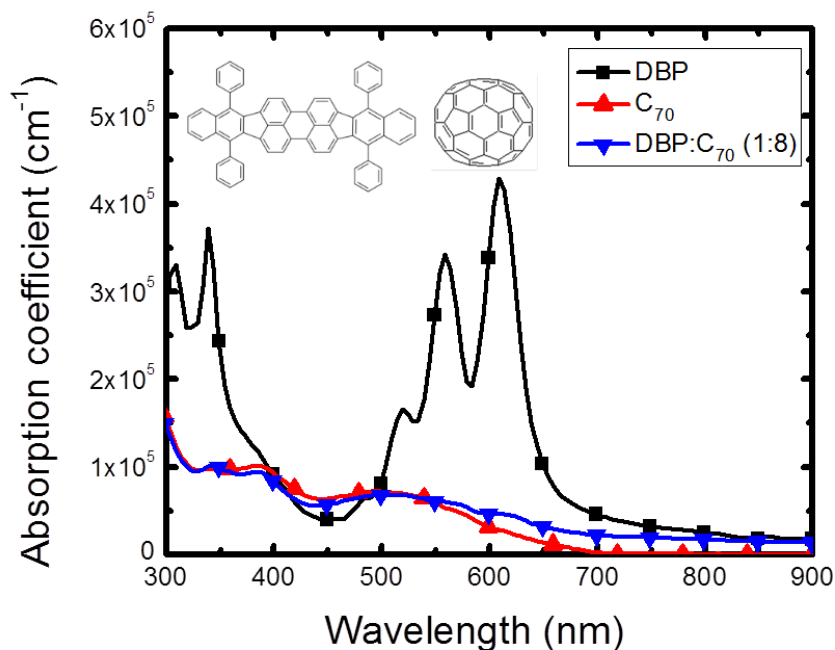
Figure 2.1 Absorption spectra of DBP, C_{70} and a 1:8 DBP:C_{70} mixture. *Inset*: Molecular structural formulae of DBP (left), C_{70} (right).

2.3 Exciton dynamics at MoO₃/organic interfaces

Typically, vacuum thermally evaporated MoO_3 is used in OPVs as an anode buffer layer due to its large work function (which improves the hole collection efficiency at the anode), high transmittance and low series resistance[54-56]. To investigate the influence of MoO_3 on exciton dissociation and, therefore, OPV efficiency, we measured the photoluminescence (PL) excitation spectra of 60 nm-thick DBP and C_{70} films in contact with a 8 nm-thick MoO_3 layer on quartz[52], with results shown in Fig. 2.2. For comparison, 8 nm-thick bathophenanthorline (BPhen) layers are used as exciton blocking layers for both DBP and C_{70}, while C_{60} and N,N'-diphenyl-N,N'-bis(1-naphthyl)-1-1'biphenyl-4,4'diamine (NPD) are employed as exciton quenching layers for DBP and C_{70}, respectively. All films are capped with a 10 nm-thick BPhen

25

exciton blocking layer. The PL spectra of DBP and C_{70} films are measured with illumination through the glass substrate and excited at wavelengths of $\lambda = 530$ nm and 460 nm, respectively. The MoO_3/DBP sample has a PL intensity comparable to that of a quenching C_{60}/DBP interface. Similarly, the MoO_3/C_{70} interface has slightly higher PL intensity than that of the quenching NPD/C_{70} sample. In both cases, their PL intensities are significantly reduced compared to those employing the blocking BPhen/C_{70} and BPhen/DBP interfaces. Because the polarity of the MoO_3-organic junctions is opposite that of the DBP-C_{70} junction, this exciton quenching will always harm the device performance even if the junction were dissociating, as opposed to quenching, excitons. These results provide striking evidence that MoO_3 quenches rather than blocks excitons, as previously expected and will be harmful to device performance[57-59].
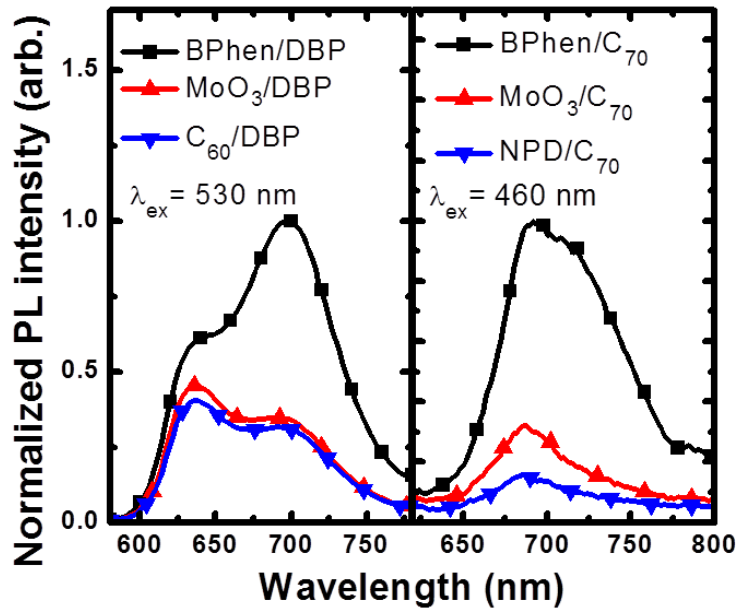
Figure 2.2 Photoluminescence (PL) excitation spectra of DBP (left) and C_{70} (right) films with MoO_3, exciton blocking (BPhen) and quenching (C_{60}, NPD) layers. The excitation wavelengths (λ_{ex}) are indicated. Note that the PL intensities using MoO_3 are similar to those employing the quenching materials, C_{60} and NPD, and are much less than interfaces employing the blocking material, BPhen.

2.4 Optical field simulation for mixed HJ and PM-HJ

Due to the high concentration of C_{70} in the mixed layer (see below), the extensive C_{70} domains that form a partially mixed heterogeneous region analogous to a bulk heterojunction found in polymer-based cells are expected to directly contact the MoO_3. Hence, excitons generated close to the MoO_3 interface can either quench at the MoO_3/organic interface, or dissociate at the donor/acceptor interface (see the inset of Fig. 2.3). To calculate the spatial distribution of the absorbed optical power in the layer stack, we employ the transfer matrix method [2, 60] within a mixed-HJ structure of ITO/MoO_3(10 nm)/DBP:C_{70} (54 nm, 1:8 by vol.)/BPhen(8 nm)/Al (100 nm) using optical constants measured by variable angle spectroscopic ellipsometry. In Fig. 2.3, we show that the absorbed optical power in the mixed-HJ cell has a maximum located at ~12 nm from the MoO_3 surface or ~1.5× L_D of C_{70} (8.0 ± 0.8 nm)[61]. This suggests that a significant number of excitons may indeed be quenched at the MoO_3/organic interface.

Preliminary work showed that OPV devices with more than ~54 nm of mixed DBP:C_{70} layer have a reduced fill factor and efficiency. Thus, to reduce the absorbed optical power near the MoO_3/organic interface, we introduce a neat C_{70} layer between the DBP:C_{70} mixed layer and cathode buffer layer to increase the thickness of the active region. The optimal thickness of the C_{70} layer is expected to be ~L_D, in which case excitons generated within the C_{70} layer can efficiently diffuse to the interface with the mixed layer where they dissociate. In this case, the maximum in absorbed optical power is located 24 nm (~3× L_D) from the MoO_3/organic interface (see Fig. 2.3), thus reducing absorption near the interface by 15% compared to the mixed-HJ cell.
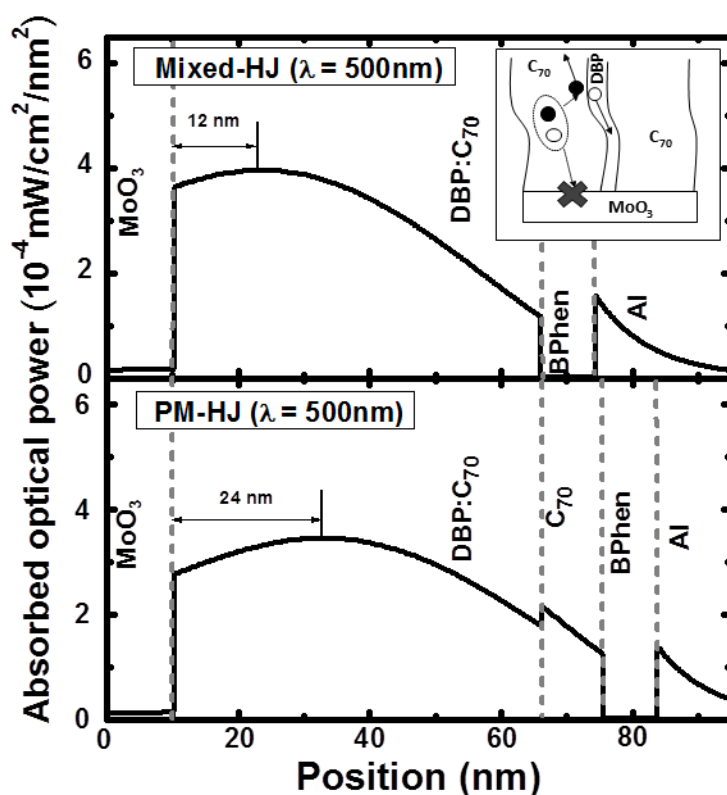
Figure 2.3 Spatial distribution of absorbed optical power in the mixed-HJ (top) and PM-HJ (bottom) cells at a wavelength of $\lambda = 500$ nm. Device layer structures and the distances between the absorbed optical power peak and the MoO_3/organic interface are indicated. *Inset*: Illustration of two competing processes in the partially mixed, small molecule bulk heterojunction active region near to the MoO_3 interface. Excitons (dashed circle) generated in the mixed layer close to the MoO_3 interface can either quench at the MoO_3 interface ("**X**"), or dissociate into electrons (solid circle) and holes (open circle) at a nearby DBP/C_{70} interface.

2.5 Experiments

Following these design considerations, OPV cells were fabricated via vacuum thermal evaporation with the same structure as modeled, except where we vary both the DBP:C_{70} volume ratio, and the thickness (x) of the C_{70} cap layer. Devices were grown on glass substrates pre-coated with 100 nm-thick ITO with a sheet resistance of 15 $\Omega/\square$. Prior to thin film deposition, substrates were cleaned in detergent, de-ionized water, and a sequence of organic solvents,[19]

followed by exposure to ultraviolet (UV)-ozone for 10 min. The substrates were transferred into the vacuum chamber with a base pressure of 10^{-7} torr where MoO3, C70 and BPhen layers were deposited at a rate of 0.05 nm/sec. Both DBP and C_{70} were co-deposited using a DBP deposition rate of 0.02 nm/sec while the deposition rate of C_{70} was adjusted to achieve the desired volume ratio. A shadow mask with an array of 1 mm-diameter circular openings was used to pattern the 100 nm-thick Al cathode, thereby defining the cell area. The substrates were directly transferred into a glove box filled with ultrahigh purity N_2 where current density-voltage (J-V) characteristics in the dark and under simulated AM 1.5G solar irradiation, and EQE were measured. A National Renewable Energy Laboratory (NREL) traceable Si reference cell was used to determine optical power.[16] The EQE was determined in reference to a NIST-traceable Si detector using monochromated light from a Xe-lamp and chopped at 200 Hz. The short circuit current density (J_{SC}) was corrected for spectral mismatch.[20] Errors quoted are based on the deviation from the average of three or more devices on the same substrate.

2.6 Results and discussions

Optimization of the PM-HJ structure requires testing the effect of the DBP:C_{70} ratio. This ratio was optimized using a structure comprising ITO (100 nm) / 10nm MoO$_3$ (10 nm) / DBP:C_{70} (40 nm) / BPhen (8 nm) / Al (100 nm) with results summarized in Table 2.1. The J_{SC} increases as the amount of DBP is reduced from 1:4 to 1:8 mixtures where a maximum of $J_{SC} = 9.7 \pm 0.3$ mA cm^{-2} is obtained; further reductions in DBP concentration reduce the J_{SC}. The open circuit voltage (V_{OC}) increases monotonically from $V_{OC} = 0.85 \pm 0.01$ V to 0.90 ± 0.01 V with decreasing DBP concentration. The fill factor increases with decreasing DBP concentration, reaching a maximum of $FF = 0.55 \pm 0.01$ at a 1:8 ratio, and remains unchanged as the DBP

concentration is further reduced in this partially mixed, heterogeneous region. This results in a

maximum in efficiency for this thickness of $PCE = 4.7 \pm 0.2\%$ for the 1:8 ratio. The relatively

high FF for a small molecule co-evaporated OPV likely results from the balanced electron and

hole mobilities in the mixed-layer domains and preferable donor-acceptor phase segregation that

reduce bimolecular recombination. [62-65]

Table 2.1 Device performance for various mixture ratios for a PM-HJ. Error on V_{OC} and FF are all ± 0.01.

Blend ratio	V_{OC} (V)	J_{SC} (mA/cm^2)	FF	PCE (%)
1:4	0.85	9.1 ± 0.2	0.50	3.9 ± 0.1
1:6	0.87	9.5 ± 0.2	0.53	4.4 ± 0.1
1:8	0.89	9.7 ± 0.2	0.55	4.7 ± 0.2
1:10	0.90	9.3 ± 0.3	0.55	4.5 ± 0.1
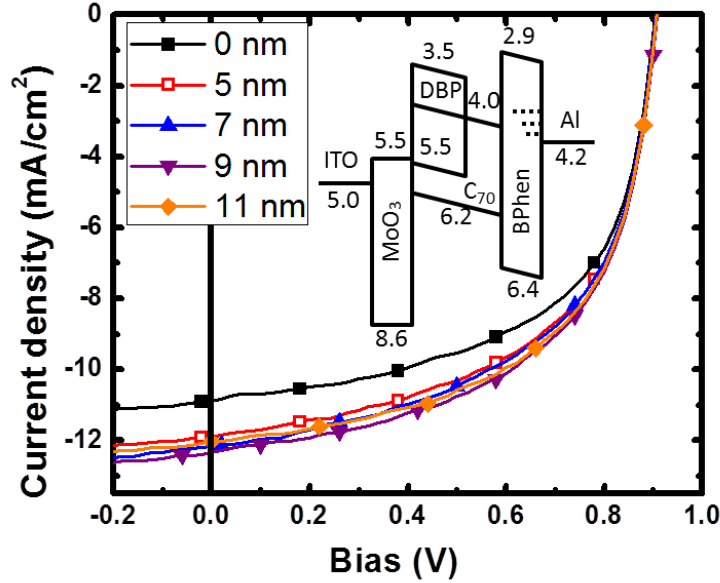
Figure 2.4 Spectrally-corrected current density *vs.* voltage (*J-V*) characteristics under simulated AM1.5G, one sun illumination as a function of the thickness (*x*) of the neat C_{70} cap layer. The mixed-HJ corresponds to *x* = 0, and the hybrid PM-HJ cells have a C_{70} thickness of *x* > 0 as indicated. *Inset*: Energy level diagram of the PM-HJ cell. The energy level data (shown in eV) are taken from literature referenced in text. The dashed lines in the BPhen layer indicate defect states induced during the metal deposition.

The *J-V* characteristics of the cells with different C_{70} cap thicknesses under AM1.5G, 1 sun intensity simulated solar illumination are shown in Fig. 2.4, with device performance characteristics summarized in Table 2.2. All cells have V_{OC}= 0.91 ± 0.01 V. According to Giebink, *et al.*,[24] the maximum open circuit voltage is given by $qV_{OC}=\Delta E_{HL}-E_B$, where ΔE_{HL} is the difference between the HOMO of the donor and the lowest unoccupied MO (LUMO) of the acceptor, and E_B is the polaron pair binding energy (see inset, Fig. 2.4 for the HOMO and LUMO energies of materials used).[34, 53, 61, 66] Hence, it is expected that V_{OC} should be similar for the mixed-HJ and the PM-HJ cells. All the cells also have a fill factor of $FF = 0.56 \pm$ 0.01. The mixed-HJ cell has $J_{SC} = 10.7 \pm 0.2$ mA/cm^2, resulting in a power conversion efficiency

of $PCE = 5.7 \pm 0.1\%$. The addition of a C_{70} layer ($x= 9$ nm) leads to $J_{SC} = 12.3 \pm 0.3$ mA/cm^2,

resulting in $PCE = 6.4 \pm 0.3\%$.

Table 2.2 Device performance of mixed-HJ and hybrid PM-HJ cells. The thickness of the planar C_{70} layer is "x".

Cell Structure (x nm)	V_{OC} (V)	J_{SC} (mA/cm^2)	FF	PCE (%) 1 sun, AM1.5G	Spectral mismatch factor
mixed-HJ (0)	0.90(±0.01)	10.7 (±0.2)	0.57 (±0.02)	5.7 (±0.2)	1.03
PM-HJ (5)	0.91(±0.01)	11.9 (±0.2)	0.56 (±0.01)	6.1 (±0.2)	1.04
PM-HJ (7)	0.91(±0.01)	12.1 (±0.2)	0.56 (±0.01)	6.2 (±0.2)	1.03
PM-HJ (9)	0.91(±0.01)	12.3 (±0.3)	0.56 (±0.01)	6.4 (±0.3)	1.03
PM-HJ (11)	0.91(±0.01)	12.0 (±0.2)	0.56 (±0.01)	6.2 (±0.2)	1.04

As the C_{70} thickness increases to $x= 9$ nm, the EQE of the PM-HJ cell increases by up to 10% between $\lambda= 400$ nm and 700 nm compared to the mixed-HJ cell (see Fig. 2.5). This, in turn, leads to a 15% increase in J_{SC}. As x is increased further to 11 nm, J_{SC} decreases to 12.0 ± 0.2 mA/cm^2. The EQE of the PM-HJ cell with a 9 nm-thick C_{70} layer is >70% between $\lambda= 450$ nm and 550 nm, and averages >65% within the spectral range from $\lambda= 350$ nm to 650 nm, leading to $J_{SC} = 12.3 \pm 0.3$ mA/cm^2.
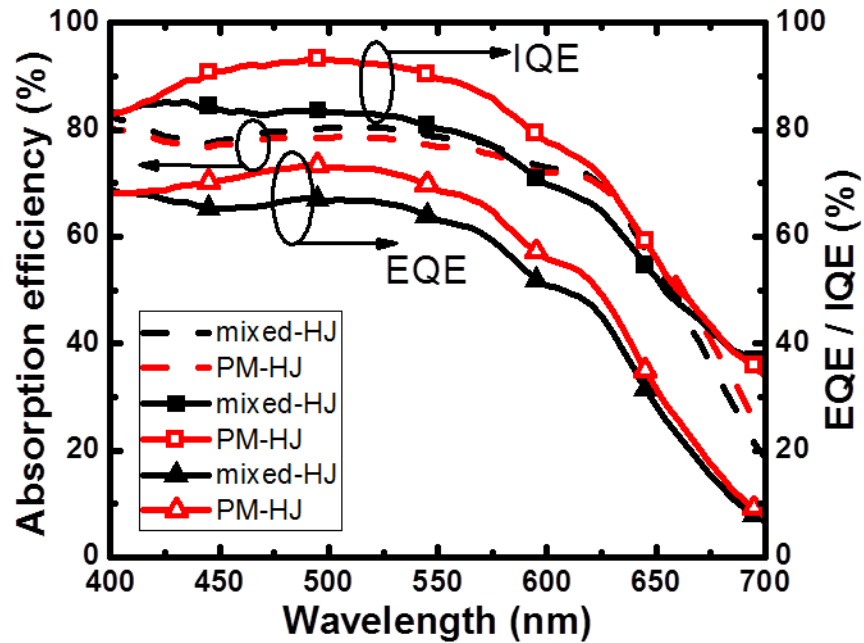
Figure 2.5 Absorption efficiency (dashed lines), external quantum efficiency (*EQE*, triangles) and internal quantum efficiency (*IQE*, squares) spectra for the mixed-HJ and PM-HJ (with a *x*= 9 nm-thick C$_{70}$ cap layer) OPV cells.

The internal quantum efficiency, *IQE*, is defined as the ratio of free carriers collected at the electrodes to photons absorbed in the photoactive layers.[2, 21] We employed the transfer matrix method[2, 60] to calculate the absorption efficiency, η_A, to further understand the origin of improvement in *EQE* in the PM-HJ cell. Based on the optical simulation, the mixed-HJ and PM-HJ cells show similar absorption spectra with η_A >75% between λ= 400 nm and 650 nm, as shown in Fig. 2.5. The PM-HJ cell has *IQE* >90% within the spectral range of λ= 450 nm and 550 nm, while the *IQE* of the mixed-HJ cell is only ~80% in the same spectral region (Fig. 2.4). The addition of the C$_{70}$ layer in the PM-HJ cell redistributes the optical field inside the photoactive layer, as shown in Fig. 2.3, leading to increased exciton generation and dissociation in the photoactive region, and reduced exciton quenching at the MoO$_3$/organic interface. With

IQE > 90%, we infer that almost all the photons absorbed in the PM-HJ cell are converted into free carriers and collected at the electrodes, consistent with the morphology in the inset, Fig. 2.3.

2.7 Conclusions

In summary, we have shown that excitons generated on both DBP and C_{70} are quenched at the MoO_3 anode buffer layer. Quenching at the MoO_3/organic interface in small molecular weight, partially mixed regions consisting of a relatively high concentration of C_{70} compared to DBP can be reduced by including an acceptor (C_{70}) cap on the mixed region. This, in turn, reduces excitons generated near the MoO_3 interface. This architecture leads to a significant improvement in device performance compared to a simple mixed 1:8 DBP:C_{70} HJ cell. A maximum power conversion efficiency of *PCE* = 6.4 ± 0.3% is achieved for the PM-HJ cell under simulated AM 1.5G one sun illumination, representing a 12% increase compared to the analogous mixed-HJ cell. With *IQE* >90% for the PM-HJ, our structure is characterized by efficient exciton diffusion, dissociation and charge transport.

Chapter III

Electron filtering buffer for PM-HJ OPV cells

In Chapter 2, we demonstrated a DBP:C_{70} PM-HJ OPV with a power conversion efficiency of $PCE = 6.4 \pm 0.3$ % under simulated AM 1.5G illumination at 1 sun intensity.[67] Despite its high J_{SC} and V_{OC}, the DBP:C_{70} PM-HJ OPV cell suffers from a relatively low fill factor of $FF = 56 \pm 1$%, suggesting that there remains considerable room for performance improvements. In this chapter, we demonstrate PM-HJ OPV cells employing fullerene-based compound cathode buffer layers that block excitons while efficiently conducting electron-polarons, thereby acting as an "electron filter" that results in reduced bimolecular recombination and exciton-polaron quenching. The compound buffer consists of a blend of wide energy-gap, exciton-blocking bathophenanthroline (BPhen) and electron conducting C_{60} capped with a neat BPhen layer. The compound buffer significantly increases FF in the PM-HJ to 66 ± 1%. Hence, the OPV with a compound buffer achieves $PCE = 8.1 \pm 0.4$ % under simulated AM 1.5G, 1 sun illumination. Furthermore, the responsivity, $R = J_{SC}/I$, where I is the incident light intensity, of the control monotonically decreases with light intensity in contrast to the cell with a BPhen:C_{60}/BPhen electron-filtering buffer whose responsivity is nearly constant over the same light intensities, providing further evidence that both bimolecular recombination and exciton-polaron quenching are suppressed.

3.1 Principle loss mechanisms in the PM-HJ structure

In the PM-HJ structure, there are two principal loss mechanisms leading to the low *FF*. One is bimolecular recombination of free charge carriers in the extensive donor-acceptor blended region of the PM-HJ structure,[68-69] whose rate is given by $k_{BM} = \gamma \cdot n \cdot p$. Here, γ is the Langevin recombination constant, and n (p) is the free electron (hole) density. A second significant loss is due to exciton-polaron quenching in the neat C_{70} layer.[70-71] In previous work[72], electron-polaron build-up was observed at the neat acceptor/blocking layer interface that results in quenching and, therefore, a reduction of internal quantum efficiency (*IQE*). Note that exciton-polaron quenching follows a similar relationship to bimolecular recombination, as both exciton and polaron concentrations are proportional to intensity. Both mechanisms can result in a loss in photocurrent under forward bias that increases the slope of current density-voltage (*J-V*) characteristics in the fourth quadrant, ultimately decreasing both *FF* and *PCE*.

3.2 Fullerene-based mixed buffer layer for OPV cells

Recently, an electron conducting/exciton blocking fullerene-based mixed buffer layer placed adjacent to the cathode was shown to increase the efficiency of bilayer OPV cells as shown in Fig. 3.1.[72] The buffer consists of a mixture of C_{60} that efficiently conducts electron-polarons and wide energy gap bathocuproine (BCP) that blocks excitons. Exciton-polaron quenching was significantly reduced in bilayer cells employing this "electron filter" due to its ability to spatially separate excitons and polarons at the blocking interface. This led to a significant increase in J_{SC}, while V_{OC} and *FF* remained unchanged. The PM-HJ cells additionally suffer from bimolecular recombination in the mixed photoactive layer. Using a mixed buffer

results in a reduced interfacial field with the active layer due to its increased conductivity compared to a neat, conventional blocking buffer layer.[72] The resulting increase in field across the photosensitive region leads to more rapid charge extraction. This, in turn, leads to reduced bimolecular recombination in the cell.
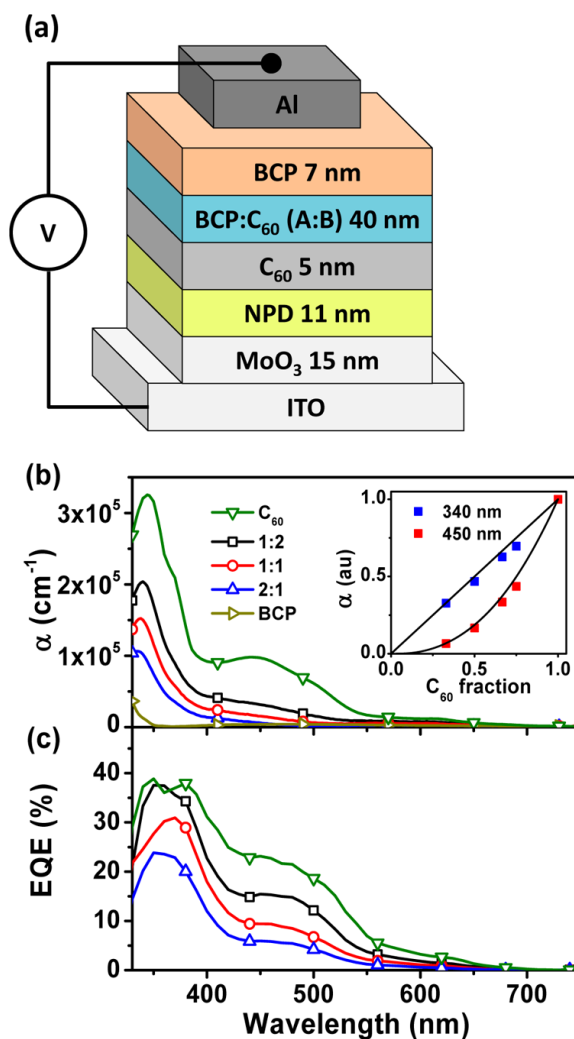
Figure 3.1 Absorption and *EQE* spectra of OPVs with BCP:C_{60} mixtures of different blend ratios as buffers. (a) Device structures with different BCP:C_{60} volume ratios. (b) Absorption and (c) *EQE* spectra of BCP:C_{60} mixtures with a variety of blend ratios. *Inset*: Extinction coefficients as a function of C_{60} fraction in the BCP:C_{60} mixture at $\lambda = 360$ nm and 450 nm, respectively.[72]

3.3 Physical properties of fullerene-based mixture buffers

The charge transport properties of the BPhen:C_{60} mixed buffer were investigated by 3-D Monte Carlo simulations of the layer, programmed in Matlab. The buffer was modeled as a random distribution of BPhen and C_{60} molecules on a cubic lattice, with electron transport attributed to nearest-neighbor hopping between C_{60} molecules. In this model, Columbic interactions between charges are neglected, and the lattice sites are assumed to be isoenergetic, aside from energy differences imposed by the applied electric field. Transfer probabilities were calculated according to Miller-Abrahams theory[73-77], from which the median extraction time for charges injected on one side of the buffer layer was obtained. The mobility of the layer was then calculated from the relationship between extraction time and electric field, normalized by setting the zero-field mobility of electrons in neat C_{60} layer to the experimental value of 5.1×10^{-2} cm^2/V·s.[78] For a 1:1 mixed buffer, the model predicts an effective mobility of 4.7×10^{-3} cm^2/V·s, only one order of magnitude lower than that of neat C_{60}. In comparison, the neat BPhen film has a significantly lower electron mobility of 1.9×10^{-5} cm^2/V·s[79], leading to charge pile-up at the buffer interface that promotes quenching.

The model was tested by examining the predictions for different thicknesses of a 1:1 mixed buffer, with results in Fig. 3.2. We find a linear relationship between extraction time (corresponding to film mobility) at a given voltage and thickness of the mixed layers, which translates to a linear increase in series resistance, assuming a constant charge density (i.e. a constant illumination intensity). Fits to experimental data for mixed buffer DBP:C_{60} OPVs are shown in Figure 3.2, inset. Now, a neat BPhen layer conducts electrons through defect states induced during metal deposition, thereby leading to a superlinear relationship between thickness and resistance.[80] In contrast, the mixed buffer resistance increases linearly with thickness even

up to 20 nm, suggesting that electrons in the mixed buffer are predominantly conducted by the C_{60} in the mixture.
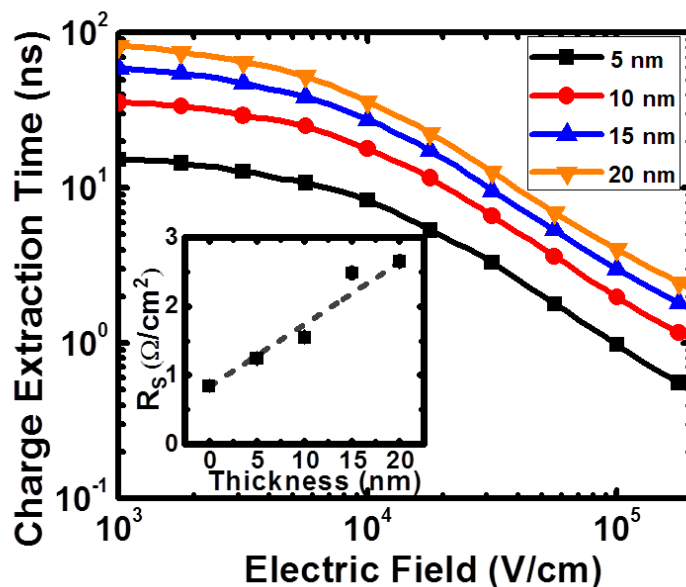
Figure 3.2 Charge extraction time *vs.* electric field for various layer thicknesses calculated using 3-D Monte-Carlo simulations. *Inset*: Cell series resistance (RS) *vs.* layer thickness with a linear fit (dashed line) to the data obtained from the OPV cells (squares) (Error bars in the inset are smaller than data points).

Previously, we showed that the 1:1 BCP:C_{60} blend has an 81% exciton-blocking efficiency using 3-D Monte Carlo simulations.[72] Here, we experimentally investigate its exciton blocking efficiency using the photoluminescence (PL) excitation spectra of 40 nm-thick C_{70} film capped with a 1:1 BPhen:C_{60} blend on quartz.[81] By comparing the PL intensity of the layer deposited onto the surface of the blend under study to that of either a "perfectly" blocking or quenching layer, the relative importance of these processes can be determined. For this comparison, therefore, an 8 nm-thick BPhen or N,N'-diphenyl-N,N'-bis(1-naphthyl)-1-1'biphenyl-4,4'diamine (NPD) layer are used as reference, perfectly exciton blocking or

quenching layers[81], respectively. The PL intensity of the mixed buffer is nearly identical to the intensity found for the blocking reference (see Fig. 3.3), demonstrating that BPhen:C_{60} mixed layers can efficiently block excitons. Since BPhen:C_{60} mixture has a relatively high electron mobility, the mixed buffer layer can spatially separate excitons and polarons acting as an effective filter, leading to a reduction of exciton-polaron quenching within the neat fullerene layer.
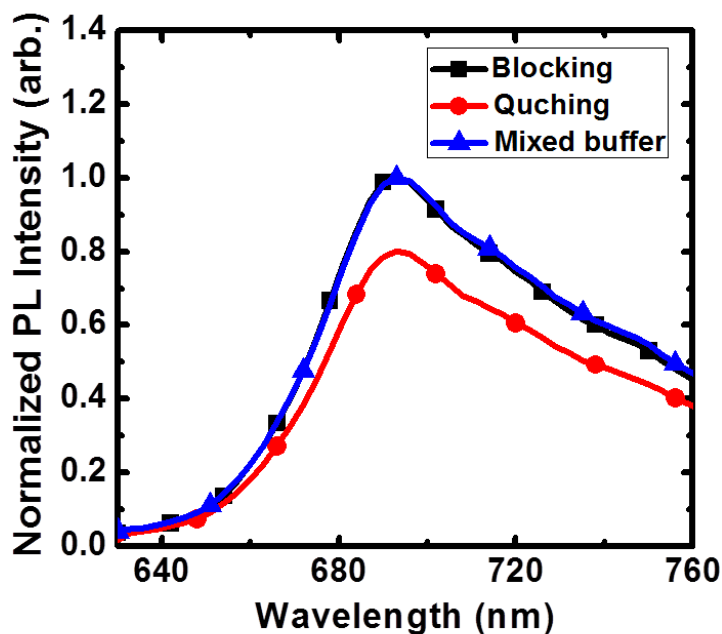
Figure 3.3 Photoluminescence (PL) spectra for a neat C_{70} layer in contact with BPhen (blocking), NPD (quenching) and BPhen:C_{60} mixed layers obtained at an excitation wavelength of $\lambda = 520$ nm.

3.4 Experiments

The OPV cells were grown by vacuum thermal evaporation (VTE) at a base pressure of 2×10-7 torr on glass substrates pre-coated with indium tin oxide (ITO, sheet resistance: 15 $\Omega/\square$

). Prior to deposition, the substrates were cleaned in diluted Tergitol® (Type NP-10), deionized water, acetone and isopropyl alcohol,[16] and then exposed to ultraviolet-ozone for 10 min. We obtained MoO3 from Acros Organics, C60 from Materials and Electrochemical Research Corp., BPhen and DBP from Luminescence Technology Corp., and C70 from SES Research. DBP, C60 and C70 were purified once via thermal gradient sublimation.[17] The MoO3 and BPhen layers were grown at a rate of 0.1 nm/s, DBP and C70 were co-deposited using a DBP deposition rate of 0.02 nm/s and a C70 deposition rate of 0.16 nm/s to achieve a 1:8 ratio. The BPhen:C60 mixed buffer was grown by co-depositing BPhen and C60 each at a rate of 0.05 nm/s creating a 1:1 blend. A 100 nm-thick Ag cathode was subsequently deposited through a shadow mask defining an array of 15, 1 mm diameter devices (device area of 0.008 cm2). Following fabrication, devices were transferred into a glovebox filled with ultra-high purity N2 for measurement of the J-V characteristics and EQE. During measurement, only the tested device was under illumination while other devices were kept in the dark. The solar simulator intensities were calibrated using a NREL-traceable Si reference cell, and JSC was corrected for spectral mismatch.[18] The EQE as a function of wavelength (λ) was obtained with a lock-in amplifier and monochromated light from Xe-lamp chopped at 200 Hz. Errors in JSC and PCE arise primarily from uncertainties in light intensity and spectral calibration.

3.5 Mixed HJ with electron-filtering buffers

To disaggregate the sources of loss, we employ the BPhen:C_{60} mixed buffer with only a DBP:C_{70} mixed HJ as the photoactive region to determine the effects of bimolecular recombination alone. In this structure, excitons rapidly dissociate into charge carriers within the

DBP:C_{70} blend.[67] The exciton concentration is negligible in the mixed layer, thereby eliminating exciton-polaron quenching as a significant loss mechanism.

The mixed HJ cells were grown by vacuum thermal evaporation (VTE) with the structure: MoO_3 (10 nm)/DBP:C_{70} (54 nm, 1:8 volume ratio)/Buffer/Ag (100 nm). Two different buffer layers were employed: 8 nm-thick BPhen (control), and 10 nm-thick BPhen:C_{60} mixed layer at 1:1 ratio (by volume) capped with a neat, 5 nm-thick BPhen layer. Figs. 3.4(a) and (b) show the *J-V* characteristics and *EQE* spectra of mixed HJ devices employing the control and compound buffers. The control has $FF = 55 \pm 1$ %, $J_{SC} = 12.5 \pm 0.3$ mA/cm^2, $V_{OC} = 0.91 \pm 0.1$ V and $PCE = 6.3 \pm 0.3$ % under simulated AM 1.5G, 1 sun illumination (spectral mismatch factor[82] $= 1.00 \pm 0.01$), as previously.[67] The cells with the compound electron-filter buffer exhibit improvement in all three performance parameters, leading to $FF = 63 \pm 1$ %, $J_{SC} = 12.8 \pm 0.3$ mA/cm^2, $V_{OC} = 0.93 \pm 0.1$ V and $PCE = 7.5 \pm 0.4$ %, the latter corresponding to a 19% increase compared to the control.
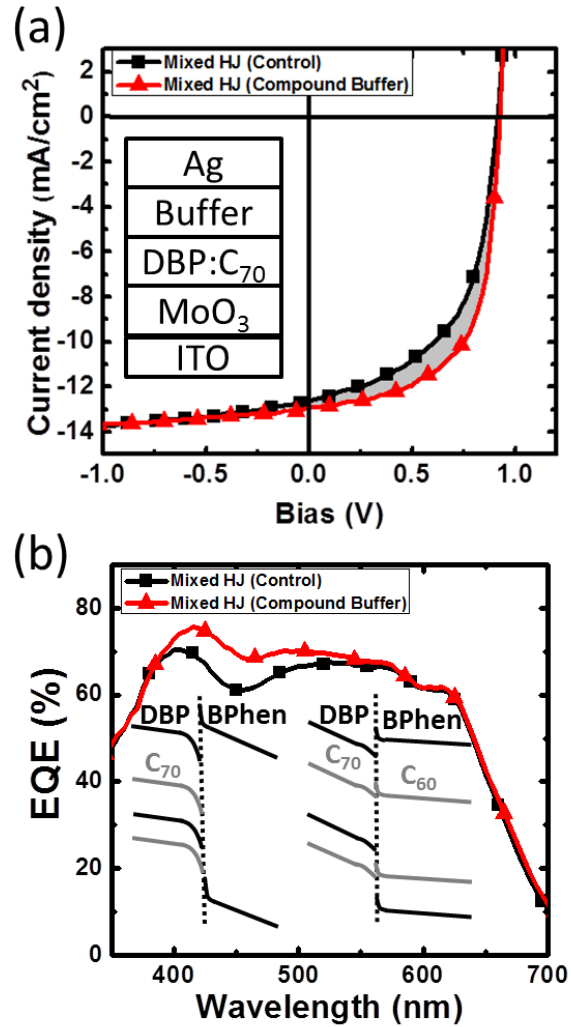
Figure 3.4 (a) Spectrally-corrected current density *vs.* voltage (*J-V*) characteristics under simulated AM 1.5G, 1 sun illumination for DBP:C_{70} mixed-HJ OPV cells. The shaded region emphasizes the difference in fill factors, and hence maximum power output, of the two cells. *Inset*: Schematic of the device structure; (b) External quantum efficiency (*EQE*) spectra for the cells in (a). *Inset*: Schematic diagrams of energy levels at the DBP:C_{70}/buffer interface (left: neat BPhen buffer; right: BPhen:C_{60} compound buffer).

The significant improvement in *FF* for the device with the compound buffer is shown in Fig. 3.4(a) (indicated by the shaded region between the curves) with the energy level diagram in Fig. 3.4(b), inset. Previous studies have shown that energy level bending occurs at the fullerene/BCP interface [83-84], leading to electron accumulation and a large potential drop as

43

shown in the left inset. Consequently, the field across the active layers is reduced as the voltage is redistributed, increasing the charge extraction time and, therefore, the residence time for electrons and holes at the donor-acceptor heterointerface where they have an opportunity to recombine. In the case of the compound buffer, the high conductivity of the 1:1 BPhen:C_{60} blend[72] results in less electron accumulation and, therefore, a smaller potential drop at the interface (right inset, Fig. 3.4(b)) and a higher electric field in the DBP:C_{70} mixed region. This in turn leads to reduced bimolecular quenching, and consequently an increased *FF* and *EQE* at wavelengths between $\lambda = 400$ nm and 550 nm, as shown in Fig. 3.4(b).

Both cells show almost identical *EQE* at $\lambda < 400$ nm and $\lambda > 550$ nm (see Fig. 3.4(b)). At $\lambda < 400$ nm, the photoactive region absorption decreases in the compound buffer cell resulting from parasitic absorption in the BPhen:C_{60} mixed buffer[72] while the internal quantum efficiency (*IQE*) increases due to reduced bimolecular recombination. Overall, the *EQE* of the compound buffer cell is nearly equal to the control cell. At $\lambda > 550$ nm, the absorbed optical power peak as well as charge distribution peak shift towards the anode, since the excitons generated in the DBP:C_{70} mixed region almost immediately dissociate into charges. This reduces the population of holes at the DBP:C_{70}/BPhen interface (close to the cathode side) where electrons pile up in the control cell, while at the same time improving hole extraction. The spatial separation of the holes and electrons at longer excitation wavelengths reduces bimolecular recombination in the control cell, leading to the almost identical *EQE* as well.

To understand the role of bimolecular recombination, we investigated the responsivity (*R*) for both cells as a function of light intensity (*I*). The control cell is found to have a monotonic decrease in *R* with *I*, from $R = (12.7 \pm 0.4) \times 10^{-2}$ A/W at $I = 0.6$ sun, to $(11.8 \pm 0.3) \times 10^{-2}$ A/W at $I = 2.7$ suns, while for the compound buffer cell, *R* drops by only 0.2×10^{-2} A/W over the same

range of intensities (see Fig. 3.5). In general, $J_{SC} = J_G - J_{MM} - J_{BM}$, where J_G is the photogenerated current density, J_{MM} is the monomolecular recombination current density and J_{BM} is the bimolecular recombination current density. Both J_G and J_{MM} are linearly proportional to I, while $J_{BM} \sqcup \gamma \cdot n \cdot p \sqcup \beta \cdot I^2$, where γ is the Langevin coefficient and β is a constant. Therefore, $R = J_{SC}/I = R_0 - \beta \cdot I$, where R_0 is the responsivity in the absence of bimolecular recombination. The linear fits to this analysis (dashed lines, Fig. 3.5) yields $R_0 = 12.9 \times 10^{-2}$ A/W for both cells. The same intercept for both cells at zero light intensity suggests that both OPV cells have the same responsivities as $I \to 0$ in the absence of bimolecular recombination. However, β for the control is four times larger than that for the cell with the compound buffer. The smaller β for the compound buffer cell suggests that bimolecular recombination is only 25% of that of the control cell, indicating that the electron and hole concentrations have each decreased, on average, by 50% due to the increased electric field in the mixed region. This larger internal field across the heterojunction in the compound buffer cell compared to that of the control for a given external bias results in improved charge extraction and, therefore, higher *FF*.
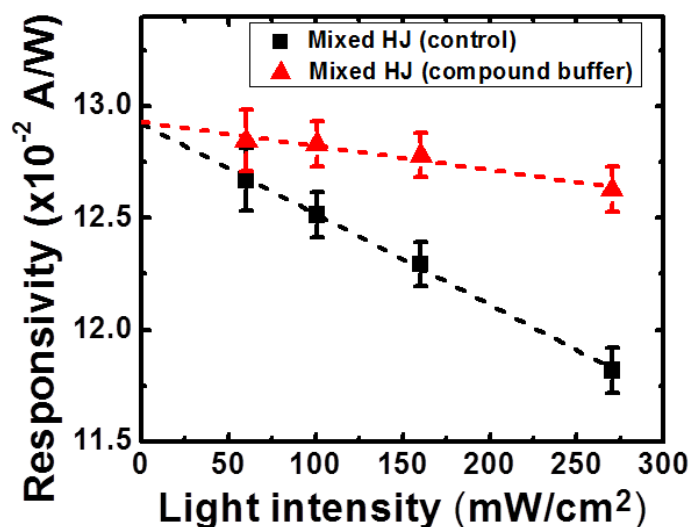
Figure 3.5 Responsivity *vs.* light intensity for the mixed-HJ control cell and the compound buffer cell with linear fits according to bimolecular recombination theory (dashed lines).[15, 16]

3.6 PM-HJ with electron-filtering buffers

The DBP:C_{70} PM-HJ OPV exploits the advantages of the mixed buffer by employing it adjacent to a neat C_{70} layer using the following structure: ITO/ MoO_3 (10 nm)/DBP:C_{70} (54 nm, 1:8)/C_{70} (9 nm)/Buffer/Ag (100 nm). Figure 3.6 shows the *J-V* characteristics and *EQE* spectra (inset) of the cells with both the control and compound buffers. The control has *PCE* = 7.1 ± 0.3%, which is comparable to previous results.[67] The compound buffer results in a nearly 20% increase in *FF* to 66 ± 1%, as anticipated for architectures with reduced recombination of photogenerated carriers. Also, $V_{OC} = 0.93 ± 0.1$ V for the compound buffer compared with 0.91 ± 0.1 V for the control, and J_{SC} decreases to 13.2 ± 0.3 mA/cm^2 from 13.8 ± 0.3 mA/cm^2 for the control due to the reduced *EQE* in the range $\lambda < 420$ nm and $\lambda > 550$ nm. Overall, the OPV cell with a BPhen:C_{60}/BPhen buffer exhibits *PCE* = 8.1 ± 0.4 % under simulated AM 1.5G, 1 sun illumination, which is among the highest efficiencies reported for VTE-grown OPV cells. The

EQE and *IQE* spectra[2, 60] of the mixed buffer and control cells are shown in the inset, Fig. 3.6.

The compound buffer cell shows an increased *EQE* between $\lambda = 420$ nm and 550 nm while *EQE*

decreases outside of this range for the compound buffer cell compared to the control. Similar to

the case of the mixed HJ, the reduced *EQE* for the compound buffer cell at $\lambda < 420$ nm is due to

the absorption of BPhen:C_{60} mixed buffer. At $\lambda > 550$ nm, the peak absorbed optical power in the

control shifts closer to the anode than for the compound buffer cell, which enhances the hole

extraction and, therefore, reduces bimolecular recombination in the control. At $\lambda > 550$nm, the

absorbed optical power in the neat C_{70} layer in the control is lower than that in the compound

buffer due to the optical peak moving farther from the cathode, leading to the reduced exciton-

polaron quenching in the control. Therefore, the *EQE* for the control is higher than that for the

compound buffer cell at $\lambda > 550$ nm.
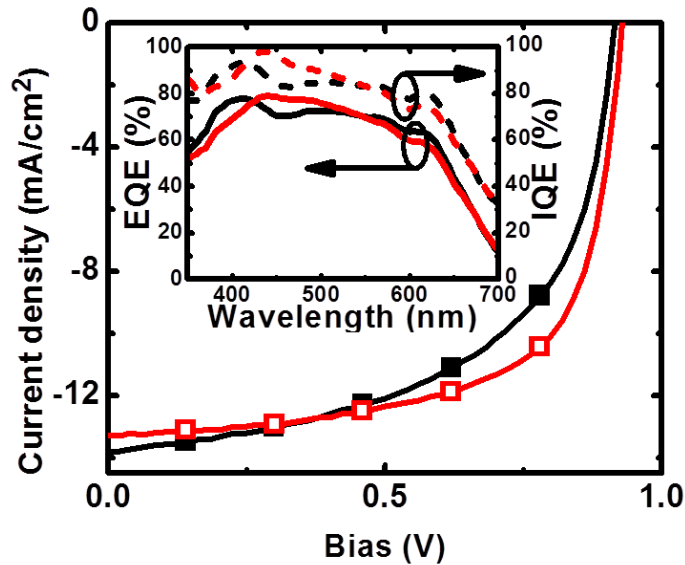
Figure 3.6 Spectrally-corrected current density *vs*. voltage (*J-V*) characteristics under simulated AM 1.5G, 1 sun illumination for DBP:C_{70} PM-HJ OPV cells with a neat BPhen buffer (solid squares), and a compound buffer (hollow squares). *Inset*: *EQE* (solid lines) and *IQE* (dashed lines) spectra for the control (black) and the compound buffer cell (red)).

47

The *IQE* of the compound buffer cell averages ~90% between λ = 350 nm and 500 nm while the *IQE* in the control averages only ~80% over the same spectrum range. The *IQE* increase results from a reduction in both bimolecular recombination and exciton-polaron quenching for the case of the mixed buffer.

The intensity dependence of *R* and *PCE* for both cells ranging from 0.6 sun to 2.7 sun is shown in Fig. 3.7. Similar to mixed HJ cells, the responsivity of the control cell decreases monotonically by 10%, from R =(14.3 ± 0.4)× 10^{-2} A/W at 0.6 sun to (13.0 ± 0.4)× 10^{-2} A/W at 2.7 sun. In contrast, the PM-HJ cell with the compound buffer shows only a 1.3% reduction with intensity. The significant drop in *R* of the control indicates substantial bimolecular recombination and exciton-polaron quenching, whereas these effects are significantly suppressed in the compound buffer cell.
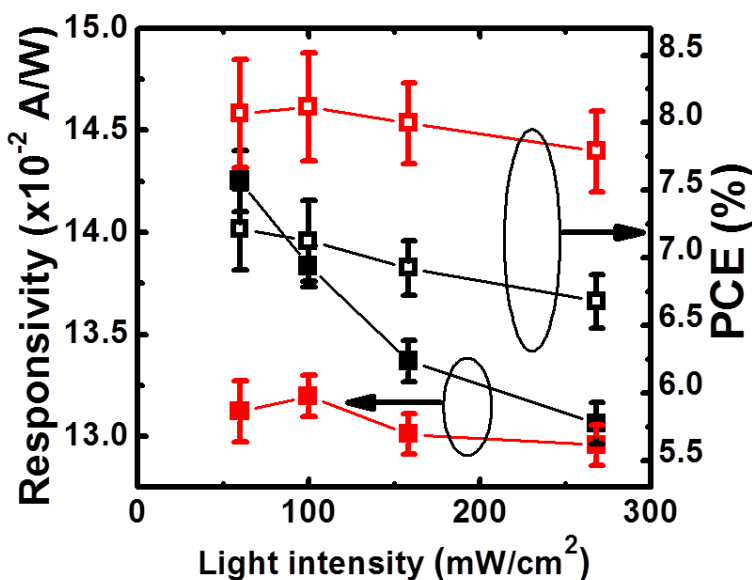
Figure 3.7 Responsivity (solid squares) and power conversion efficiency (*PCE*) (hollow squares) *vs*. light intensity for the PM-HJ control cell (black symbols), and the cell with a BPhen:C_{60}/BPhen compound buffer (red symbols).

3.7 Conclusions

In summary, we have demonstrated that the BPhen:C_{60}/Bphen compound buffer acts as an electron filter characterized by a high electron conductivity while efficiently blocking excitons. This combination of physical properties from the compound buffer prevents the build-up of charge at the active region/buffer interface even at very high illumination intensities, thereby suppressing losses from both bimolecular recombination and exciton-polaron quenching. The DBP:C_{70} PM-HJ cell with a compound buffer achieves a $PCE = 8.1 \pm 0.4$ % with $FF = 66 \pm$ 1% under simulated AM 1.5G, 1 sun illumination.

Chapter IV

Squaraine blend OPV cells

In Chapters 2 and 3, we discussed DBP:C_{70} PM-HJ cells that absorb primarily in the visible. There is, however, still a significant amount of photons in the near infrared (NIR) spectral regions of the solar spectrum. One challenge for OPVs is to find donors that lead to high efficiencies by extending the cell efficiency into the infrared.[85-86] In this context, squaraines are a promising class of donors due to their large absorption coefficients in both the visible and near-infrared spectral regions, along with their large V_{oc} (~1V) when paired with the acceptor, C_{60}.[87-91] We have recently demonstrated efficient OPVs based on 2, 4-bis[4-(N-Phenyl-1-naphthylamino)-2,6-dihydroxyphenyl] squaraine (1-NPSQ).[26, 91] However, since the absorption peaks of C_{60} and 1-NPSQ lie at wavelengths of λ= 450 nm and 710 nm, respectively, and the absorption spectrum of the squaraine molecule is relatively narrow (~100 nm full-width-half-max) compared to many other small molecule donors, there is a dip in the *EQE* spectrum between the C_{60} and 1-NPSQ peaks, ultimately limiting the OPV short circuit current density (*J_{sc}*). Here, we show that blending 1-NPSQ and the blue-shifted donor, 2, 4-bis[4-(N,N-diphenylamino)-2,6-dihydroxyphenyl] asymmetric squaraine (DPASQ), can partially fill the gap in *EQE* between λ= 500 nm and 600 nm, resulting in an increase in quantum efficiency in this spectral region that leads to improved device performance compared with single squaraine OPVs. Indeed, we show that solvent annealed blended cells can have power conversion

efficiencies of 5.9 ± 0.3%, representing a significant improvement over single donor 1-NPSQ and DPASQ reference devices.

4.1 Physical properties of functionalized squaraine donors

Functionalized squaraines provide a versatile class of donors with exceptionally high absorption coefficients that can be tuned from the green to the infrared by simple chemical and structural modifications. The squaraine donor layers in this work consist of various mixtures of 1-NPSQ, with an absorption peak of 2.3×10^5 cm^{-1} at λ= 710 nm, and DPASQ, with an absorption peak of 2.6×10^5 cm^{-1} at λ= 530 nm (see Fig. 4.1 for the absorption spectra of 1-NPSQ and DPASQ and their corresponding molecular structural formulae) that fits within the absorption gap between C_{60} and 1-NPSQ. With this combination of materials, in principle, the OPV cell response can overlap the solar spectrum from 400 nm to 1000 nm, as required for high efficiency solar energy conversion.[92]
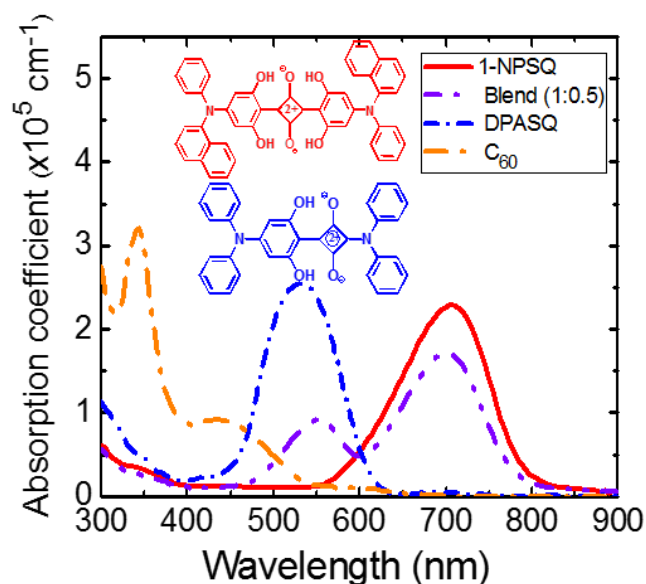
Figure 4.1 Absorption spectra of C_{60}, 1-NPSQ, DPASQ and blended 1-NPSQ:DPASQ (at weight ratio of 1:0.5) films. Inset: (upper) molecular structural formula of 1-NPSQ; and (bottom) DPASQ.

4.2 Experiments

The OPV cells were grown on glass substrates coated with 150 nm-thick indium tin oxide (ITO) with a sheet resistance of 20 $\Omega/\square$. The substrates were cleaned in a surfactant followed by a series of organic solvents,[93] and exposed to ultraviolet light and ozone for 10 min prior to loading into a high vacuum chamber with a base pressure of 1×10^{-7} torr. Vacuum thermal evaporation (VTE) was used to deposit an 80 Å-thick molybdenum oxide (MoO_3) layer on the ITO surface at a rate of 0.5 Å/s. Next, 1-NPSQ was dissolved in 1,2-dichlorobenzene (DCB) at 5 mg/ml, and then added to DPASQ powder to achieve the desired weight ratios. The mixture was stirred at 100°C in a glove box filled with ultrahigh purity N_2 for 12 hrs. After spin-casting the films at a rate of 3000 rpm for 40 s, the substrates were thermally annealed at 90 $^{\circ}$C for 6 min in

the N_2 atmosphere. The substrates were once more transferred to the high vacuum chamber for deposition of 400 Å C_{60} and an excition blocking and electron transporting layer of 80 Å 3, 4, 9, 10 perylenetetracarboxylic bis-benzimidazole (PTCBI), both at the rate of 1 Å/s. A 1000 Å-thich Ag cathode layer was deposited through a shadow mask with 1 mm-diameter circular apertures. The current density-voltage (*J-V*) and *EQE* measurements were performed in a nitrogen glove box. The *J-V* characteristics were measured in the dark and under simulated AM 1.5G solar illumination. The incident power intensity at one sun (100 mW/cm^2) was measured using an NREL-calibrated Si reference cell. The measured photocurrent was corrected by a spectral mismatch factor between 0.97 and 1.0, depending on the *EQE* spectrum.[82, 94] Here, *EQE* was obtained using light from a 200 Hz-chopped and monochromated Xe-lamp.

4.3 Results

The *J-V* characteristics under 1 sun AM1.5G simulated illumination of blended OPVs at various weight ratios of 1-NPSQ to DPASQ are presented in Fig. 4.2 and Table 4.1. Here, the neat 1-NPSQ (120 Å thick from a 5mg/ml 1-NPSQ solution) and DPASQ (85 Å thick from a 1mg/ml DPASQ solution) cells are used as controls. The V_{oc} of neat 1-NPSQ and DPASQ cells are 0.92 V and 1.00 V, respectively, whereas V_{oc} of the blended cells increases with DPASQ concentration. As shown in Table 4.1, V_{oc} increases to 1.00 V at a 1:2 1-NPSQ:DPASQ, which is the same as for that of the neat DPASQ cells.
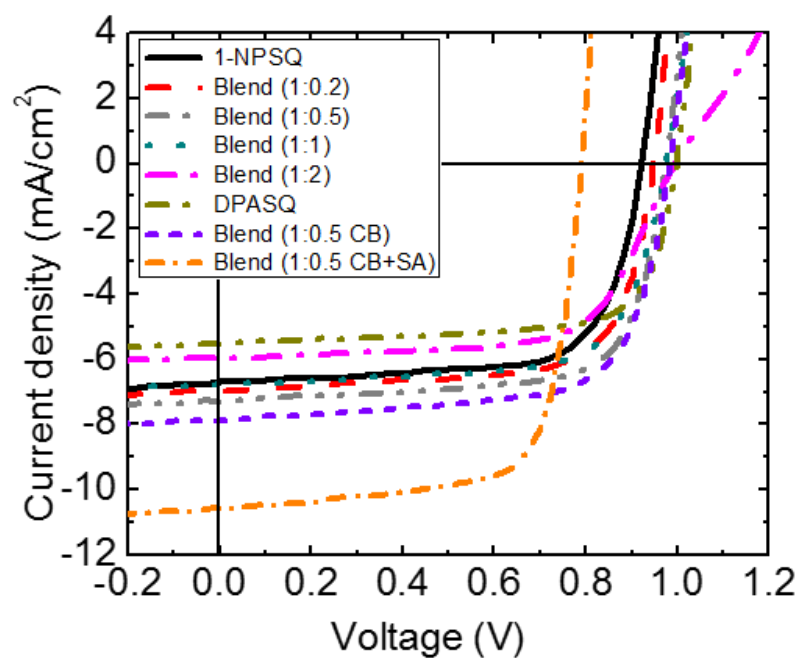
Figure 4.2 Current density-voltage characteristics under 1 sun, AM1.5G simulated solar illumination (spectrally corrected) for thermally-annealed, neat 1-NPSQ, DPASQ and blended donor cells at various weight ratios of 1-NPSQ to DPASQ. Also shown are characteristics for solvent-annealed (SA), blended cells at a 1:0.5 ratio (here, CB=compound buffer is used).

Table 4.1 Device performance of various 1-NPSQ, DPASQ and blended cells.

Device	V_{oc} (V)	J_{sc} (mA/cm^2)	FF	PCE (%) at 1 sun	J_s (mA/cm^2)	n	R_s ($\Omega \cdot$cm^2)
1-NPSQ (TA*)	0.92($\pm$0.02)	6.8($\pm$0.1)	0.70($\pm$0.01)	4.4($\pm$0.1)	(7.2$\pm$0.6)$\times$10^{-9}	1.72($\pm$0.04)	2.2($\pm$0.2)
Blend(1:0.2, TA)	0.94($\pm$0.02)	7.1($\pm$0.1)	0.71($\pm$0.01)	4.7($\pm$0.1)	(1.8$\pm$0.2)$\times$10^{-8}	1.89($\pm$0.04)	1.4($\pm$0.1)
Blend(1:0.5, TA)	0.98($\pm$0.02)	7.3($\pm$0.2)	0.71($\pm$0.01)	5.1($\pm$0.2)	(1.3$\pm$0.2)$\times$10^{-8}	1.96($\pm$0.05)	2.5($\pm$0.2)
Blend(1:1, TA)	0.98($\pm$0.02)	7.0($\pm$0.2)	0.7($\pm$0.02)	4.8($\pm$0.2)	(6.0$\pm$0.5)$\times$10^{-8}	2.16($\pm$0.07)	3.0($\pm$0.3)
Blend(1:2, TA)	1.00($\pm$0.02)	6.0($\pm$0.2)	0.66($\pm$0.01)	3.9($\pm$0.2)	(1.5$\pm$0.1)$\times$10^{-8}	2.23($\pm$0.07)	7.1($\pm$0.5)
DPASQ (TA)	1.00($\pm$0.02)	5.5($\pm$0.1)	0.72($\pm$0.01)	4.0($\pm$0.1)	(1.0$\pm$0.1)$\times$10^{-10}	1.58($\pm$0.03)	2.9($\pm$0.2)
Blend(1:0.5, CB#+TA)	0.98($\pm$0.02)	7.8($\pm$0.2)	0.69($\pm$0.01)	5.2($\pm$0.2)	(1.4$\pm$0.3)$\times$10^{-8}	1.88($\pm$0.04)	1.4($\pm$0.2)
Blend(1:0.5, CB+SA$^\Diamond$)	0.78($\pm$0.02)	10.5($\pm$0.5)	0.72($\pm$0.01)	5.9($\pm$0.3)	(1.5$\pm$0.2)$\times$10^{-8}	1.58($\pm$0.02)	1.0($\pm$0.1)

*TA: thermal annealed   #CB: compound buffer $^\Diamond$SA: solvent annealed.

4.4 Discussions

To understand the increase in V_{oc} of the blended cells, we used ultraviolet photoemission spectroscopy (UPS) to measure the highest occupied molecular orbital (HOMO) energies of 10 Å thick films of 1-NPSQ and DPASQ. Films were spun cast onto ITO/glass substrates and then transferred to an ultrahigh vacuum chamber from an inert N$_2$ environment. The measurements were performed at a base pressure $< 10^{-8}$ torr using 21.22 eV He-I emission in a Thermo VG scientific Clam 4MCD analyzer system. There is ~0.1 eV shift of the low energy cutoff between 1-NPSQ and DPASQ films (see Fig. 4.3(a)), while the high energy cutoffs of 1-NPSQ and DPASQ are almost identical (see Fig. 4.3(b)). This suggests that the HOMO energy of DPASQ is 0.1 eV deeper than that of 1-NPSQ; i. e., the HOMO levels of 1-NPSQ and DPASQ are at 5.3 $\pm$ 0.1 eV and 5.4 $\pm$ 0.1 eV below the vacuum level, respectively. Since V_{oc} is related to the energy

difference between the HOMO energy of the donor and the lowest unoccupied MO (LUMO) of the acceptor, less the polaron binding energy (i.e. the so-called interfacial energy gap, ΔE_{DA}),[95-97] the deeper HOMO level of DPASQ compared with 1-NPSQ leads to an increase in V_{oc} of the former cell. Assuming a relationship between ΔE_{DA} of the blend and the relative concentrations of the two donor constituents follows a linear relationship (i.e. $\Delta E_{DA} = \rho\, \Delta E_{DA:1-NPSQ} + (1-\rho)\, \Delta E_{DA:DPASQ}$, where ρ is the weight ratio of 1-NPSQ to DPASQ, and the energies correspond to the HOMO-LUMO offsets of the individual constituents with C_{60}, respectively), then V_{oc} of the blended cells should similarly depend on ρ at the donor-acceptor interface. For example, at 1:2 1-NPSQ:DPASQ, the DPASQ concentration at the surface exceeds that of 1-NPSQ, forming a nearly continuous layer at the donor/acceptor interface. Therefore, the 1:2 blend cells have V_{oc} $=1.00 \pm 0.02$ V, the same as that of neat DPASQ cells.
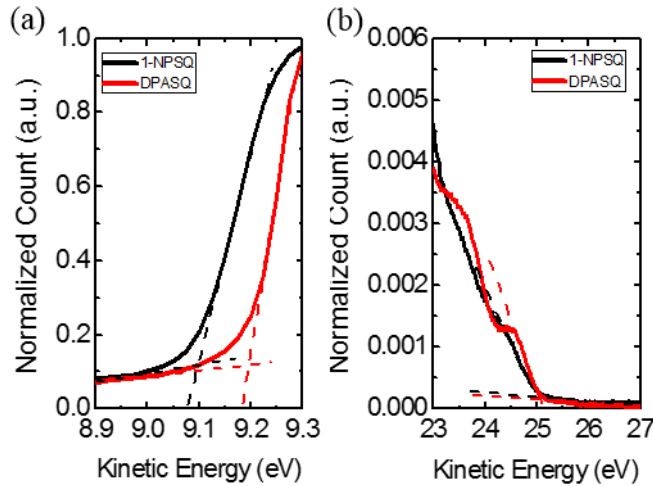
Figure 4.3 Ultraviolet photoelectron spectra of 10Å-thick 1-NPSQ and DPASQ films on indium-tin-oxide-coated glass substrates. (a) Low energy cutoff; and (b) high energy cutoff of the films. The dashed line crossings correspond to intercepts with the energy axis.

The J_{sc} of the blended cells compared with the neat 1-NPSQ cell increases as 1-NPSQ:DPASQ increases to 1:0.5, and then deceases as the ratio is further increased. As expected, this trend is related to changes in the *EQE* spectrum. As shown in Fig. 4.4, the presence of DPASQ in the blend cells partially fills the gap between λ= 500 nm and 600 nm, although the quantum efficiency is significantly lower than its peak for the neat DPASQ cells. Since the absorption spectrum of DPASQ also overlaps with C_{60} (see Fig. 4.1), the *EQE* between λ= 400 nm and 500 nm also increases. However, the 1-NPSQ peak at λ= 700 nm deceases with ρ since the number of 1-NPSQ molecules within an exciton diffusion length of the donor-acceptor junction is reduced with increasing DPASQ concentration. When the DPASQ concentration is too high, the blended film is thicker than the excition diffusion length, leading to the decrease of the peak in *EQE* at 400nm<λ<500nm. Therefore, J_{sc} reaches a maximum for 1:0.5 blends, which is ~8% higher when compared with neat 1-NPSQ cells.
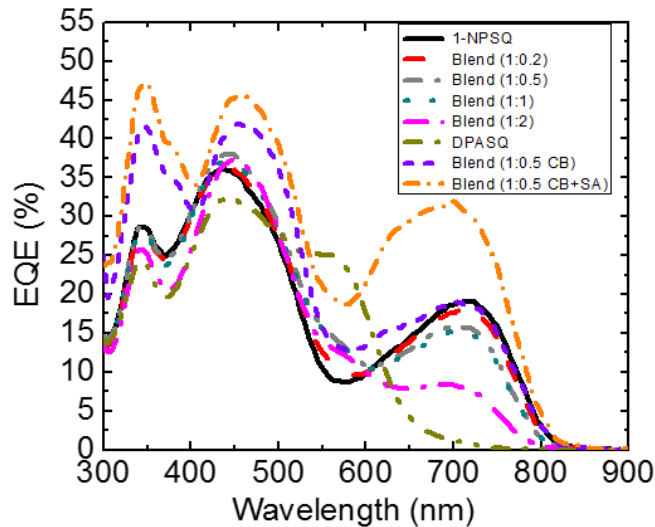
Figure 4.4 External quantum efficiency (*EQE*) spectra of devices in Figure 4.2. Note that the clearly defined feature due to exciton generation in the DPASQ film disappears for the CB and CB+SA films due to a significant increase in the intensity of the C_{60} spectra. The presence of DPASQ results in the broadening of that feature.

Atomic force microscope (AFM) images of surface morphologies for several films are shown in Fig. 4.5. While the neat 1-NPSQ film has a root-mean-square (rms) roughness of rms= 17 ± 1 Å, the surface of the 1:0.5 blend has rms= 8 ± 1 Å, only half that of neat 1-NPSQ films. As the weight ratio of DPASQ further increases, large crystallites are formed, increasing rms to 12 ± 1 Å at a 1:2 ratio. At high ρ, 1-NPSQ determines the film surface morphology, while isolated islands of DPASQ form at the higher weight ratios.
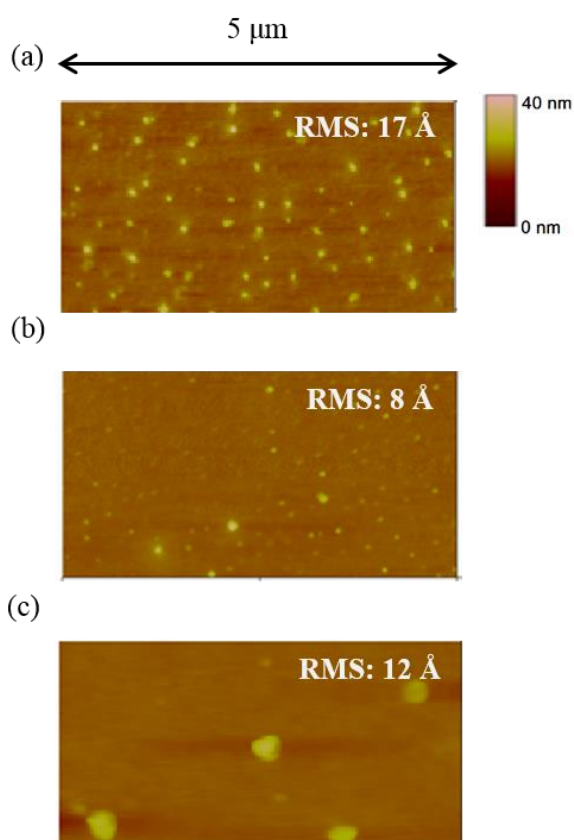
Figure 4.5 Atomic force microscope (AFM) images of (a) a neat 1-NPSQ film; (b) a 1-NPSQ:DPASQ 1:0.5 blend; and (c) a 1:2 blend. Here, RMS indicates the root mean square roughness of the films in the respective images. Small-size surface clusters (possibly crystallites) were observed on neat 1-NPSQ film, which leads to RMS = 17 Å. The surface of 1:0.5 blend is smoother, with fewer clusters and RMS = 8 Å. The 1:2 blend has large clusters, with RMS = 12 Å.

To further understand the performance of the blended cells, the modified ideal diode equation[95-97] $J = J_s \left[\exp\left(\frac{q(V_a - JR_s)}{nk_bT} \right) - \frac{k_{ppd}}{k_{ppd,eq}} \right] + \frac{V_a - JR_s}{R_p}$ is used to fit the *J-V* characteristics in the dark. Here, J_s is the reverse saturation current density, q is the electron charge, V_a is the applied voltage, R_s is the series resistance, n is the ideality factor, k_b is the Boltzmann constant, T is the temperature, and R_p is the parallel (or shunt) resistance. Here, the ratio of the polaron pair dissociation rate to its value at equilibrium is assumed to be $k_{ppd}/k_{ppd,eq} \approx 1$ for simplicity. The use of two donor molecules creates disorder at the donor/acceptor interface, thereby resulting in an increased ideality factor compared with that of the neat 1-NPSQ and DPASQ cells, as shown in Table 4.1. According to Giebink, *et al.*,[97] disorder can lead to increased recombination at the interface due to the high density of traps that may result. The disorder increases with blend ratio, thereby leading to a corresponding increase in *n*. In addition, J_o of the blended cells is increased compared with neat 1-NPSQ and DPASQ cells. The series resistance R_s increases with higher blend ratios indicating reduced hole mobility at high weight ratios. Nevertheless, *PCE* at 1 sun intensity for blended cells reaches 5.1 ± 0.2 % at $\rho = 2$, compared with *PCE*= 4.4 ± 0.1 % for the neat 1-NPSQ cells.

To further optimize cell performance, the 1:0.5 film was solvent-vapor annealed in the presence of dichloromethane vapor for 10 min following deposition of the C_{60} layer. In addition, a 1,4,5,8-napthalene-tetracarboxylic-dianhydride (NTCDA) (150 Å)/PTCBI (50 Å) compound buffer layer was used to cap the blend/C_{60} cell, which further enhances the optical field distribution within the OPV active layer while blocking excitons from quenching at the cathode.[91] For comparison, analogous thermally annealed cells with compound buffer layers were also fabricated.

The short circuit current increases from $J_{sc}= 7.3 \pm 0.2$ mA/cm^2 for the cells without compound buffer layers, to $J_{sc}= 7.8 \pm 0.2$ mA/cm^2 for ones with such buffers, consistent with previous results.[91] As shown in Fig. 4.2 and Table 4.1, the short-circuit current increases further, to $J_{sc}= 10.5 \pm 0.5$ mA/cm^2 for solvent-annealed devices due to a significant increase of *EQE* in both the C$_{60}$ and squaraine absorption regions. The improvement in *EQE* (c.f. Fig. 4.4) upon solvent-annealing is likely due to the improvement in crystallinity of both the C$_{60}$ and blended layers, which leads to an increase in exciton diffusion length and charge mobility.[98] We note that this increase in *EQE* results in the disappearance of a clearly defined shoulder in the C$_{60}$ peak due to exciton generation in the DPASQ. This results from the increased C$_{60}$ peak intensity, where the presence of DPASQ now results in an overall broadening of the long wavelength tail of the C$_{60}$ peak. The open circuit voltage declines from $V_{oc}= 0.98 \pm 0.02$ V for thermal-annealed cells to 0.78 ± 0.02V for solvent-annealed devices, with the fill factors remaining largely unchanged. The reduction in V_{oc} is attributed to the increased concentration of defects at the donor-acceptor interface during the solvent annealing process, thereby reducing V_{oc} due to enhanced polaron-pair recombination.[99] The *PCE* at 1 sun intensity (simulated AM 1.5G spectrum) increases from *PCE*= 5.2 ± 0.2% for thermal annealed cells to 5.9 ± 0.3% for solvent-annealing.

The stability of the blended, unpackaged SQ OPV was tested in N$_2$ and ambient air under 1-sun illumination. The OPV cell in N$_2$ retains about 70% of its initial *PCE* after 6 h while the *PCE* of a cell exposed to the ambient air reduces to 30% of its initial value. The degradation is primarily due to a decrease in J_{sc} and *FF*, while V_{oc} remains approximately constant over this testing period.

4.5 Conclusions

In summary, we have demonstrated that blended 1-NPSQ:DPASQ donor layers can lead to an increased J_{sc} as compared to neat, single component donors. This results from increased absorption between $\lambda = 450$ nm and 600 nm, the location of the gap in the *EQE* spectrum between C_{60} and 1-NPSQ peaks, and enhanced V_{oc} due to the deeper HOMO energy of blended film compared with neat 1-NPSQ. The power conversion efficiency at 1 sun intensity increases from *PCE* $= 4.4 \pm 0.1\%$ for neat 1-NPSQ cells to *PCE* $= 5.1 \pm 0.2\%$ for blend cells at an optimal 1-NPSQ:DPASQ ratio of 1:0.5. Furthermore, by solvent-annealing a blended device employing a compound, PTCBI/NTCDA exciton blocking layer, the power conversion efficiency of blended cells increases to 5.9 ± 0.3 % at 1 sun intensity due to a significant increase of J_{sc} in spite of a small reduction of V_{oc}.

Chapter V

Tandem and multi-junction OPV cells

As discussed in Chapter I, single junction OPV cells usually suffer from limited absorption ranges and thermalization losses. To overcome these limits and achieve higher efficiencies, tandem and multi-junction OPV cells comprised of two or more single junctions connected in series have been developed. Previously, our group demonstrated a tandem cell incorporating a solution-processed 2,4-bis[4-(N,Ndiphenylamino)-2,6-dihydroxyphenyl] squaraine (DPSQ)/C_{70} bilayer HJ and a vacuum-deposited subphthalocyaninechloride (SubPc):C_{70} graded HJ as sub-cells with a *PCE* = 6.6 ± 0.1 % under simulated AM 1.5G illumination at one sun intensity[61]. This tandem cell, however, suffers from a low *FF* and J_{SC} limited by the SubPc:C_{70} graded HJ and DPSQ/C_{70} bilayer HJ, respectively, which ultimately hinders the further improvement on the device performance of tandem cells.

In this chapter, we employ DBP:C_{70} PM-HJ as the blue-green-absorbing sub-cell, which has a higher FF than SubPc:C_{70} HJ, paired with various NIR-absorbing sub-cells to achieve higher efficiency tandem cells. The blended *f*SQ/C_{70} bilayer HJ developed in Chapter 4 is first used as a NIR-absorbing sub-cell in the tandem to increase the total J_{SC}. The new tandem cell exhibits considerable improvement in both J_{SC} and *FF* leading to a *PCE* = 8.3 ± 0.4 % under simulated AM1.5G illumination at one sun intensity, significantly higher than that of the previous tandem. Furthermore, we implement a vacuum-deposited NIR donor, 2-((7-(5-(dip-

tolylamino)thiophen-2-yl)benzo[c][1,2,5]thiadiazol-4-yl)methylene)malononitrile (DTDCTB), paired with C_{60} in a PM-HJ to enhance the absorption in the NIR spectral range and minimize the absorption overlap between two sub-cells, resulting in a significant improvement in J_{SC} and, thus, *PCE*. Finally, we develop triple and four-junction OPV cells which enable the photon harvesting at the second order optical interference maxima across the visible and NIR, leading to a further improvement of *EQE* and *PCE* of multi-junction cells.

5.1 Tandem OPV cells incorporating DBP:C_{70} PM-HJ and blended *f*SQ/C_{70} bilayer HJ

The tandem cell previously developed in our group [47] suffers from low J_{SC} and *FF* ultimately limiting its *PCE*. J_{SC} of the previous tandem is primarily limited by the front sub-cell, DPSQ/C_{70} bilayer HJ, due to its limited donor/acceptor interface and thin photoactive layers restricted by its L_D. To improve the photocurrent of the front sub-cell, we employ a blended *f*SQ/C_{70} HJ which we demonstrated in Chapter 4 as a NIR-absorbing sub-cell. In this case, a blend of DPASQ and DPSQ at a 4:6 vol. ratio is implemented as the donor layer along with a 10nm-thick C_{70} layer as the photoactive region (see Fig. 5.1(a)). Solvent-annealing is applied after the deposition of PTCBI layer to enhance the crystallinity of organic photoactive layers while preserving the donor/acceptor interface to maintain the V_{OC} [27]. The charge generation layer (CGL) is comprised of PTCBI (5 nm)/Ag(0.1 nm)/MoO_3 (5 nm). Additionally, a 30nm thick MoO_3 layer is grown on the front sub-cell to mimic the optical field inside the tandem.

On the other hand, the *FF* of the previous tandem is restricted by SubPc:C_{70} graded HJ owing to the low hole mobility of SubPc (~10^{-6} cm^2/(V·s)) [63]. To improve *FF* of the blue-green-absorbing sub-cell, we employ DBP, which has a higher hole mobility (~10^{-4} cm^2/(V·s))

[33], to replace SubPc as the green-absorbing donor. As we discuss in Chapters 2 and 3, DBP:C_{70} PM-HJ can achieve a high $FF = 66 \pm 1\%$ with a mixed buffer, significantly higher than that of SubPc:C_{70} graded HJ which is only $48 \pm 1\%$ [29, 47]. Thus, we replace SubPc:C_{70} graded HJ with DBP:C_{70} PM-HJ as a blue-green-absorbing sub-cell in the tandem. By optimizing the blend ratio of DBP:C_{70}, we find the ratio of 1:10 is better than 1:8 due to further separated absorption spectra between two sub-cells along with an improved FF. The optimized device structures of the tandem and sub-cells are shown in Fig. 5.1.
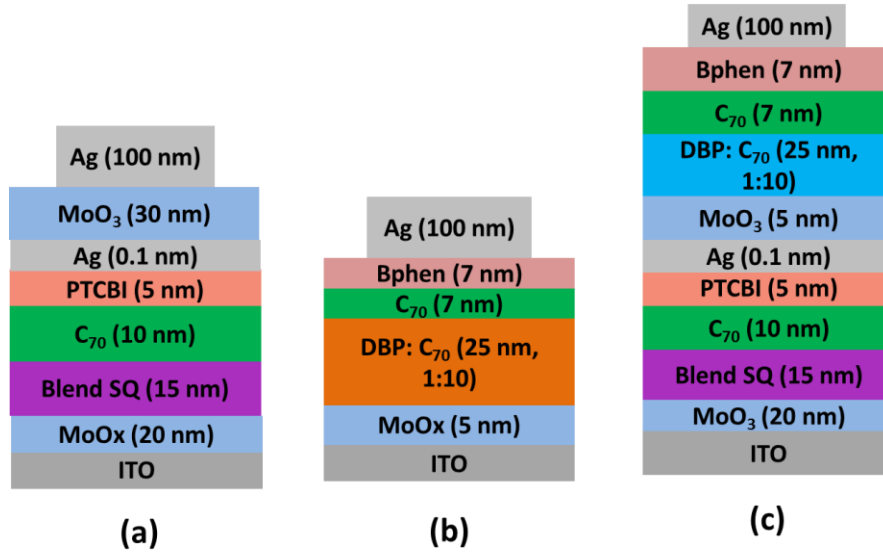
Figure 5.1 Device structures of (a) front sub-cell; (b) back sub-cell; and (c) tandem cell.

Figure 5.2(a) shows the measured $J\text{-}V$ characteristics for both the discrete cells (circles and triangles), and the tandem device (squares), with $V_{OC} = 1.85 \pm 0.01$ V, $FF = 61 \pm 1$ %, $J_{SC} = 7.4 \pm 0.4$ mA/cm^2, and $PCE = 8.3 \pm 0.4\%$. The V_{OC} of the tandem is almost identical to the sum of two sub-cells indicating the CGL is electrically lossless. The lines in Fig. 5.2(b) show the calculated EQE for each sub-cell as it behaves in the tandem (red dashed line for the blended squaraine cell, blue dotted line for the DBP:C_{70} cell) and the sum of the $EQEs$ of the sub-cells

(black solid line) showing the overall percent of photons contributing to current in the tandem OPV. The tandem cell harvests >60% of the photons at $\lambda < 600$ nm, and >40% at $\lambda < 750$ nm.
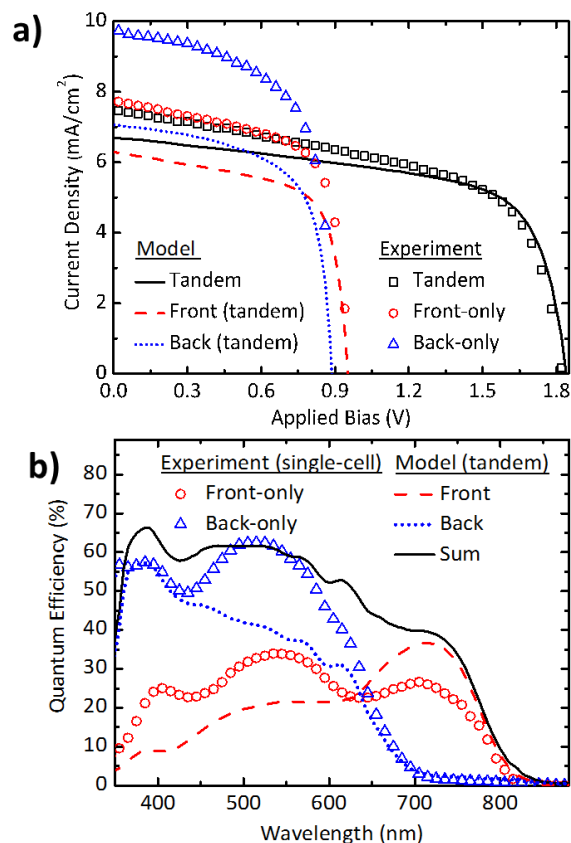
Figure 5.2 Device performance of the tandem cell and sub-cells. (a) Current density-voltage characteristics in the 4th quadrant under simulated AM1.5G illumination at one sun intensity for front-only (circle), back-only (triangle), and tandem (square) cells, along with characteristics extrapolated from the model for the front sub-cell (dashed line) and back sub-cell (dotted line) for the optical fields in the tandem structure and the predicted tandem (solid line) response. (b) *EQE* spectra for front-only (circle) and back-only (triangle) organic photovoltaic cells, along with extrapolated spectra for front sub-cell (dashed line), back sub-cell (dotted line), and the sum of the two sub-cells (solid line).

Compared to the previous tandem cell, the new tandem cell with DBP:C_{70} PM-HJ and blended fSQ/C_{70} HJ shows significant improvement in J_{SC} and FF, leading to a 25% increase in

PCE. To further understand the improvement, we compare two tandem designs by calculating the power conversion efficiency penalty $\Delta\eta$ described by [100]

$$\Delta\eta = 1 - \frac{J_{M-T}V_{M-T}}{\sum_{i=1}^{N} J_{M-i}V_{M-i}}, \tag{5.1}$$

where V_{M-i} and J_{M-i} are the voltage and current density at the maximum power point (MPP) of the sub-cell i, respectively, and V_{M-T} and J_{M-T} are the device parameters of the tandem cell. As shown in Figs. 5.3(a) and (b), the previous tandem cell has a $\Delta\eta$ = 21.4%, whereas $\Delta\eta$ of the new tandem is only 11.7 %. In the new tandem structure, the closer MPPs for two sub-cells and the tandem due to improved J_{SC} and *FF* of both tandem and sub-cells lead to a smaller $\Delta\eta$ and higher *PCE* of the tandem cell.
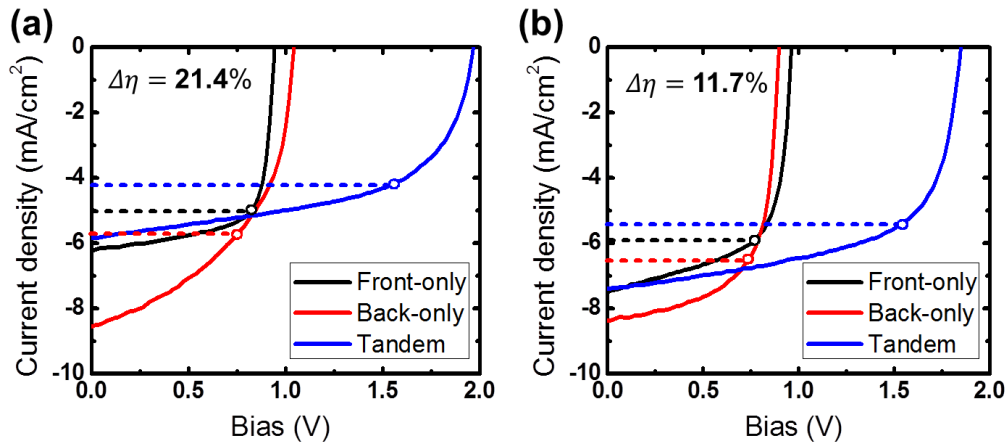
Figure 5.3 Current density-voltage characteristics of the front-only, back-only and tandem cell for (a) the previous tandem incorporating DPSQ/C_{70} bilayer HJ and SubPc:C_{70} graded HJ and (b) the new tandem incorporating blended *f*SQ/C_{70} bilayer HJ and DBP:C_{70} PM-HJ. Circles show the maximum power point for each device. The power conversion efficiency penalty $\Delta\eta$ is shown on each plot.

5.2 Fully vacuum-deposited OPV tandem cells

To further improve the device performance, we begin by analyzing the primary losses in the tandem cell described in section 5.1: (a) the quantum efficiency in the NIR is relatively low, only ~30% (see Fig. 5.2(b)), resulting from the thin layer of blended fSQ limited by its short exciton diffusion length; (b) there are considerable spectral overlaps between the elements in the tandem that prevent photons from reaching the back sub-cell, ultimately limiting the total photocurrent; (c) CGL with a PTCBI blocker have a significant absorption loss in the visible. Therefore, we employ several strategies accordingly to reduce these losses.

5.2.1 Vacuum-deposited NIR-absorbing donor

To mitigate the problem of inefficient absorption in the NIR resulting from the short exciton diffusion length, a vacuum-deposited NIR-absorbing PM-HJ is employed as a sub-cell since the PM-HJ is not limited by L_D, but rather the much larger charge collection length[28]. Meanwhile, to overcome the deficiency of spectral overlap, we use two relatively thick and strongly absorbing, vacuum-deposited PM-HJ sub-cells with considerable separation between their absorption maxima, therefore maximizing the total photocurrent in the tandem. The front sub-cell adjacent to the transparent anode consists of a sublimable NIR-absorbing donor, 2-((7-(5-(dip-tolylamino)thiophen-2-yl) benzo[c][1,2,5] thiadiazol-4-yl)methylene)malononitrile (DTDCTB) (see Fig. 5.4(a)), blended with C_{60}. In the front cell, the C_{60} intermolecular charge transfer (CT) absorption feature in the visible is greatly suppressed when diluted in DTDCTB, providing a spectrally complementary system with the back sub-cell. Thus, the tandem cell has a broad coverage of solar spectrum from $\lambda = 350$ nm to 900 nm.

The low energy gap DTDCTB absorbs at wavelengths as long as $\lambda = 900$ nm. To separate the front (i.e. that nearest the cathode) and the back sub-cell (nearest the anode) absorption spectra, the blue-green absorbing C_{60} is used as the acceptor, whereas the broadly absorbing C_{70} is employed solely in the back sub-cell. The extinction coefficients (k) of the DTDCTB:C_{60} film is shown in Fig. 5.4(b).
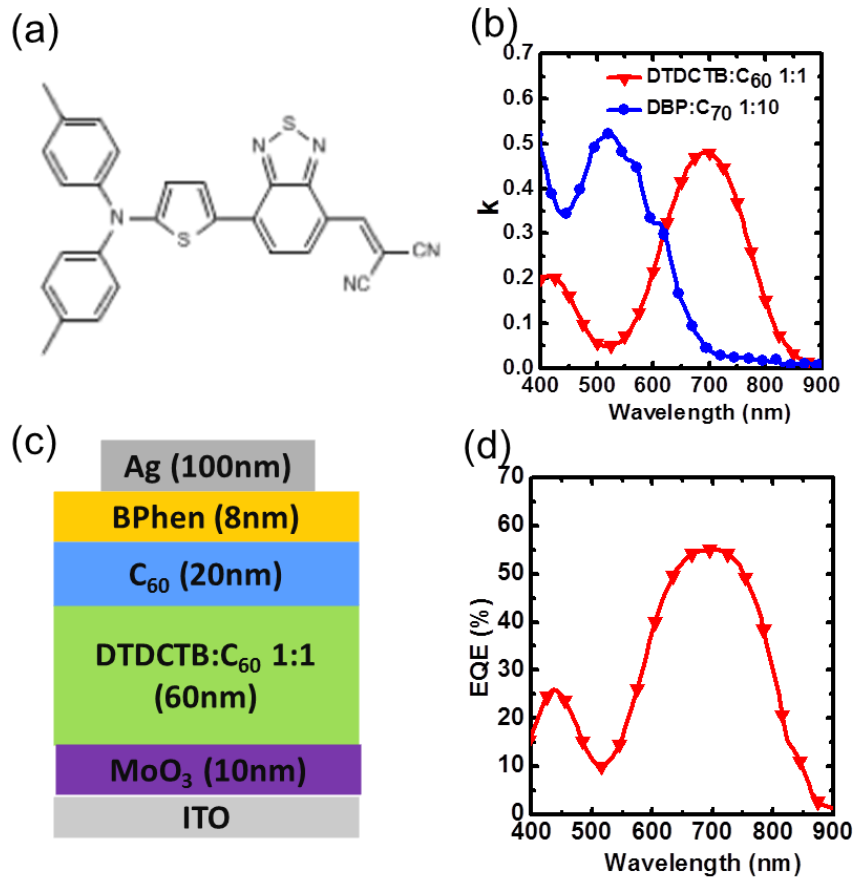
Figure 5.4 (a) Molecular structure of DTDCTB; (b) absorption spectra of DTDCTB:C_{60} and DBP:C_{70} films; (c) device structure of DTDCTB:C_{60} PM-HJ; (d) *EQE* spectrum of the device in (c).

An optimized DTDCTB:C_{60} single junction photovoltaic cell has the following structure shown in Fig. 5.4(c): ITO/MoO$_3$ (10 nm)/DTDCTB:C_{60} (60 nm, 1:1 ratio by vol.)/C_{60} (20

nm)/Bathophenanthroline (BPhen, 8 nm)/Ag (100 nm). The MoO_3 serves as the anode buffer layer due to its large work function, high transmittance, and low resistance[101], and BPhen is used as the exciton blocking buffer layer adjacent to the cathode[102]. The device exhibits V_{OC} = 0.82 ± 0.01V, J_{SC} = 13.7 ± 0.2 mA/cm^2, and fill factor FF = 0.55 ± 0.01. This corresponds to a PCE = 6.2 ± 0.1% at 1 sun, AM 1.5G illumination. At this blend ratio, the CT absorption by C_{60} is suppressed to only 40% of its value in the neat film. Accordingly, the DTDCTB:C_{60} cell shows an external quantum efficiency of $EQE > 55\%$ at $\lambda = 700$ nm, falling off to $< 25\%$ at $\lambda < 500$ nm (see Fig. 5.4 (d)). As shown below, this NIR absorbing front sub-cell has minimal spectral overlap with the principally green-absorbing DBP:C_{70} back sub-cell. In addition, the optimized structure of the back sub-cell is: ITO/MoO_3 (5 nm)/DBP:C_{70} (30 nm, 1:10 ratio by vol.)/C_{70} (7 nm)/BPhen (7 nm)/Ag (100 nm), resulting in J_{SC} = 11.3 ± 0.2 mA/cm^2, V_{OC} = 0.90 ± 0.01 V, FF = 0.61 ± 0.01 and PCE = 6.2 ± 0.1%, comparable to that of the front sub-cell.

The extinction coefficient of the 1:1 DTDCTB:C_{60} and the 1:10 DBP:C_{70} blends, are shown in Fig. 5.4 (b). The DBP:C_{70} film exhibits a broad spectral response at $\lambda < 700$ nm, while the DTDCTB:C_{60} layer primarily absorbs from $\lambda = 500$ nm to 900 nm. By stacking these two sub-cells, absorption spans the wavelengths from $\lambda = 350$ nm to 900 nm, thereby covering a large portion of solar spectrum with only minimal overlap between the constituent devices. The tandem thus harvests light efficiently with good current match between the sub-cells.

5.2.2 Highly transparent interconnecting layer

The PTCBI layer in CGL has a significant absorption loss in the visible as shown in Fig. 5.5(a). Hence, for cell interconnection, we employed a previously reported transparent exciton blocking and electron conducting BPhen:C_{60} electron filter[103-104]. Figs. 5.5 (b) and (c) show

the simulated optical field distribution within the tandem cell, comparing a 5 nm thick PTCBI with a similarly thick BPhen:C_{60} mixed buffer. As the dashed white rectangle indicates, the BPhen:C_{60} is transparent, in striking contrast with the PTCBI buffer. The simulation also shows that both sub-cells fit within the first interference maximum of the optical field.
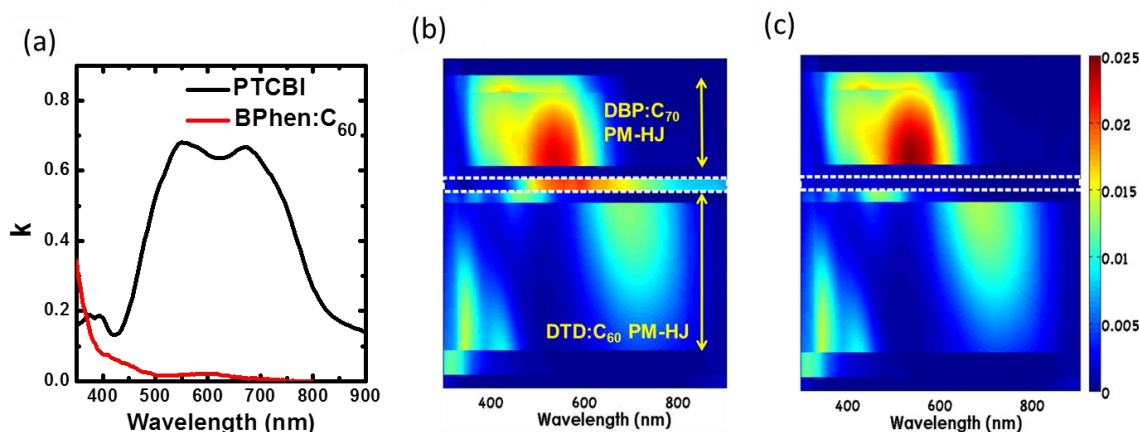
Figure 5.5 (a) Extinction coefficients of PTCBI and 1:1 BPhen:C_{60} mixed layer. (b-c) Calculated absorbed optical power in tandem cells with different interconnecting layers: (b) PTCBI; (c) BPhen:C_{60}.

5.2.3 Device performance

The optimized device structure of the tandem cell is shown in Fig. 5.6(a) and the fourth quadrant *J-V* characteristics of tandems utilizing two different interconnecting layers, namely, PTCBI and BPhen:C_{60}, are shown in Fig. 5.6(b). As expected, when PTCBI is replaced with BPhen:C_{60}, J_{SC} increases from 11.6 ± 0.2 mA/cm^2 to 12.3 ± 0.2 mA/cm^2 in the front sub-cell, with no significant change in *FF*. Hence, the efficiency of the front sub-cell increases from $5.7 \pm 0.1\%$ to $6.0 \pm 0.1\%$. Also from Fig. 5.5 (c), the optical field in the DBP:C_{70} sub-cell is enhanced when using BPhen:C_{60}, leading to a corresponding increase in current. Consequently, J_{SC} of the tandem cell is increased to 9.9 ± 0.2 mA/cm^2, which shows significant improvement over the previously reported small molecule tandem cells.[105-107] The results of the cell using

BPhen:C_{60} along with Ag nanoparticles as the interconnecting layer, whose structure and optimized layers thicknesses are shown in Fig. 5.6 (a), match the modeled performance summarized in Table 5.1.
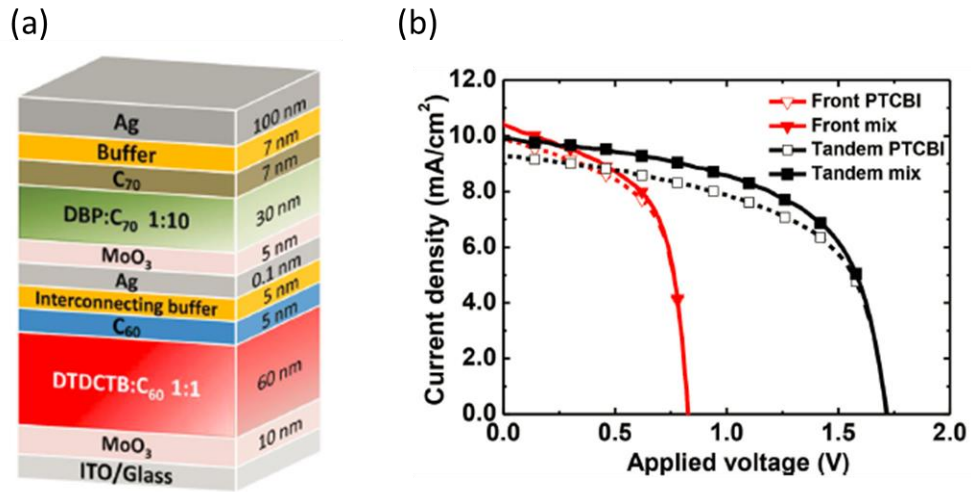
Figure 5.6 (a) Device structure of the optimized tandem cell; (b) Current density-voltage characteristics of the tandem and front-only cell with two different interconnecting layers.

Table 5.1 Measured (meas) and calculated (calc) tandem sub-cells, tandem cell and triple-junction cell performances.

Cells*	J_{SC} (mA/cm^2)	V_{OC} (V)	FF	PCE (%)	M
Front (meas)	12.3 ± 0.2	0.82 ± 0.01	0.59 ± 0.01	6.0 ± 0.1	0.93 ± 0.01
Front (calc)	9.6	0.82	0.57	4.5	/
Back (meas)	11.3 ± 0.2	0.90 ± 0.01	0.61 ± 0.01	6.2 ± 0.1	1.00 ± 0.01
Back (calc)	9.6	0.90	0.61	5.3	/
Tandem (meas)	9.9 ± 0.2	1.72 ± 0.01	0.59 ± 0.01	10.0 ± 0.2	0.95 ± 0.01
Tandem (calc)	9.9	1.72	0.58	9.9	/
Triple (meas)	7.3 ± 0.2	2.58 ± 0.01	0.59 ± 0.02	11.1 ± 0.2	0.97 ± 0.01
Triple (calc)	7.7	2.62	0.61	12.3	/

[*] 'Front" refers to the DTDCTB:C_{60} PM-HJ nearest the anode in the tandem; 'Back' refers to the DBP:C_{70} PM-HJ close to the cathode in the tandem; 'Tandem' employs a BPhen:C_{60} interconnecting buffer layer; 'Triple' employs a second DBP:C_{70} sub-cell as the front cell in additional to the tandem structure. Measured J_{SC} and PCE are spectrally corrected. Errors indicate device-to-device variations of samples produced in the same growth cycle; an addition ~ 5% of systematic error applies to J_{SC} and PCE.

The optimized tandem cell EQE shown in Fig. 5.7 (a) is similar to that employing a conventional PTCBI buffer, although the measured front sub-cell peak EQE increased from 50% to 53%. Fig. 5.7(a) shows measured and calculated 4th quadrant J-V characteristics. The calculated tandem J-V characteristics agree with measurement, suggesting that the models of optical field distribution and charge collection are predictive of performance, thereby simplifying device layer thickness design. The optimized tandem OPV cell achieves a measured $J_{SC} = 9.9 \pm 0.2$ mA/cm^2 ($M = 0.95 \pm 0.01$), $V_{OC} = 1.72 \pm 0.01$ V, $FF = 0.59 \pm 0.01$, with $PCE = 10.0 \pm 0.2\%$. This represents an approximately 60% improvement over the discrete cell efficiencies comprising the stack. Furthermore, the tandem V_{OC} is equal to the sum of the constituent sub-cells, suggesting that the interconnecting charge recombination layer is lossless.

(a)

(b)
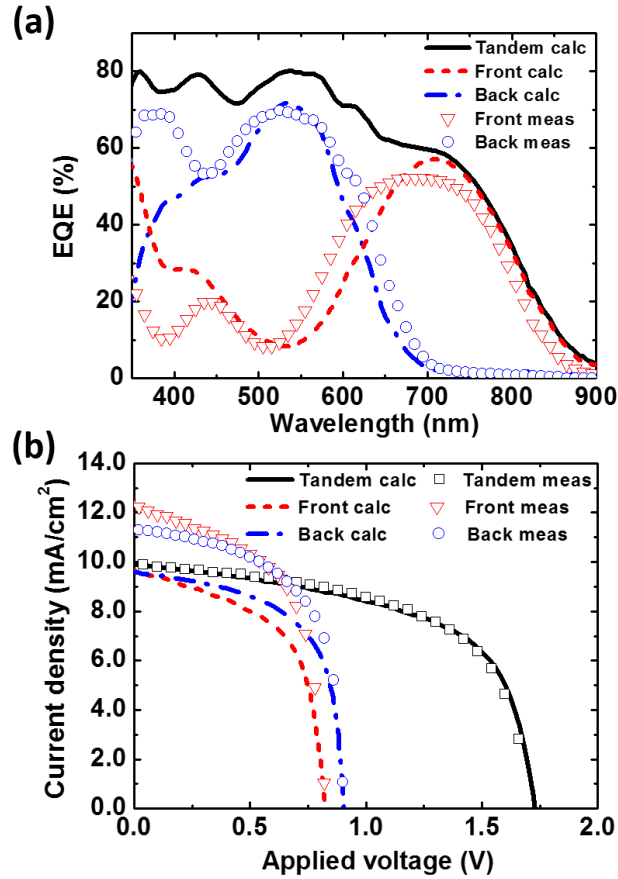
Figure 5.7 Device performance of the optimized tandem cell: (a) Measured (dots) and calculated (lines) *EQE* spectra of the front (dash; triangle), back (dash-dot; circle) and tandem cell (solid line; square); (b) current density-voltage characteristics in 4th quadrant for the same devices in (a).

5.3 Triple junction OPV cells

To take further advantage of the optical field distribution and achieve even higher V_{OC}, an additional DBP:C_{70}(1:10) sub-cell is inserted as the front cell in the stack. Figure 5.8(a) shows the structure of the triple junction cell, where the middle DTDCTB:C_{60} (1:1) cell is sandwiched between two DBP:C_{70} (1:10) sub-cells. The BPhen:C_{60} interconnecting layers are used between the sub-cells to ensure minimal absorption loss. Compared with the tandem cell, the thicknesses

of the back DBP:C_{70} and the middle DTDCTB:C_{60} cells are increased over that used in the tandem such that the front, short-wavelength absorbing DBP:C_{70} sub-cell fits into the second order optical interference maximum, as shown in Fig. 5.8(b). The front and back green-absorbing cells absorb at different optical maxima to efficiently harvest short wavelength photons while complementing the absorption of the middle NIR-absorbing cell. Similar to the tandem cell, the thicknesses of each active layer is optimized by simulation to achieve current balance between sub-cells at 1 sun intensity.

The *J-V* characteristics of the triple-junction and tandem cells are compared in Fig. 5.8(c), with performance parameters listed in Table 5.1. Compared with the tandem, the V_{OC} increases to 2.58 ± 0.01V. Although J_{SC} decreases to 7.3 ± 0.2mA/cm^2, the optimized triple junction cell achieves a *PCE* = 11.1 ± 0.2%. Figure 5.8(c), inset, shows that the calculated quantum efficiency at wavelengths from 400 nm to 700 nm approaches 100% in the triple-junction cell due to contributions from the two DBP:C_{70} sub-cells at the different interference maxima. Note that its V_{OC} is 0.04V lower than the sum of its sub-cells, mainly due to the reduced optical intensity in each active layer.
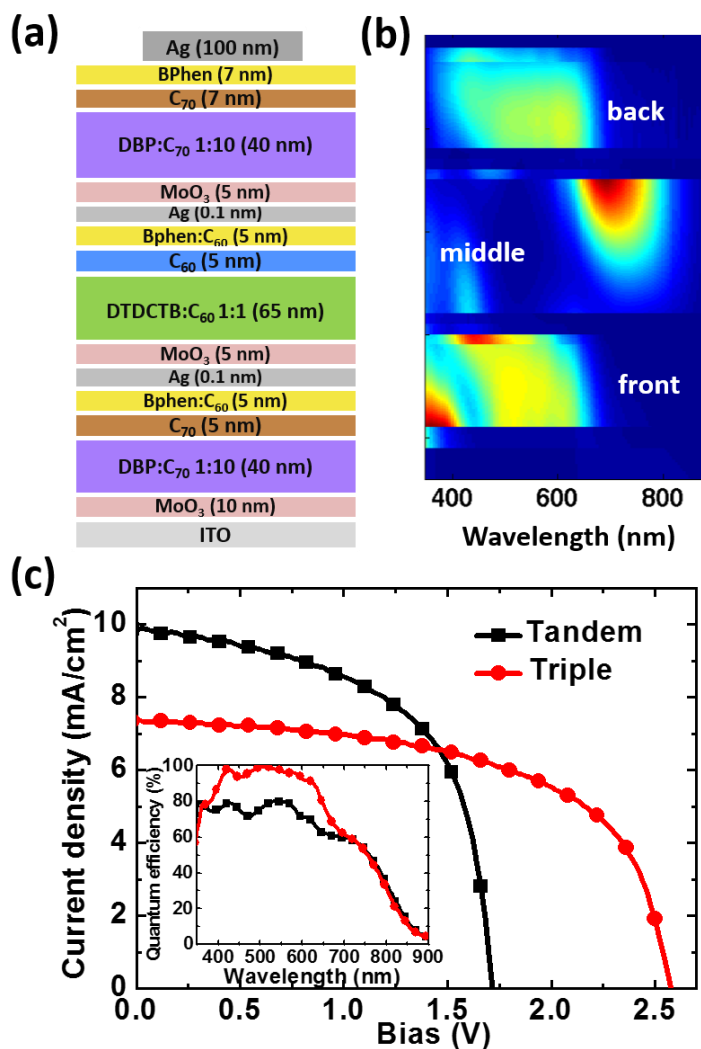
Figure 5.8 Triple-junction OPV cell: (a) device structure and (b) calculated optical field distribution of the three sub-cells in the stack; (c) measured current density-voltage characteristics of tandem and triple-junction cells. *Inset*: Calculated quantum efficiencies for the tandem and triple-junction cells.

5.4 Four-junction OPV cells

As shown in the inset of Fig. 5.8(c), the *EQE* significantly increases in the visible with the additional DBP:C_{70} PM-HJ in the triple junction cell due to the enhanced photon harvesting at the second order optical interference maxima in the visible. The *EQE* in the NIR, however, is

still relatively low. Therefore, we add another DTDCTB:C_{60} PM-HJ at the anode side (see Fig. 5.9(a)) to further improve the absorption at the second order optical interference maxima in the NIR spectral range.
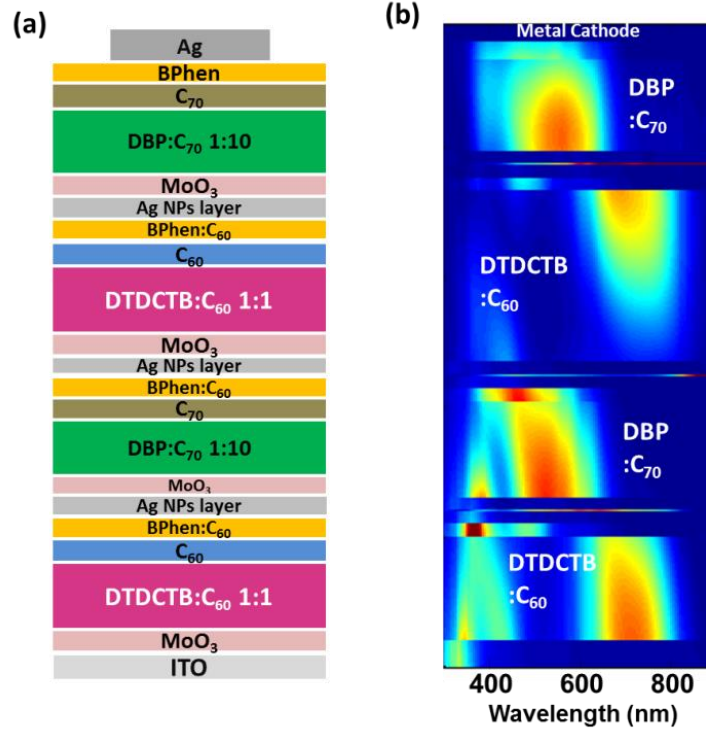
Figure 5.9 Four-junction cell: (a) device structure and (b) calculated optical power distribution inside the four-junction cell.

Figure 5.9(a) shows the device structure of a four-junction OPV cell. Two DBP:C_{70} and DTDCTB:C_{60} PM-HJ are arranged in an alternating order such that photons from visible to NIR at both the first and second optical interference maxima can be efficiently harvested by each sub-cell accordingly as shown in Fig. 5.9(b). Compared to the triple junction, the *EQE* in the NIR increases owing to the enhanced absorption in the NIR with the presence of the second DTDCTB:C_{60} PM-HJ whereas the *EQE* in the visible are almost identical in both cells (see Fig. 5.10(a)). Figure 5.10(b) shows *J-V* characteristics of optimized tandem, triple and four-junction

cells, with the device performance summarized in Table 5.2. For the four-junction cell, the V_{OC} increases up to 3.38 ± 0.01V in spite of a slight decrease in J_{SC} while FF remains almost the same. Thus, the optimized four-junction cell achieves a $PCE = 12.6 \pm 0.2\%$ under simulated AM 1.5G illumination at one sun intensity. It is worth noting that the accurate measurement of multi-junction OPV cells is challenging compared to single junction and multi-junction inorganic cells, resulting from considerably large overlaps in the absorption spectra between sub-cells in multi-junction OPV cells. We have developed a method with a combination of modeling and experiment for the accurate measurement of multi-junction OPV cells. Details of this method are discussed in Appendix A.
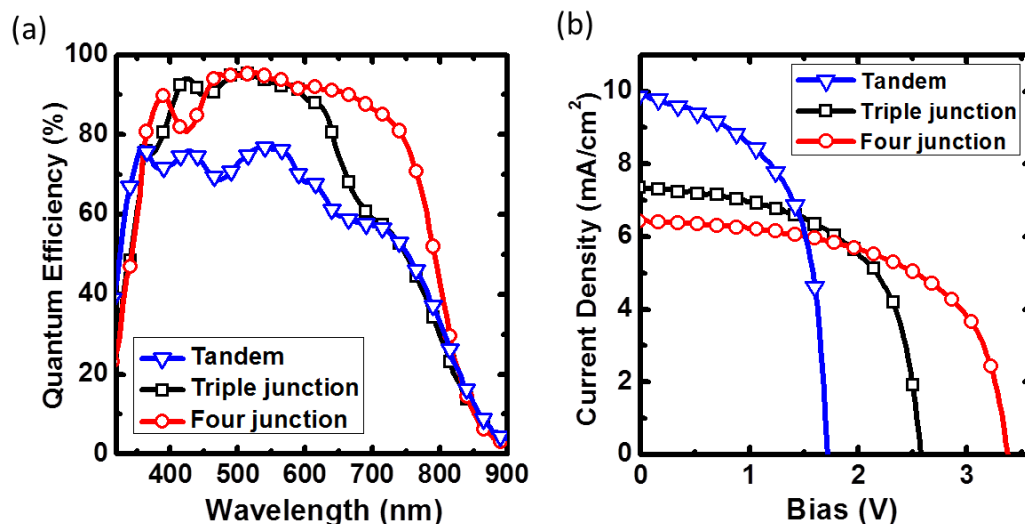
Figure 5.10 (a) Quantum efficiency spectra of tandem, triple and four junction OPV cells; (b) current density-voltage characteristics of the same devices in (a) under simulated AM 1.5G illumination at one sun intensity.

Table 5.2 Device performance of tandem, triple and four junction OPV cells

Cells*	J_{SC}	V_{OC}	FF	PCE
	(mA/cm^2)	(V)		(%)
Tandem	9.9 ± 0.2	1.72 ± 0.01	0.59 ± 0.01	10.0 ± 0.2
Triple junction	7.3 ± 0.2	2.58 ± 0.01	0.59 ± 0.02	11.1 ± 0.2
Four junction	6.4 ± 0.2	3.38 ± 0.01	0.58 ± 0.02	12.6 ± 0.2

5.5 Conclusions

In summary, we demonstrated tandem and multi-junction OPV cells employing DBP:C_{70} PM-HJ as a blue-green-absorbing sub-cell paired with a variety of NIR-absorbing sub-cells. A blended fSQ/C_{70} bilayer HJ is first employed to increase the photon harvesting in the NIR leading to an improved J_{SC} and PCE. To further enhance the absorption in NIR and minimize the absorption overlap between sub-cells, we replace the blended fSQ/C_{70} bilayer HJ with a vacuum-deposited DTDCTB:C_{60} PM-HJ, along with a BPhen:C_{60} mixed layer in CGL, resulting in a significant increase in J_{SC}. The optimized tandem cell achieves a $PCE = 10.0 \pm 0.2\%$ under simulated AM 1.5G, 1 sun illumination. Furthermore, we develop triple and four-junction OPV cells by incorporating additional DBP:C_{70} and DTDCTB:C_{60} PM-HJ sub-cells in the stack to enable the photon harvesting at the second order optical interference maxima. The quantum efficiency of multi-junction cells is considerably enhanced across the visible and NIR leading to a $PCE = 11.1 \pm 0.2\%$ and $12.6 \pm 0.2\%$ for the triple and four-junction cells, respectively.

Chapter VI

Inverted, semitransparent small molecule photovoltaic cells

Semitransparent OPV cells are of interest due to their potential for fulfilling building integrated PV needs such as deployment on windows and other architectural surfaces. Moreover, semitransparent OPV cells can also be integrated into tandem and multi-junction structures to achieve a high power conversion efficiency along with acceptable transparency for these applications. The *PCE* of small molecule semitransparent OPV cells based on bilayer or mixed HJ structures have been relatively low since the former is limited by short exciton diffusion lengths, whereas the latter suffers from the lack of continuous paths for charge extraction[108-115]. In contrast, considerable progress has been made on the solution-processed semitransparent bulk heterojunctions OPV cells[116-117].

In this chapter, we demonstrate vacuum-deposited small molecule semitransparent OPV cells based on both mixed and hybrid planar-mixed heterojunctions (PM-HJ) with inverted structures. The fill factor increases from 0.53 ± 0.01 for the mixed HJ to 0.58 ± 0.01 for the PM-HJ due to reduced series resistance, whereas internal quantum efficiency increases from an average of 75% to 85% between the wavelengths of $\lambda = 450$ nm to 550 nm. The inverted, semitransparent PM-HJ cell achieves a power conversion efficiency of $PCE = 3.9 \pm 0.2\%$ under simulated AM1.5G illumination at one sun intensity with an average optical transmission of $\overline{T} = 51 \pm 2\%$ across the visible spectrum, corresponding to >10 % improvement compared with the

mixed HJ cell. We also demonstrate an inverted semitransparent tandem cell incorporating two PM-HJ sub-cells with different absorption spectra. The tandem cell achieves a $PCE = 5.3 \pm 0.3\%$ under simulated AM1.5G at one sun intensity with $\overline{T} = 31 \pm 1\%$ across the visible. Almost identical efficiencies are obtained for tandem cells illuminated via either the cathode or anode surfaces.

6.1 Inverted structures for semitransparent OPV cells

We employ an inverted structure, using a hole blocking/electron selective sol-gel ZnO layer as a cathode buffer on top of an ITO contact, for the semitransparent cells. The ZnO has a high electron mobility[118] of ~10 cm^2/V·s, 98% transmission in the visible and near infrared (NIR) spectral regions, and a work function of 4.5 eV[68], leading to efficient electron collection and low optical loss. In addition, ZnO-based inverted structures eliminate thin but optically lossy metal layers that have been reported previously[108, 111, 114, 119] although highly transparent metal-based electrodes have been recently demonstrated[120]. It is worth noting that conventional OPV structures using wide energy gap molecules, e.g. Bathophenanthroline (BPhen), as cathode buffers cannot employ symmetric ITO contacts due to the lack of electron-transporting defect states induced by the electrode deposition, whereas inverted structures enable the implementation of metal oxides, e.g. MoO_3, as the buffer for the top electrode to efficiently extract charge carriers without the concern of defect states. Meanwhile, the sol-gel ZnO cannot be employed on top of organic layers due to the damage on organic photoactive regions underneath during the solution process.

6.2 Experiments

The photovoltaic cells were grown on glass substrates with pre-patterned ITO (4.2 mm $\times$ 3.5 mm patterns, sheet resistance: 15 Ω/sq). The materials used in OPV cells were obtained from commercial venders: zinc acetate dehydrate, 2-methoxyethanol and ethanolamine (Sigma-Aldrich), DBP, DTDCTB and BPhen (Lumtec), C_{70} (SES Research), C_{60} (MER) and MoO_3 (Alfa Aesar). The glass/ITO substrates were cleaned by successive ultrasonication in Tergitol® (Sigma-Aldrich), deionized water, and a series of organic solvents, followed by ultraviolet ozone exposure for 10 min. The ITO surface was coated with ZnO, deposited using a precursor solution prepared by dissolving 0.5 M zinc acetate dihydrate in 2-methoxyethanol with ethanolamine added as a stabilizer[57]. The solution was passed through a 0.45 µm pore, polyvinylidene fluoride filter, and then spun-cast onto the substrates at 3000 rpm for 30 s. The film was thermally annealed in ambient at 150 $^{\circ}$C for 30 min. The substrates were transferred into a high vacuum chamber with a base pressure of 10^{-7} torr where organic layers were deposited. The mixed organic layers were deposited at a total rate of 0.1 nm/s except for DBP:C_{70} mixtures with a total deposition rate of 0.18 nm/s, whereas neat layers were deposited at a rate of 0.1 nm/s. The densities of organic materials were set at 1.1 g/cm^3 for vacuum thermal evaporation. Top contacts consisting of 100 nm thick ITO with a sheet resistance of 30 Ω/sq were sputter-deposited at a base pressure of 7×10^{-8} torr and a deposition rate of 0.04 nm/s through a shadow mask with an array of 11 mm^2 openings oriented perpendicular to the ITO contact patterns on the substrate. Completed devices were directly transferred into a high-purity N_2-filled glove box with both H_2O and O_2 concentrations of <0.1ppm. There, *J-V* and *EQE* measurements were performed. The light intensity of solar simulator (ASAHI SPECTRA, HAL-320) was characterized by a National Renewable Energy Laboratory (NREL) traceable Si reference cell,

with J_{SC} and *PCE* corrected for spectral mismatch.[82, 121] The tandem cells were measured under simulated AM 1.5G illumination at one sun intensity (25 ± 1 ^{o}C, 1000 W/m^{2}, ASTM G173-03). The *EQE* measurements were performed using monochromated light from a 200 Hz chopped Xe-lamp without other light bias. The OPV cells were measured under illumination with and without masks with known apertures and the device performances were identical in both cases. The measured J_{SC} for single junction cells were consistent with the integrated J_{SC} over the *EQE* spectra with a difference of <3%. Transmission spectra of unpatterned films were obtained using a spectrometer (Perkin-Elmer, LAMBDA 1050). Experimental errors quoted correspond to the deviation from the average values of three or more devices on the same substrates, or from unpatterned films deposited during the same growth.

6.3 Mixed HJ for inverted semitransparent OPV cells

Inverted semitransparent mixed HJ OPV cells were fabricated based on the donor, DBP, and the acceptor, C_{70}. The 30 nm thick DBP:C_{70} (1:8 vol. ratio) blend has an average transmission of $\bar{T} = 59 \pm 2\%$ between the wavelengths of $\lambda = 400$ nm to 700 nm, and appears red owing to its reduced long wavelength absorption (inset, Fig. 6.1(a)). The mixed HJ cells had the following structures: ITO/ZnO (30 nm)/DBP:C_{70} (1:8 vol. ratio, thickness $x = 30, 40, 50, 60, 70$ nm)/MoO$_3$(20 nm)/ITO. The *J-V* and *EQE* characteristics are shown in Figs. 6.1 (a) and (b) with device performance summarized in Table 6.1. The OPV cell with $x = 30$ nm has a short circuit current density of $J_{SC} = 4.8 \pm 0.1$ mA/cm^2, an open circuit voltage of $V_{OC} = 0.88 \pm 0.01$ V, a fill factor of $FF = 0.61 \pm 0.01$ and $PCE = 2.6 \pm 0.1\%$ with $\bar{T} = 59 \pm 2\%$ across the visible as shown in the left inset, Fig. 6.1(a). The cells with thicker photoactive layers exhibit increased *EQE*

across the entire visible owing to enhanced absorption (Fig. 6.1(b)), thus leading to a correspondingly higher J_{SC}. While V_{OC} is independent of thickness, FF decreases with increasing x due to increased series resistance. Figure 6.2 shows a correlation between PCE and $\overline{T}$ as a function of the photoactive layer thickness. The PCE and $\overline{T}$ show opposite trends, with a maximum $PCE = 3.5 \pm 0.1\%$ at $x = 60$ nm and $\overline{T} = 47 \pm 2\%$ across the visible. PCE decreases with further increases in thickness owing to reduction in FF.
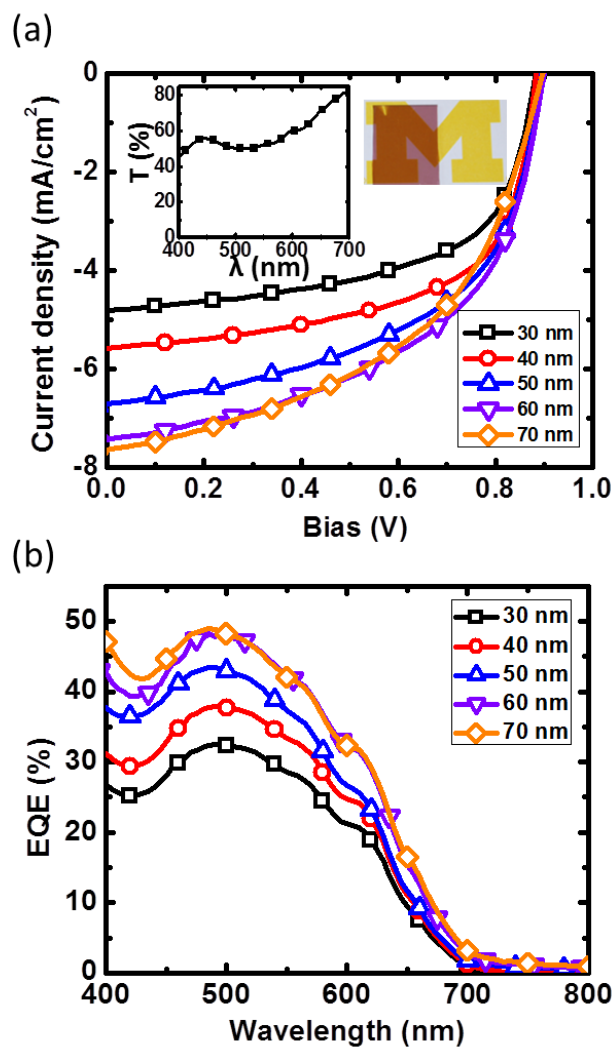
Figure 6.1 (a) Current density-voltage characteristics of semitransparent OPV cells with different active layer thicknesses, *x*. *Inset*: (left) Transmission spectrum of *x*=30 nm DBP:C_{70} mixed film; (right) Photograph of *x*=30 nm DBP:C_{70} film on a quartz substrate. (b) External quantum efficiency (*EQE*) spectra for the same devices *vs. x*.

Table 6.1 Performance of inverted, semitransparent OPV cells

Device	J_{SC} (mA/cm^2)	V_{OC} (V)	FF	PCE (%)
Mixed HJ (x=30 nm)	4.8 ± 0.1	0.88 ± 0.01	0.61 ± 0.01	2.6 ± 0.1
Mixed HJ (x=40 nm)	5.6 ± 0.1	0.88 ± 0.01	0.60 ± 0.01	3.0 ± 0.1
Mixed HJ (x=50 nm)	6.6 ± 0.2	0.89 ± 0.01	0.57 ± 0.01	3.3 ± 0.1
Mixed HJ (x=60 nm)	7.4 ± 0.2	0.89 ± 0.01	0.53 ± 0.01	3.5 ± 0.1
Mixed HJ (x=70 nm)	7.7 ± 0.2	0.89 ± 0.01	0.49 ± 0.01	3.3 ± 0.1
PM-HJ	7.5 ± 0.2	0.89 ± 0.01	0.58 ± 0.01	3.9 ± 0.2
Front	7.4 ± 0.2	0.82 ± 0.01	0.51 ± 0.01	3.1 ± 0.1
Back	7.8 ± 0.2	0.89 ± 0.01	0.54 ± 0.01	3.7 ± 0.2
Tandem(bottom illumination)	6.2 ± 0.2	1.70 ± 0.01	0.51 ± 0.01	5.3 ± 0.3
Tandem(top illumination)	5.8 ± 0.2	1.70 ± 0.01	0.50 ± 0.01	4.9 ± 0.3

To further understand the dependence of *FF* on *x*, the specific series resistance (R_SA) is obtained *vs.* active layer thickness by fitting the dark *J-V* characteristics to:[24]

$$J(V) = J_s \left[\exp\left(q \frac{[V - J \cdot R_S A]}{n k_B T} \right) - \chi \right] - J_{ph}(V), \tag{6.1}$$

where J_s is the saturation current density in the dark, *n* is the ideality factor associated with the donor (acceptor) layer, k_B is the Boltzmann constant, *T* is the temperature, *q* is the elementary charge, and J_{ph} is the photocurrent density. Also, $\chi \sim 1$ is the ratio of the polaron-pair dissociation rate at the heterojunctions between donor and acceptor at *V* to its value at $V = 0$. We find $R_S A =$

2.9 ± 0.1 $\Omega \cdot cm^2$ for 30 nm thick OPV cells, and increases to 5.8 ± 0.1 $\Omega \cdot cm^2$ for 70 nm thick devices; a result of reduced charge collection efficiency arising from the lack of continuous paths for charge extraction (and hence *FF*) of thicker donor/acceptor mixed regions.
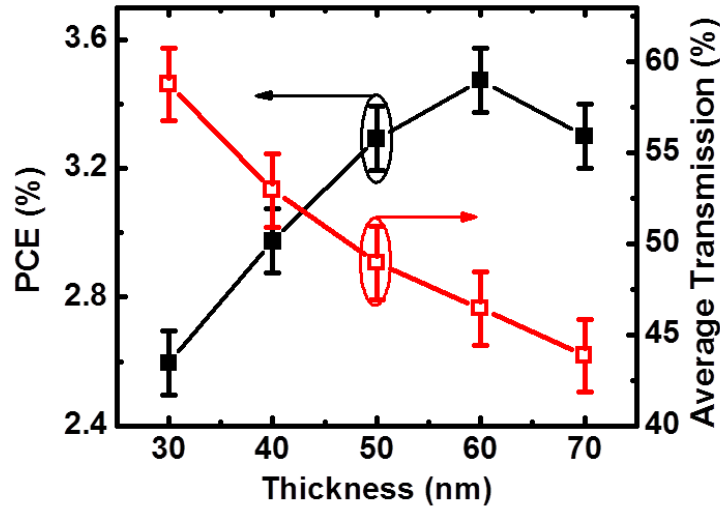
Figure 6.2 Power conversion efficiency, *PCE* (left axis) and average optical transmission between the wavelengths of $\lambda = 400$ nm to 700 nm (right axis) *vs.* thickness of the photoactive layers for mixed HJ OPV cells.

6.4 Planar-mixed HJ for inverted semitransparent OPV cells

The inverted PM-HJ architecture consisting of a donor/acceptor mixture grown onto a neat acceptor layer is useful in reducing the active region series resistance by improving charge collection.[28, 122] Thus, we replaced the $x = 60$ nm DBP:C_{70} layer in the mixed HJ with C_{70} (9 nm) /DBP:C_{70} (51 nm, 1:8 vol. ratio) for the photoactive region. The neat C_{70} layer thickness is roughly equal to its exciton diffusion length[47], leading to efficient exciton dissociation at the acceptor/blend interface. The C_{70}/DBP:C_{70} film has $\overline{T} = 51 \pm 2$ % across the visible spectrum, >10% higher than that of the mixed HJ. Figure 6.3(a) shows the *J-V* characteristics of both the

mixed HJ and PM-HJ OPVs. The PM-HJ has a $J_{SC} = 7.5 \pm 0.2$ mA/cm^2; almost the same as the mixed HJ. Both cells have the same $V_{OC} = 0.89 \pm 0.01$ V as expected, whereas *FF* increases from 0.53 ± 0.01 for the mixed HJ to 0.58 ± 0.01 for the PM-HJ due to a decrease in R_SA from 5.0 ± 0.1 $\Omega \cdot$cm^2 to 3.8 ± 0.1 $\Omega \cdot$cm^2. Therefore, *PCE* of the PM-HJ OPV cell is increased to 3.9 ± 0.2 %, an 11% increase compared to the mixed HJ.

To further understand the improved combination of transparency and efficiency of the PM-HJ architecture, we measured the internal quantum efficiency (*IQE*), i.e. the ratio of photogenerated carriers collected at the electrodes to the absorbed photons in the active region. The PM-HJ shows reduced absorption calculated using transfer matrices[2, 60], compared to the mixed HJ, particularly between the wavelength of $\lambda = 550$ nm to 700 nm (see Fig. 6.3(b)). This results from a reduced amount of DBP in the photoactive region in the former structure. With a similar *EQE* for both architectures, the *IQE* of the PM-HJ is thus greater than that of the mixed HJ.
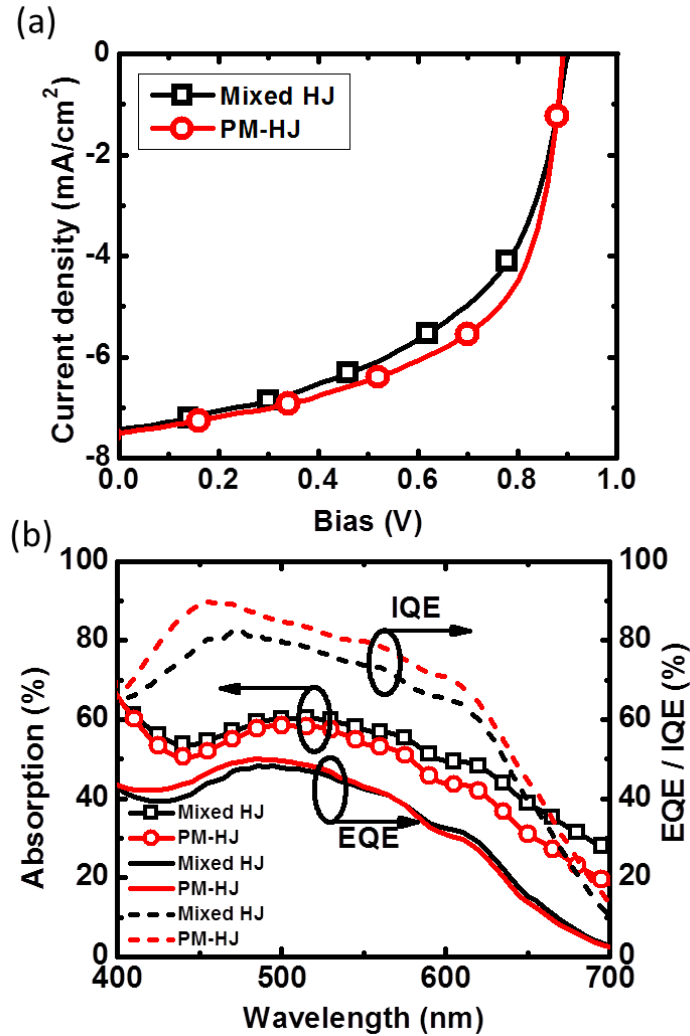
Figure 6.3 (a) Current density-voltage characteristics of inverted semitransparent mixed HJ (hollow squares) and PM-HJ (hollow circles) OPVs under simulated AM 1.5G illumination at one sun intensity. (b) Calculated absorption (left axis), *EQE* and internal quantum efficiency (*IQE*, right axis) spectra of mixed and PM-HJ cells. Optical constants used in the absorption calculation were measured by variable angle spectroscopic ellipsometry.

6.5 Inverted semitransparent tandem cells

Based on the single junction cell results, we fabricated an inverted semitransparent tandem cell incorporating two PM-HJ sub-cells that absorb in different spectral regions. The sub-cells employed 2-((7-(5-(dip-tolylamino)thiophen-2-yl)benzo[c][1,2,5]thiadiazol-4yl)methylene)

malononitrile (DTDCTB):C_{60} for absorbing in the near infrared (NIR), and DBP:C_{70} for blue-green absorption. The charge generation layer (CGL) between the sub-cells is comprised of MoO_3(5 nm)/Ag(0.1 nm)/BPhen:C_{60} (5 nm, 1:1 vol. ratio). The optimal tandem structure is ITO/ZnO (30 nm)/C_{60} (5 nm)/ 1:1 DTDCTB:C_{60} (60 nm)/CGL/C_{70} (7 nm)/ 1:8 DBP:C_{70} (55 nm)/MoO_3 (20 nm)/ITO (100 nm). We also fabricated discrete front and back cells with the structure: ITO/ZnO (30 nm)/organic photoactive layer (front cell: C_{60} (5 nm)/1:1 DTDCTB:C_{60} (60 nm); back cell: C_{70} (7 nm)/ 1:8 DBP:C_{70} (55 nm)) / MoO_3 (20 nm)/ITO (100 nm) for comparison. .

Figure 6.4(a) shows *J-V* characteristics of discrete sub-cells and the tandem cells, with their performances summarized in Table 6.1. The calculated optical absorption of the sub-cells is plotted in the inset of Fig. 6.4(a). The DTDCTB:C_{60} and DBP:C_{70} films appear green and red (see Fig. 6.4(b), inset), respectively, owing to their different absorption spectra, while the tandem film has a neutral appearance due to its broader absorption spectrum. Hence, depending on the needs of a particular application, single junction cells can be designed to have a particular tint, whereas the more absorptive and efficient tandem cell has a neutral coloration.

Figure 6.4(b) also shows the *EQE* of the discrete and tandem cells. The *EQE* of tandem cells, which is a sum of *EQE* of discrete front and back cells, is used here to characterize the photon-harvesting efficiency of tandem cells across the solar spectrum. As shown in Fig. 6.4(b), the *EQE* of the tandem cell reaches >50% at the wavelength of λ < 600 nm, and remains >30% at λ = 750 nm, indicating efficient photon harvesting across the visible and NIR spectral regions. The tandem cell V_{OC} = 1.70 ± 0.01V, almost equal to the sum of two sub-cells, indicating that the CGL is electrically lossless. Furthermore, J_{SC} = 6.2 ± 0.2 mA/cm^2 for the tandem is less than that of the individual sub-cells mainly due to the slight overlap of their individual absorption spectra.

The tandem cell has $FF = 0.51 \pm 0.01$, limited by that of the DTDCTB:C_{60} PM-HJ. Overall, the optimized tandem cell exhibits $PCE = 5.3 \pm 0.3$ % under simulated AM 1.5G illumination at one sun intensity, with $\overline{T} = 31 \pm 1$ % across the visible.

Previously, thin metal films have been employed as semitransparent cathodes in OPV cells.[108, 111, 114, 119] These films, however, reflect and absorb a significant fraction of the incident light, which dramatically reduces the efficiency of the device when illuminated via the cathode *vs.* the anode. Several strategies have been developed to overcome the shortcomings, such as solution-processed Ag nanowires[116-117]. In our devices, the use of metal-free, transparent ITO for both contacts eliminates these reflections and optical losses. Top illuminated tandem cells have $J_{SC} = 5.8 \pm 0.2$ mA/cm^2 compared to 6.2 ± 0.2 mA/cm^2 for bottom illumination, yielding $PCE = 4.9 \pm 0.3$ % *vs.* 5.3 ± 0.3 %, respectively.
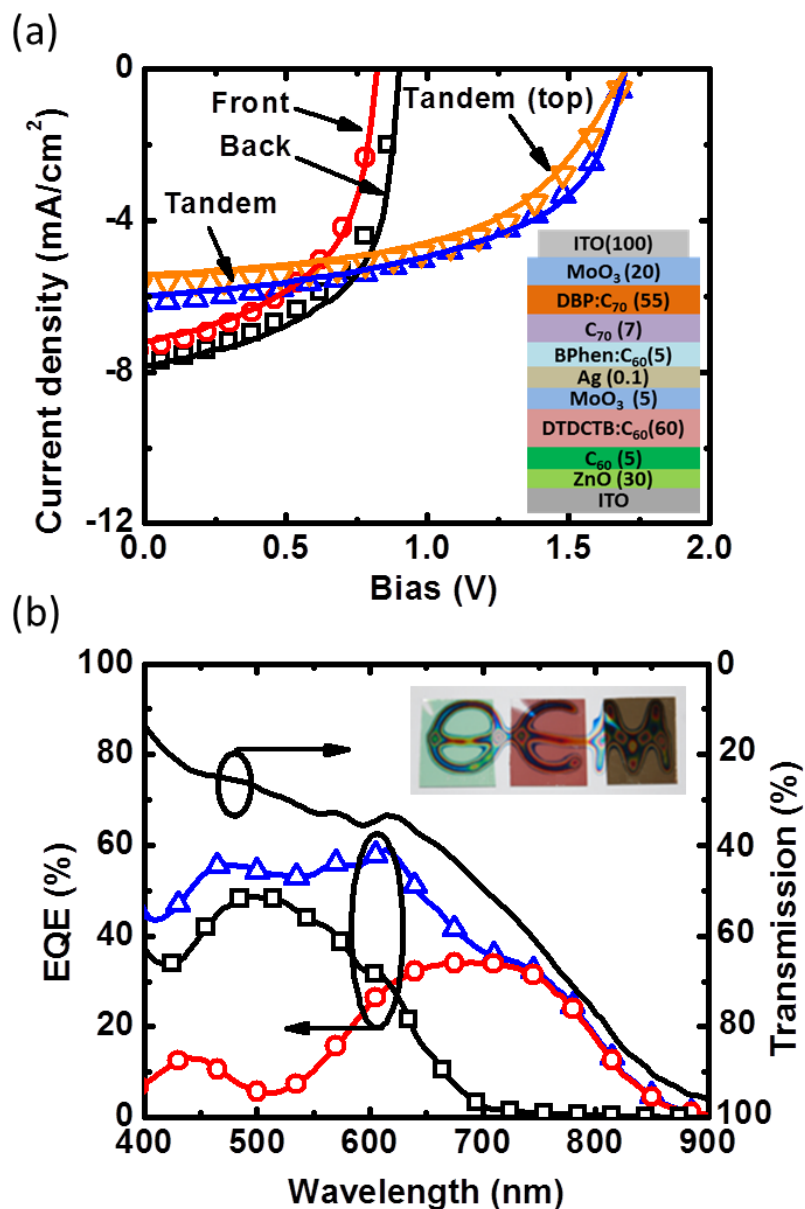
Figure 6.4 (a) Current density-voltage characteristics of inverted semitransparent single junction and tandem OPV cells. Hollow circles, squares, triangles, and inverse triangles represent experimental data of the front, back sub-cells used in the tandem, the tandem cell under bottom illumination, and the same tandem under top illumination, respectively. Lines are calculated characteristics following the previously described methods.[47, 100] *Inset*: Schematics of the tandem cell structure with the thickness of each labelled in the brackets (unit: nm). (b) The *EQE* (left axis) *vs.* wavelength for semitransparent single junction and tandem cells (circles: front cell; squares: back cell; triangles: tandem) and transmission spectrum (right axis) of the tandem cell. *Inset*: Photograph of DTDCTB:C_{60} (1:1 vol. ration, 60 nm, left), DBP:C_{70} (1:8 vol. ratio, 55 nm, middle) and tandem (1:1 DTDCTB:C_{60}(60 nm)/CGL/1:8 DBP:C_{70}(55 nm), right) films.

91

6.6 Conclusions

In conclusion, we demonstrated inverted semitransparent PM-HJ OPV cells with improved charge collection and reduced series resistance compared to an analogous mixed HJ. The optimal single junction cell achieves a $PCE = 3.9 \pm 0.2\%$ with $\overline{T} = 51 \pm 2$ % across the visible. We also demonstrated an inverted semitransparent tandem cell with $PCE = 5.3 \pm 0.3$ % and $\overline{T} = 31 \pm 1$ % across the visible spectrum. These results illustrate the unique attributes of organic semiconductors to provide tinted or neutral density solar power generating coatings with potential for integration within the built environment.

Chapter VII

Scalability of multi-junction organic solar cells for large area organic solar modules

In Chapter 5, we have shown that multi-junction OPV cells can achieve higher *PCE* than single junction cells due to reduced thermalization losses and broadened coverage of the solar spectrum[7, 9, 123]. There is, however, less attention paid to scaling the size of OPV cells, particularly those consisting of more than one active cell in a stack (i.e. multi-junction cells), which is key for their practical application[13, 124-128]. Here we report on a systematic investigation of the scalability of multi-junction OPV cells ranging from 1 mm^2 to 1 cm^2, and find the reduction in *PCE* with increased active area is due to increased ITO anode series resistance, which in turn reduces the *FF*. Further, multi-junction OPV cells show reduced losses with cell area compared to single-junction cells due to their higher V_{OC} and lower J_{SC}. Based on our findings, we fabricated OPV modules comprised of an array of 25, 1 cm^2 multi-junction cells. A yield of 100% for the discrete cells in the array is achieved across the module, with a variation of *PCE* from cell-to-cell of <10%. The OPV module generates an electrical power of 162 ± 9 mW under simulated AM1.5G illumination at one sun intensity, corresponding to *PCE* = 6.5 ± 0.1 %.

7.1 Materials and device architectures

We studied the scalability of single, tandem, triple and four junction OPV cells based on the donors, DTDCTB and DBP, combined with C_{60} and C_{70} acceptors. In multi-junction structures, a DBP:C_{70} planar-mixed heterojunction (PM-HJ) is employed as a blue-green absorbing sub-cell (sub-cell 1, SC1, in Fig. 7.1) while DTDCTB:C_{60} PM-HJ primarily absorbs in the near-infrared (SC2 in Fig. 7.1). For multilayer devices, sub-cells were interconnected with a charge generation layer (CGL) comprising bathophenanthorline (BPhen):C_{60} mixed layer (5 nm, 1:1 vol. ratio)/Ag (0.1 nm)/MoO_3 (5 nm). Four-junction cells consist of the following structure (from the cathode): Ag (100 nm)/BPhen (7 nm)/SC1/CGL/SC2/CGL/SC1/CGL/SC2/MoO_3 (10 nm)/ITO. For triple, tandem and single junction cells, the sub-cells and CGLs closest to the anode are eliminated according to the number of stages (e.g. a tandem has active regions of SC1/CGL/SC2, etc.). Each device structure is optimized through both experiments and simulations.[7]

94
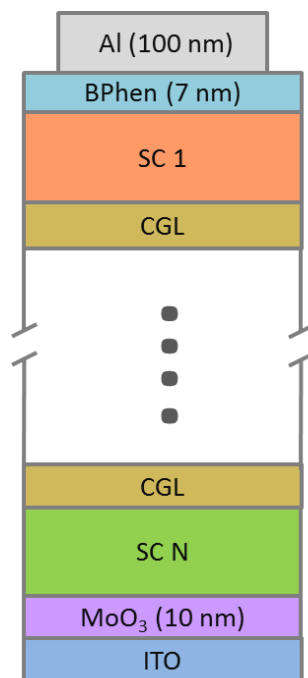
Figure 7.1 Schematic of a multi-junction organic photovoltaic (OPV) cell. Single junction cells have photoactive layers of DBP:C_{70} (54 nm, 1:8 vol. ratio)/C_{70} (9 nm). For multi-junction cells, the structures of sub-cell 1 (SC1) and sub-cell 2 (SC2) are DBP:C_{70} (30 nm, 1:8 vol. ratio)/C_{70} (7 nm) and DTDCTB:C_{60} (60 nm, 1:1 vol. ratio)/C_{60} (5 nm), respectively. Sub-cells are connected with charge generation layers (CGL) consisting of BPhen:C_{60} mixed layer (5 nm, 1:1 vol. ratio)/Ag (0.1 nm)/MoO_3 (5 nm). Four-junction cells consist of the following structure (from the cathode): Ag (100 nm)/BPhen (7 nm)/SC1/CGL/SC2/CGL/SC1/CGL/SC2/MoO_3 (10 nm)/ITO. For triple and tandem cells, the sub-cells and CGLs closest to the anode are eliminated according to the number of stages.

7.2 Experiments

The OPV cells were grown on glass substrates pre-coated with ITO with a sheet resistance of 15 Ω/sq. The substrates were sonicated in detergent and a series of organic solvents including acetone and isopropanol for 10 min each. After solvent cleaning, the substrates were then snow-cleaned[129] to remove large particles, and subsequently exposed to ultra-violet ozone for 10 min immediately prior to loading in a high vacuum chamber with a base pressure of 10^{-7} torr for the deposition of organic layers. Then, 100nm-thick Al cathodes were deposited through shadow masks. The device areas were defined as the overlap area between the ITO

anode and metal cathode. Complete devices were transferred in a high-purity N_2-filled glovebox with <0.1 ppm O_2 and H_2O without the exposure to ambient air for the *J-V* measurement in the dark and under simulated AM 1.5G illumination.

7.3 Results and discussions

Device performance as a function of area is shown in Fig. 7.2 and Table 7.1 for single, double, triple and four junction cells. The higher *PCE* of multi-junction cells compared with single junction cells results from a broadened coverage of the solar spectrum and reduced thermalization losses.[7, 9, 47] While J_{SC} and V_{OC} of each device type remains almost the same as a function of device area (Figs. 7.2 (a) and (b)), *FF* decreases as area increases (Fig. 7.2(c)). Among various devices, single junction cells exhibit the largest drop of 17.2 ± 1.7 % in *PCE* as area increases from 1 mm^2 to 1 cm^2, whereas tandem, triple and four junction cells suffer reductions of 8.5 ± 0.8 %, 6.3 ± 0.6 % and 4.1 ± 0.5%, respectively. The reduced loss in *PCE* for multi-junction cells is primarily due to increased V_{OC} and reduced J_{SC} with each additional element.
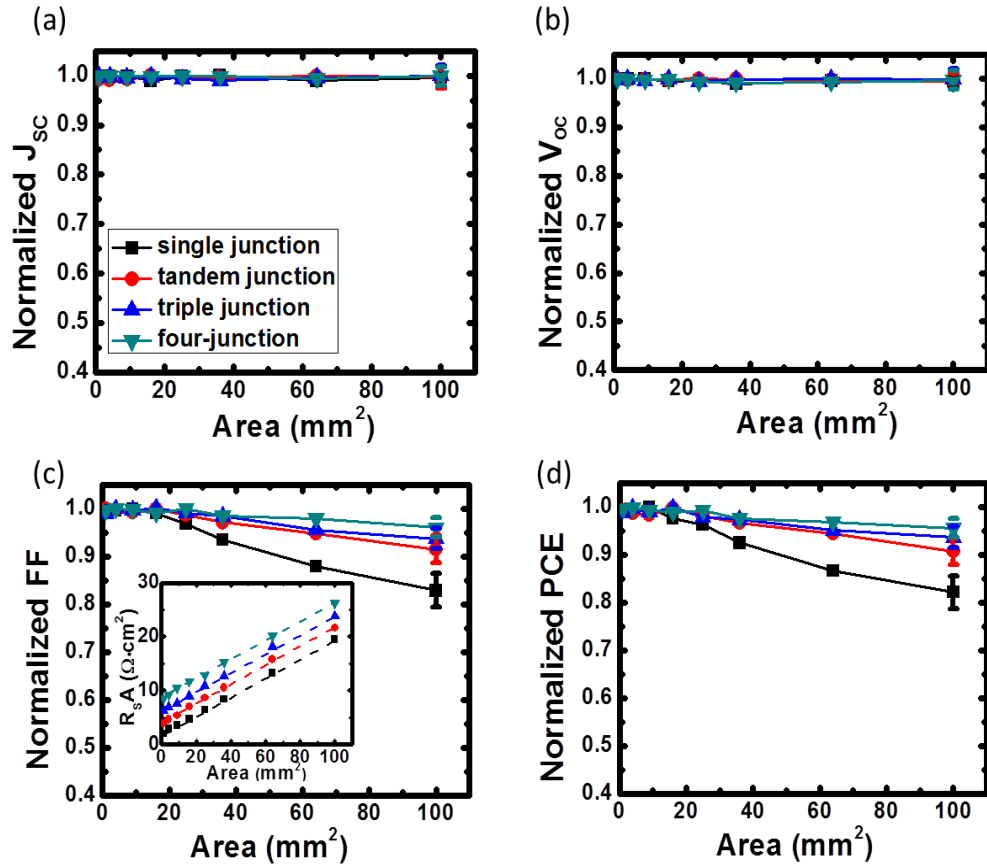
Figure 7.2 Normalized device performance (a) Short circuit current density, J_{SC}, (b) open circuit voltage, V_{OC}, (c) fill factor, FF and (d) power conversion efficiency, PCE, as functions of area for single, tandem, three and four-junction OPVs. *Inset* of (c): series resistance *vs.* device area. Actual efficiencies of each device with 1 mm^2 and 1 cm^2 area are provided in Table 7.1.

Table 7.1 Device performance of single, tandem, triple and four junction OPV cells with different device areas

Device (area)	J_{SC} (mA/cm^2)	V_{OC} (V)	FF	PCE (%)
Single (1 mm^2)	11.3 ± 0.2	0.92 ± 0.01	0.59 ± 0.01	6.1 ± 0.2
Single (1 cm^2)	11.3 ± 0.2	0.91 ± 0.01	0.49 ± 0.01	5.0 ± 0.2
Tandem (1 mm^2)	7.5 ± 0.2	1.70 ± 0.02	0.58 ± 0.01	7.4 ± 0.2
Tandem (1 cm^2)	7.5 ± 0.2	1.69 ± 0.02	0.53 ± 0.01	6.7 ± 0.2
Triple (1 mm^2)	5.3 ± 0.1	2.59 ± 0.02	0.58 ± 0.01	8.0 ± 0.2
Triple (1 cm^2)	5.3 ± 0.1	2.59 ± 0.02	0.54 ± 0.01	7.5 ± 0.2
Four (1 mm^2)	4.7 ± 0.1	3.34 ± 0.02	0.57 ± 0.01	8.9 ± 0.2
Four (1 cm^2)	4.6 ± 0.1	3.33 ± 0.02	0.54 ± 0.01	8.3 ± 0.2

To understand the effect of scaling on device performance, the specific series resistance (R_SA) of the OPV cells was analyzed as a function of device area (A). Thus, we can write:[124]

$$R_SA = R_{sheet}\left(\frac{L}{W}\right)A + \sum_N(\rho_{org}t_{org} + r_{int}), \tag{7.1}$$

where the sum is over each element in the stacked device consisting of N =1, 2, 3, or 4 sub-elements, R_{sheet} is the sheet resistance of ITO, L and W are the length and width of the ITO contact, ρ_{org} is the resistivity of the organic layer, t_{org} is the thickness of organic layer and r_{int} is the specific interface resistance. The term of $R_{sheet}(L/W)A$ corresponds to the contribution from ITO which results from the charge transport across the anode, while $\sum_N(\rho_{org}t_{org} + r_{int})$

corresponds to the contribution of resistance from the organic layers and interfaces. This can be approximated as:

$$R_S A = R_{sheet} \left(\frac{L}{W}\right) A + N \cdot r_{jn},$$

(7.2)

where r_{jn} is the specific resistance of organic layers and interfaces for a single junction. We obtain $R_S A$ from a fit to the ideal dark current density-voltage (J-V) characteristics described using:[24]

$$J(V) \approx J_s \left[\exp\left(q\frac{[V-J\cdot R_S A]}{nk_B T}\right) - \chi\right] - J_{ph}(V),$$

(7.3)

where J_s is the saturation current density in the dark, n is the ideality factor associated with the donor (acceptor) layer, k_B is the Boltzmann constant, T is the temperature, q is the elementary charge, and J_{ph} is the photocurrent density. Also, $\chi \sim 1$ is the ratio of the polaron-pair dissociation rate at the heterojunctions between donor and acceptor at V to its value at equilibrium ($V = 0$). As shown in the inset of Fig. 7.2(c), $R_S A$ increases linearly with device area, as expected. From Eq. (7.2), fit to the data gives the average junction resistance $\overline{r_{jn}} = 2.1 \pm 0.2$ $\Omega \cdot cm^2$. For the 1 mm^2 single junction cell, $R_{sheet} A = 0.015 \pm 0.002$ $\Omega \cdot cm^2$, which is small compared with $r_{jn} = 1.90 \pm 0.08$ $\Omega \cdot cm^2$. However, for 1 cm^2 single junction cell, $R_{sheet} A$ increases to 18 ± 1 $\Omega \cdot cm^2$ which is now dominant. Multi-junction cells show a similar trend as the single-junction cell. However, since the organic contribution is higher for multi-junction OPV cells due to more organic layers and interfaces, scaling of resistance with area is not as pronounced as for single junction OPVs, and hence the ITO sheet resistance plays a relatively small role in multi-junction cells compared to contributions from R_{jn}, while for large area cells, ITO resistance dominates leading to a significant drop in *FF* and, therefore, *PCE*.

To further understand the area dependence of *FF*, we write:[130]

$$\frac{FF(R_S A)}{FF(0)} = 1 - \left(\frac{J_{SC} R_S A}{V_{OC}}\right), \qquad (7.4)$$

where *FF*(0) is the fill factor at $R_S A = 0$. The normalized *FF* in Eq. (7.4) as a function of J_{SC} and V_{OC} is shown in Fig. 7.3. For comparison, we fix $R_S A$ at the value for single junction cells to focus on the influence of J_{SC} and V_{OC} on *FF*. Note, $R_S A$ is dominated by the ITO series resistance for 1 cm^2 devices, independent of *N*. Therefore, the single junction cell has the largest loss in *FF* due to its higher J_{SC} and lower V_{OC}. The tandem cell has almost double the V_{OC} and half J_{SC} compared to single junction cells, leading to a significantly reduced loss in *FF*. Similarly, triple and four junction cells exhibit proportionately higher V_{OC} and lower J_{SC} and an even smaller *FF* loss, which is less than 5% for *N*=4. The experimental results (Fig. 7.2(c)) are in agreement with calculations (stars in Fig. 7.3). Multi-junction cells with further increase in the device area (>1 cm^2) should follow the same trend.
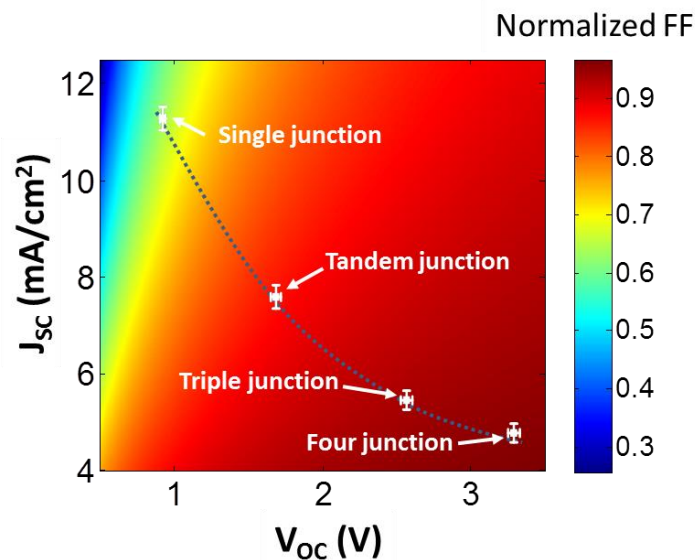
Figure 7.3 Calculated normalized *FF* as a function of J_{SC} and V_{OC}. The stars represent the measured coordinates of OPV cells with different stacking arrangements that are in agreement with calculations. The dashed line serves as a guide to the eye.

To reduce the dominant contribution to R_SA from ITO, we employ a sub-electrode structure[131] with our tandem cells. The sub-electrodes consist of a metal bus bar around 95% of the device perimeter, thereby reducing R_SA to 7.2 ± 0.3 Ohm·cm^2 compared to 21.6 ± 1.3 Ohm·cm^2 for a 1 cm^2 cell without sub-electrodes. The reduced series resistance improves *FF* from 53 ± 1% to 58 ± 1%, thus leading to an increase in *PCE* from 6.7 ± 0.2 % to 7.3 ± 0.2 %, which is almost the same as the efficiency of small-area cells with an identical device structure.

7.4 Organic solar modules

With this understanding of scalability, we fabricated a module comprised of 25, 1 cm^2 discrete tandem cells as shown in Fig. 7.4. For each discrete cell, the sub-electrode is employed to reduce the series resistance from the anode. Five discrete cells are connected in series to form

a column, while five columns are connected in parallel to form a module in Fig. 7.4(b). A photograph of a complete module is shown in the inset of Fig. 7.5(b).
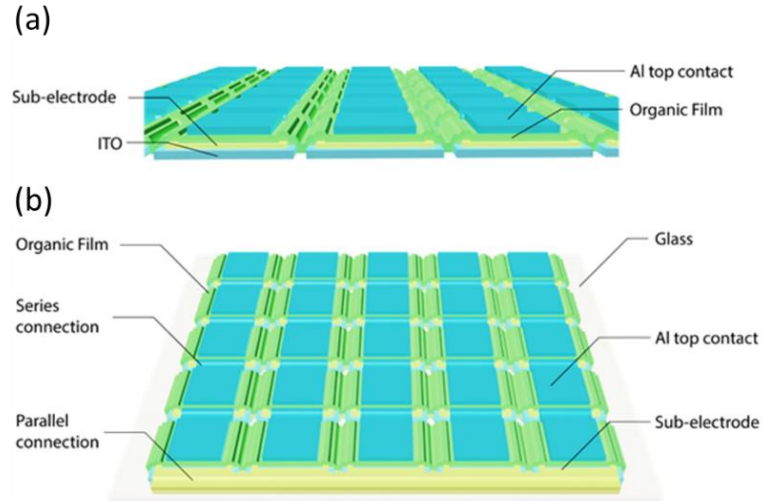
Figure 7.4 Views of the OPV module design: (a) Front and (b) top view of the module.

OPV modules were fabricated on glass substrates. First, ITO was sputtered through a shadow mask in a high vacuum chamber with a base pressure of 1×10^{-7} torr. Then the ITO/glass substrates were cleaned as above. Organic layers and metal contacts (including the sub-electrode structures) were deposited through shadow masks, also in high vacuum.

The discrete cell yield is 100%, mainly owing to the snow-cleaning process that efficiently removes particles on the substrate surface, and therefore reduces the risk of shorting. The *PCE* of discrete cells under simulated AM1.5G, 1 sun illumination range from 6.7% to 7.2%, with a variation less than 10% across the module as shown in Fig. 7.5(a).
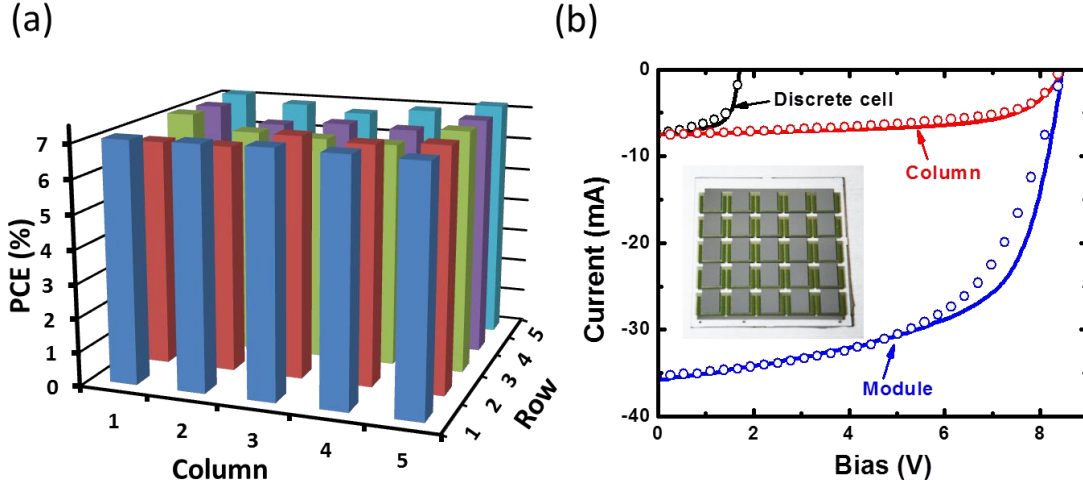
Figure 7.5 (a) *PCE* distribution of discrete OPV cells across the module; (b) experimental (circles) and calculated (solid lines) current-voltage (*I-V*) characteristics of a discrete cell (black), a column of 5 cells connected in series (red), and the entire whole module (blue) under 1 sun illumination. *Inset*: Photo of a complete OPV module.

From Eq. (7.3) we can write the current-voltage (*I-V*) characteristics in terms of the number of series and parallel cells (*S* and *P*, respectively): $I(V) = S\left\{ I_s \left[exp\left(\frac{q(\frac{V}{P} - \frac{R_S AI}{S})}{nk_BT} \right) - 1 \right] - I_{ph} \right\}$. We fit experimental *I-V* curves of a discrete cell, a column of 5 cells and the entire module

using Eq. (7.4), as shown by the lines in Fig. 7.5(b). For a column of five discrete cells connected in series, the $V_{OC} = 8.45$ V which is within 0.5% of the sum of V_{OC} for 5 individual cells, while the short-circuit current of a column is 7.5 mA, the same as the discrete cell current, as shown in Fig. 7.5(b). This indicates that resistive losses are minimal in the module compared to that of the individual cells due to a combination of the use of tandem cells, sub-electrode design and circuit layout. The difference between the experimental and fitted *I-V* for the module (see Fig. 7.5(b)) results from the discrepancy of device performance for discrete cells likely due to the variation of film thicknesses across the module. Under simulated AM1.5G illumination at one sun

103

intensity, we obtain a module output power of 162 ± 9 mW with $I_{SC} = 36 \pm 1$ mA, $V_{OC} = 8.45 \pm$ 0.01 V and $FF = 53 \pm 1$ %, corresponding to $PCE = 6.5 \pm 0.1\%$, as shown in Fig. 7.5(b).
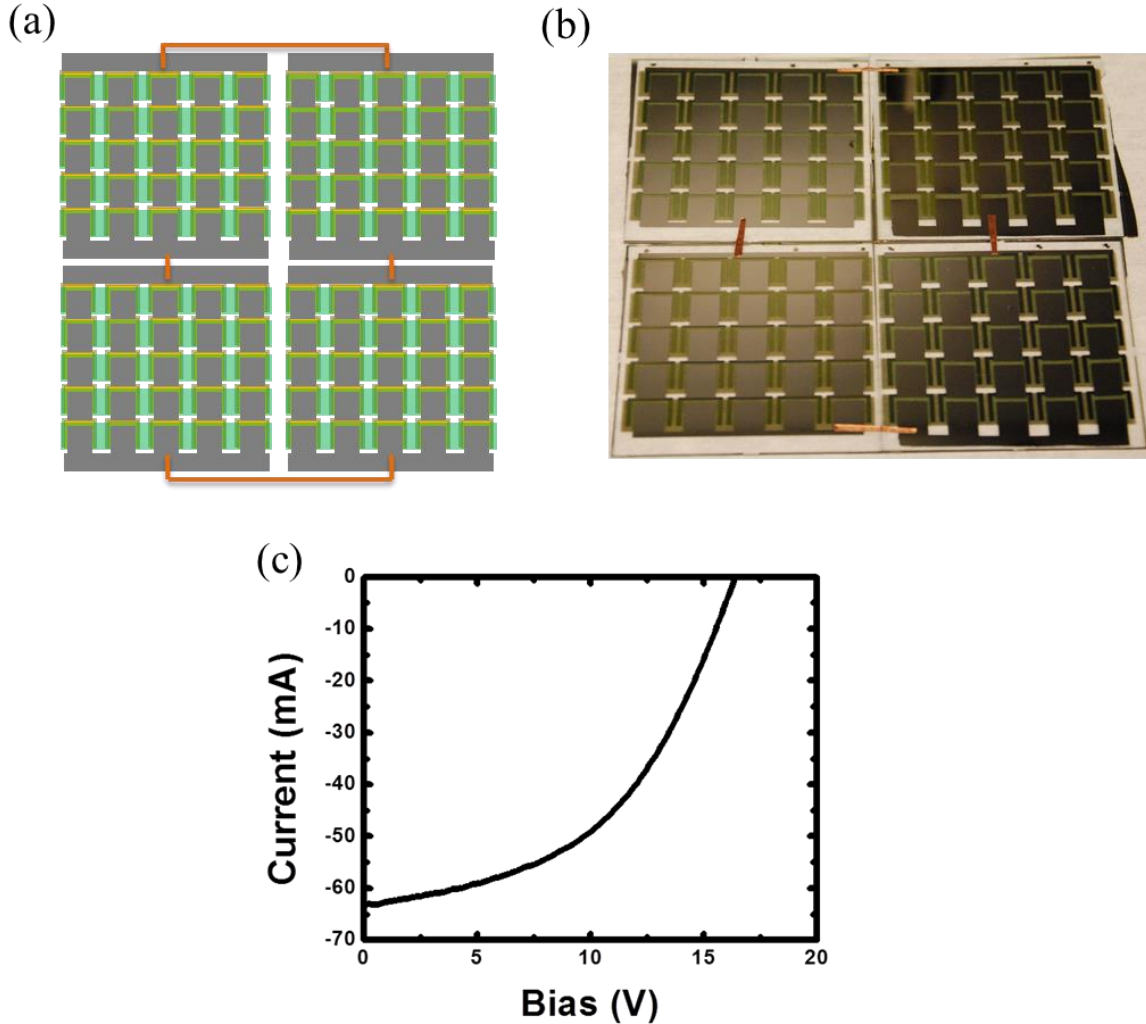
Figure 7.6 (a) Schematics of tied 2×2 organic solar modules in a series-parallel circuit configuration. (b) Photograph of tied 2×2 organic solar modules. (c) *I-V* characteristics of tied 2×2 organic solar modules under simulated AM 1.5G illumination at one sun intensity.

To further scale up, four organic solar modules are connected in a series-parallel circuit configuration for a tied 2×2 organic solar module array as shown in Fig. 7.6 (a) and (b). The module array achieves a yield of 100% for discrete cells and exhibits $I_{SC} = 63 \pm 2$ mA, $V_{OC} =$ 16.4 $\pm$ 0.03 V, $FF = 50 \pm 1\%$, corresponding to a $PCE = 5.2 \pm 0.1\%$ under simulated AM 1.5G

illumination at one sun intensity as shown in Fig. 7.6 (c). The V_{OC} of the tied 2×2 organic solar module array is close to the sum of ten discrete cells indicating minimal interconnection loss between discrete modules, whereas *FF* slightly decreases compared to individual modules likely due to the discrepancy of module performance. Nevertheless, the tied 2×2 organic solar module array achieves a high yield of discrete cells and delivers an appreciable output power of 519 ± 12 mW under simulated AM 1.5G illumination at one sun intensity.

7.5 Conclusions

In summary, we have studied the area-scaling effects of multi-junction OPV cells. Compared to single junction cells, multi-junction cells show a significant reduction in the loss of *PCE* for large compared to small area cells due to higher V_{OC} and lower J_{SC} of the former. This suggests that multi-junction OPV cells can achieve higher efficiency as well as improved scalability when used in practical device applications. Further, in contrast to multi-junction solar cells fabricated using inorganic semiconductors that are made small to reduce cost, multi-junction OPVs actually benefit from scaling to larger sizes. By using sub-electrodes to further reduce the series resistance from the ITO anode, we demonstrated a 25 cm^2 active area organic tandem OPV module with a discrete cell yield of 100% and an efficiency variation of <10% across the module area. We further scale up for a tied 2×2 organic solar module array with a 100% yield of discrete cells and an output power of 519 ± 12 mW under simulated AM 1.5G illumination at one sun intensity.

Chapter VIII

Conclusions and outlook for future work

8.1 Conclusions

In this thesis, we focused on the development and understanding of small molecule OPV cells with donor-acceptor mixed active regions and buffers. The first part of this thesis focused on the study of primary loss mechanisms in the donor/acceptor mixed HJ cell. Three loss mechanisms are analyzed in detail with solutions provided. Chapter 2 studied the exciton quenching at the MoO_3/organic interface. We employed a PM-HJ consisting of a donor/acceptor mixture with a neat acceptor layer on the top as the photoactive region to reduce exciton quenching at the MoO_3/organic interface, leading to a considerable improvement in *EQE* and *PCE*. Chapter 3 further investigated bimolecular recombination and exciton-polaron quenching within the PM-HJ. To suppress these two losses, we employed an exciton blocking/electron conducting buffer layer consisting of a mixture of a wide energy gap molecule, BPhen, and C_{60} in the PM-HJ, resulting in a significant increase in *FF* and *PCE*.

In the second part of this thesis, we employed DBP:C_{70} PM-HJ and mixed buffers as building blocks for tandem/multi-junction, as well as semitransparent OPV cells. Chapter 4 presents a solution-processed blended *f*SQ/C_{60} bilayer cell with higher V_{OC} and J_{SC} than single donor cells which are used as a NIR-absorbing sub-cell in the tandem. In Chapter 5, we

developed a tandem cell incorporating a blended fSQ/C$_{70}$ bilayer cell as a NIR-absorbing sub-cell paired with DBP:C$_{70}$ PM-HJ. To further enhance the absorption in the NIR, we replaced the blended fSQ/C$_{70}$ bilayer HJ with a vacuum-deposited DTDCTB:C$_{60}$ PM-HJ, leading to an increase in J_{SC} and PCE. Furthermore, we developed triple and four-junction structures to efficiently harvest photons at the second order optical interference maximum. The optimized triple and four-junction cells achieve $PCE = 11.1 \pm 0.2\%$ and $12.6 \pm 0.2\%$, respectively. Chapter 6 studies inverted semitransparent OPV cells based on both mixed HJ and PM-HJ. We employed an inverted PM-HJ structure to improve charge collection and reduce series resistance leading to a $PCE = 3.9 \pm 0.2\%$ with an average optical transmission of $\overline{T} = 51 \pm 2\%$ across the visible. Moreover, we demonstrate an inverted semitransparent tandem cell with a $PCE = 5.3 \pm 0.3\%$ and $\overline{T} = 31 \pm 1\%$ across the visible.

Finally, we studied the scalability of single and multi-junction OPV cells. The multi-junction cells exhibit reduced loss in PCE compared to single junctions due to their lower J_{SC} and higher V_{OC} during operation. We further fabricated organic solar modules with sub-electrodes incorporating 25, 1 cm^2 discrete cells in a parallel- series circuit configuration. The module has a yield of 100% with a variation of PCE from cell-to-cell of <10%.

8.2 Outlook for future work

8.2.1 Understanding charge transport in mixed HJ cells with diluted donor concentrations

In Chapter 2, we show that the best blend ratio of DBP:C$_{70}$ in a single junction is 1:8, i.e., the donor concentration in the photoactive region is only ~11%. It is striking that such a low donor concentration results in low series resistance and high FF in combination with the mixed

buffer (Chapter 3), indicating that charge collection is efficient in the mixed photoactive region with a low donor concentration. There is, however, still a mystery about the mechanism of charge transport in an OPV cell with such a low donor concentration.

Morphological studies of mixed films, particularly the phase separation between donor and acceptor domains, is the key to understanding charge transport inside the mixed region with diluted donors. Recently, selected area electron diffraction (SAED) measurements were performed on the DBP:C_{70} mixture at different ratios (see Fig. 8.1). The neat C_{70} film exhibits clear rings in the SAED pattern corresponding to (420), (311), (220) and (111) diffraction orders as shown in Fig. 8.1 (a), indicating a polycrystalline film for a neat C_{70} film. On the other hand, the 1:8 DBP:C_{70} mixture shows weak rings compared to the neat C_{70} film suggesting the crystallinity of the 1:8 mixture is decreasing, whereas the 1:1 DBP:C_{70} mixture is almost featureless in the SAED pattern indicating an amorphous nature of the film. These preliminary results suggest that it is likely that nano-scaled donor/acceptor domains are formed in the 1:8 mixture to facilitate the charge transport, but the domain size of the 1:8 mixture is considerably smaller than the neat C_{70} film. More sensitive techniques, e.g. grazing-incidence small-angle X-ray scattering (GISAXS), are needed to further investigate the phase separation of donor and acceptor domains in detail.
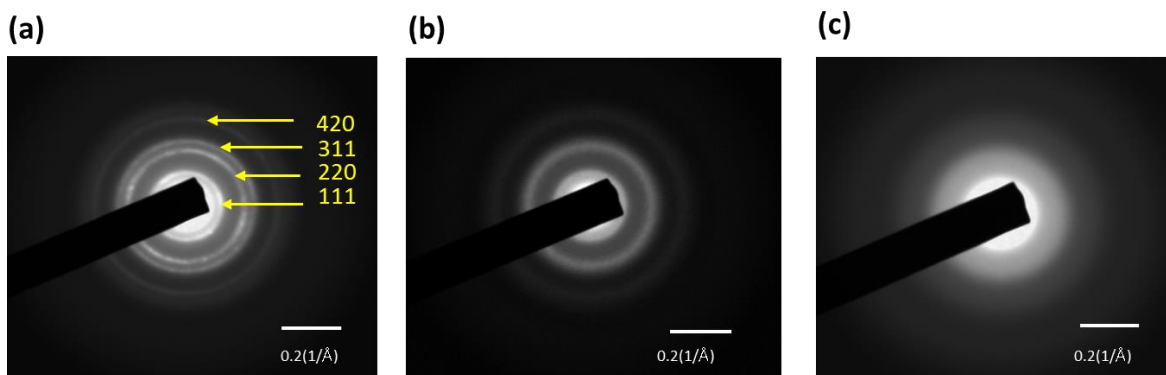
Figure 8.1 Selected area electron diffraction (SAED) patterns of (a) neat C_{70} ((420), (311), (220) and (111) diffraction orders are marked); (b) DBP:C_{70} at a 1:8 ratio; (c) DBP:C_{70} at a 1:1 ratio. Courtesy of Xiao Liu.

It is worth noting that other donor molecules, e.g. tris[4-(5-phenylthiophen-2-yl)phenyl]-amine (TPTPA) [132], 1,1-bis[4-bis(4-methylphenyl)-aminophenyl] cyclohexane (TAPC) [64] (see Figs. 8.2 (a) and (b)) and so on, can also form efficient mixed HJs with diluted donor concentrations. On the other hand, some donor molecules, e.g. DTDCTB [36], DTDCPB [133] (see Figs. 8.2 (c) and (d)), exhibit the best device performance at a 1:1 ratio. The question is why different donor molecules have different blend ratios with fullerenes for the optimized device performance. A complete understanding of the ratio dependence for different donor molecules may lead to a fundamental understanding of mixed HJ OPV cells.
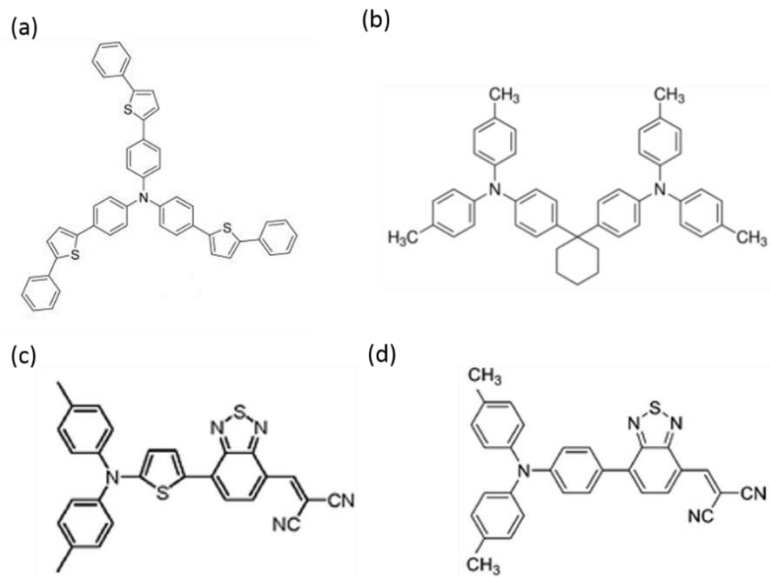
Figure 8.2 Molecular formulae of (a) TPTPA, (b) TAPC, (c) DTDCTB and (d) DTDCPB.

8.2.2 Photonic structures for light trapping in OPV cells

The relatively thin photoactive layers (~100 nm) in the mixed HJ cells usually suffer from insufficient light absorption ultimately limiting J_{SC} and, therefore, PCE, whereas the thicker photoactive region can result in reduced charge collection efficiency and a significant increase in the series resistance. Thus, it is of paramount importance to enhance the light absorption in the thin photoactive layers. One promising strategy is to implement photonic structures for light trapping in OPV cells.

Yakimov and Rand *et al.* [134-135] first demonstrated that the utilization of Ag nanoparticles (NPs) in tandem/multi-junction OPV cells can significantly enhance the long-range absorption and, thereby, increase the J_{SC} and PCE. Recently, other metal NPs have also been used in OPV cells, mainly in polymer cells, to enhance light trapping in the photoactive region.

These metal NPs are either mixed in the photoactive layers [136] or embedded in the buffer layers [137-138]. The enhancement is primarily attributed to prolonged optical paths of the incident light due to the light scattering and plasmonic local-field enhancement. For example, Jung *et al.*[137] recently demonstrated Ag NP embedded beneath the MoO_3 layer and showed that the incorporation of Ag NP can significantly increase J_{SC} in a PCDTBT:PC$_{70}$BM cell due to the enhanced light scattering and plasmonic local-field enhancement (see Fig. 8.3). On the other hand, Li *et al.* [136] blend the photoactive layer, a mixture of PBDTTT-C-T:PC$_{70}$BM, with Au NPs to enhance the light absorption as well as the conductivity, leading to an improvement in both J_{SC} and *FF*.
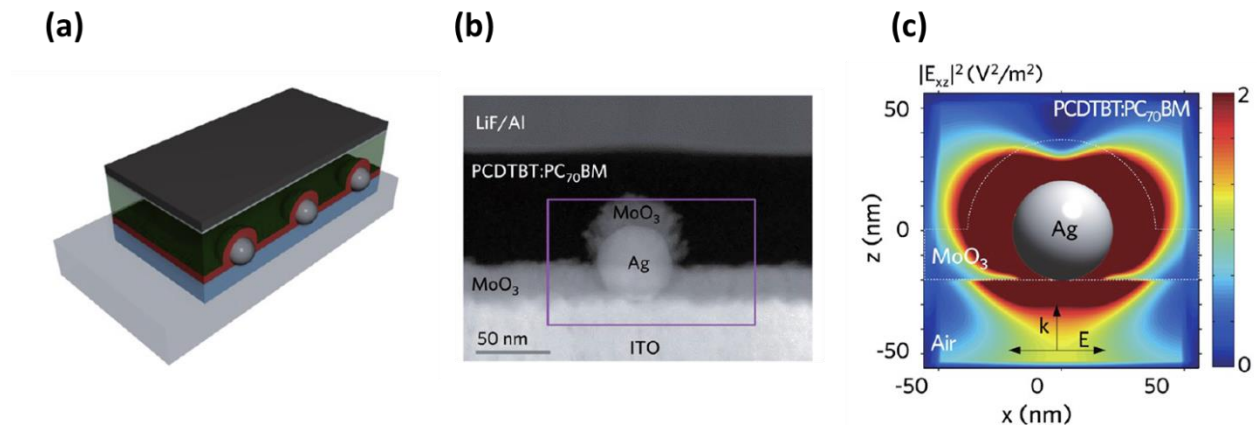
Figure 8.3 (a) Schematic cross section of a polymer OPV cell incorporating Ag NPs beneath the MoO_3 layer. (b) Cross-section high resolution TEM image of the device. (c) Calculated electric field distribution for Ag NP in the xz-plane at the wavelength of $\lambda = 533$ nm. [137]

Except for metal NPs, other photonic structures, e.g. nano-scaled antennas [139], back contact reflectors and others, can also be useful for light trapping. For instance, Niesen *et al.* [140] demonstrated a plasmonic nanostructured rear electrode to enhance the light absorption in the photoactive region (see Fig. 8.4) resulting in an increased J_{SC} and, therefore, *PCE*.
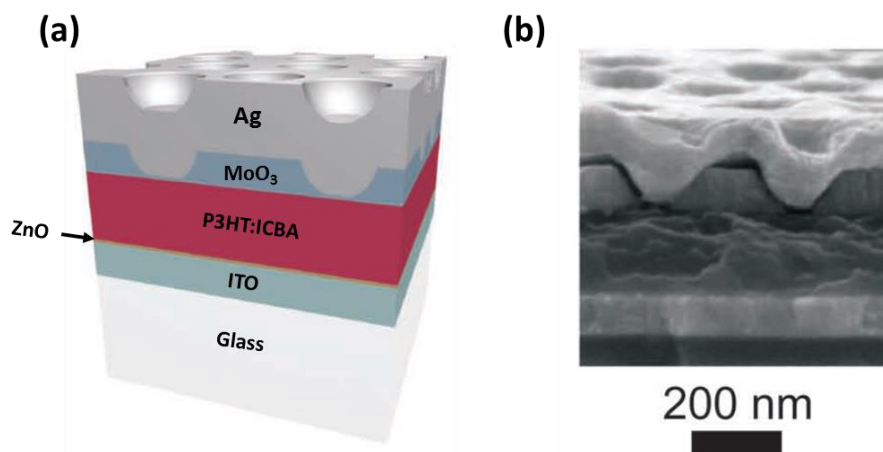
Figure 8.4 (a) Schematic diagram of an OPV cell incorporating a nanostructured Ag rear electrode; (b) Cross-section SEM image of a complete device. [140]

In spite of considerable effort to use photonic structures for the light absorption enhancement in polymer OPV cells, there are few reports on implementation of these structures for light trapping in small molecule OPV cells, particularly for tandem/multi-junction structures. Given the fact that the photoactive layers in small molecule cells are usually thinner than polymer cells, photonic structures for light trapping should be more effective in small molecule cells. Meanwhile, the implementation of these photonic structure can potentially be used to manipulate the optical field distribution inside the tandem/multi-junction OPV cells such that the optical field inside each sub-cell can be tuned to balance the photocurrent generated in each sub-cell and, therefore, further improve the device performance.

8.2.3 Advanced anode buffers for OPV cells

As we discussed in previous chapters, buffers play a critical role in determining the device performance. In Chapter 3, we demonstrated a cathode buffer comprised of wide energy

gap molecules and C_{60} that can efficiently block excitons and conduct electrons. On the other hand, the anode buffer, MoO_3, quenches excitons as discussed in Chapter 2. Although we employ a PM-HJ to reduce exciton quenching at the MoO_3/organic interface, there still remains considerable exciton quenching on the anode side. Thus, it is important to employ an exciton blocking/hole conducting anode buffer to eliminate the exciton quenching on the anode side.

Previously, Zimmerman *et al.* [141] developed a benzylphophonic acid-treat NiO buffer with an exciton blocking efficiency of 70% and similar hole extraction efficiency as MoO_3 for DPSQ/C_{60} bilayer HJ cells. Due to the enhanced exciton blocking at the anode, *EQE* increases by ~25% in the NIR spectral region leading to an increase in *PCE* from $4.8 \pm 0.2\%$ to $5.4 \pm 0.2\%$. It is possible that the same anode buffer can be employed with the mixed and PM-HJ to reduce exciton quenching.

Another promising anode buffer is a mixture comprised of wide energy gap molecules, e.g. BPhen, and a donor molecule with high hole mobility. Similar to the BPhen:C_{60} mixture, this anode buffer can block excitons due to the presence of wide energy gap molecules and also efficiently conduct holes. It is expected that the exciton blocking/hole conducting anode buffer can reduce the loss inside the device and, therefore, further improve the device performance.

To sum up, tremendous progress has been made in the field of small molecule OPV cells over the past few years. With a deeper understanding of physics underlying OPV cells along with further exploration of new materials and device architectures, we can expect a bright future for small molecule OPV cells for renewable energy sources of the next generation.

Appendix A

Measurement of multi-junction OPV cells

With multi-junction OPV cells emerging as promising structures to achieve high efficiencies, how to accurately measure the device performance of these devices becomes an essential issue. The main challenge results from considerably large spectral overlaps between sub-cells in the multi-junction OPV cells. Significant effort has been devoted on the development of accurate measurement methods for multi-junction OPV cells. There is, however, still lack of appropriate methods for the measurements of multi-junction OPV cells. In this appendix, we will introduce a method to accurately measure the device performance of multi-junction OPV cells. We will start with an introduction on the measurement principle of single-junction solar cells followed by a discussion on the measurement method for multi-junction inorganic solar cells. Then we will focus on the principle and process of our method to measurement the multi-junction OPV cells. Finally, we will compare our measurement results with the results measured by NREL for the same multi-junction OPV cells. The good agreement of results measured at two labs confirms the feasibility of our method for the accurate measurement of multi-junction OPV cells.

A.1 Measurement principle of single-junction solar cells

The power conversion efficiency (η_p) of a solar cell is defined by the equation

$$\eta_p = \frac{J_{SC} \cdot V_{OC} \cdot FF}{P_{in}} \qquad (A.\,1)$$

where P_{in} is the incident optical power per unit area. The most critical parameters for the accurate efficiency measurement are the light intensity and spectrum of the solar simulator.

Typically, a calibrated Si reference cell is used to calibrate the light intensity of the solar simulator so that the short-circuit current from the Si reference cell equals to its calibrated value under AM 1.5G illumination at one sun intensity. Since there is difference between the spectrum of the solar simulator and AM 1.5G along with the different spectral responses between the reference cell and tested cell, the mismatch factor (M) is employed to spectrally correct the measurement which is defined by the equation [142]

$$M = \frac{\int \Phi_{ref}(\lambda) Q_{ref}(\lambda) d\lambda}{\int \Phi_{sim}(\lambda) Q_{ref}(\lambda) d\lambda} \times \frac{\int \Phi_{sim}(\lambda) Q_{tst}(\lambda) d\lambda}{\int \Phi_{ref}(\lambda) Q_{tst}(\lambda) d\lambda} \qquad (A.\,2)$$

where Φ_{ref} and Φ_{sim} are spectral irradiances of AM 1.5G and solar simulator, respectively, and Q_{ref} and Q_{tst} are spectral responses of the calibrated Si reference cell and tested solar cell, respectively. The J_{SC} and η_p are spectrally corrected using the mismatch factor M. Note that the spectrally corrected J_{SC} should match with the value of J_{SC} by integrating *EQE* over the AM 1.5G to ensure the measurements of single-junction solar cells under the illumination at one sun intensity are accurate.

A. 2 Measurement principle of multi-junction solar cells

A. 2.1 Measurement principle of multi-junction inorganic solar cells

The measurement of multi-junction solar cells is more complicated than single junction cells since each sub-cell in the multi-junction structure has its own spectral response and a different mismatch factor. Simple adjustment on the total irradiance of the solar simulator cannot satisfy different requirements of spectrum change for each sub-cell. A conventional single source solar simulator can easily lead to inaccurate measurements of multi-junction solar cells. Here is an example of the measurement for a multi-junction inorganic solar cell. Figure A. 1(a) shows the *EQE* spectrum of a triple-junction AlGaAs/GaAs/InGaAs solar cell.[143] Sub-cells in this triple-junction structure can generate very different photocurrents depending on the spectra of illumination sources. For the triple-junction cell shown in Fig. A. 1(a), each sub-cell generates a J_{SC} of 16 mA/cm^2 when the photoresponse of each sub-cell is integrated with AM0 spectrum (see Fig. A. 1(b)). Using the spectrum of a solar simulator as shown in Fig. A. 1(b), the GaAs sub-cell still generates a J_{SC} of 16 mA/cm^2, whereas the AlGaAs and InGaAs sub-cells generate J_{SC} of 12.2 mA/cm^2 and 13.0 mA/cm^2, respectively, significantly lower than the values integrated with AM0 spectrum. In this case, it is likely that the measurement of the triple-junction cell under the illumination of this solar simulator is inaccurate.
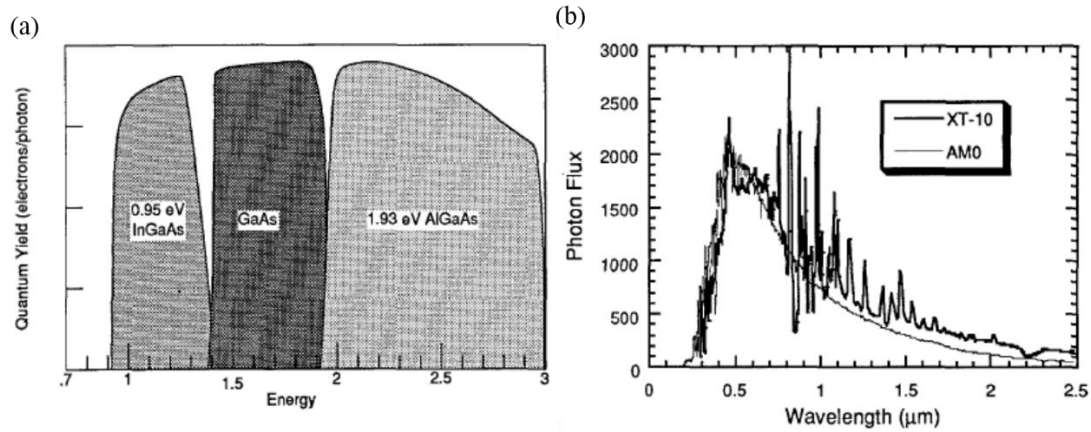
Figure A.1 (a) Quantum yield (equivalent to *EQE*) of a triple-junction AlGaAs/GaAs/InGaAs solar cell; (b) Spectra of AM0 and a solar simulator based on a Xenon lamp (XT-10). [143]

To ensure the accurate measurement of multi-junction inorganic solar cells, the spectrum of the solar simulator needs to be tuned such that each sub-cell can generate the same amount of photocurrent as it is under the illumination of the standard solar spectrum. Thus, a new type of solar simulator, multi-source solar simulator, has been developed to meet the requirement of spectral tuning for the mutli-junction solar cells. Different from conventional solar simulators consisting of only one single light source, a multi-source solar simulator is comprised on multiple independent light sources, multiple filters and fibers. Recently, NREL has built a spectrally adjustable one-sun multi-source solar simulator as shown in Fig. A. 2.[144] The multi-source solar simulator has the capability to adjust the light intensity in nine non-overlapping spectral ranges across the solar spectrum with a uniform illumination area of 9 cm^2. With the newly built multi-source solar simulator, NREL has successfully measured the multi-junction inorganic solar cells.[144]
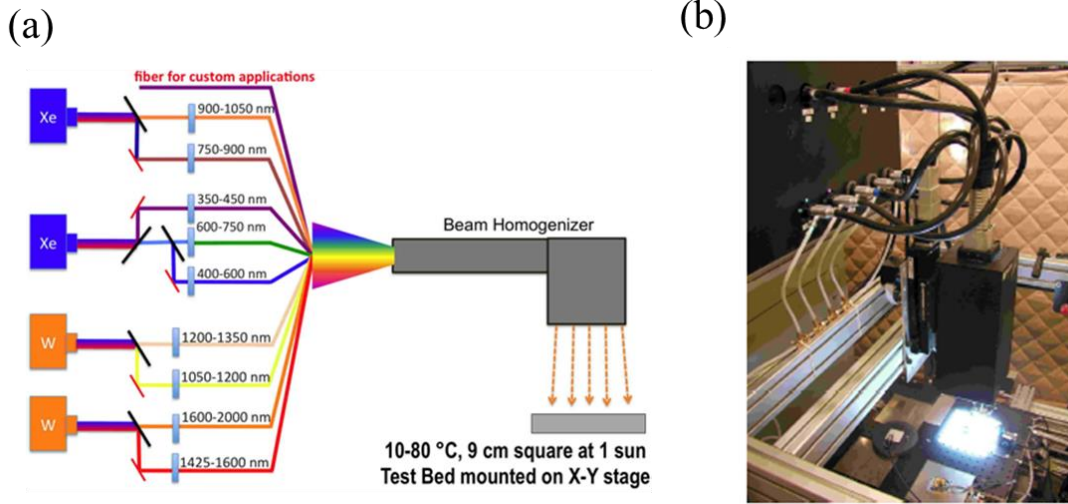
Figure A. 2 (a) Schematics of the one-sun multi-source solar simulator built by NREL; (b) Photograph of the one-sun multi-source solar simulator.[144]

A. 2.2 Measurement principle of multi-junction OPV cells

The measurement of multi-junction OPV cells is more challenging than multi-junction inorganic solar cells due to considerably large spectral overlaps between sub-cells in the multi-junction OPV cells.[7, 49] Figure A. 3 is an example of a four-junction OPV cell that we studied in Chapter 5. As previously discussed, we employed two DBP:C_{70} and DTDCTB:C_{60} PM-HJs in the four-junction structure to harvest photons at both the first and second optical maxima. As shown in Fig. A. 3(b) and (c), two DBP:C_{70} sub-cells have large spectral overlaps in the optical field distribution and *EQE* spectra. The DTDCTB:C_{60} sub-cells share the same simulation. Therefore, it is difficult to accurately measure the multi-junction OPV cells using the same method for multi-junction inorganic solar cells. Here we develop a method using a combination of modeling and experiment to measure the device performance of multi-junction OPV cells.
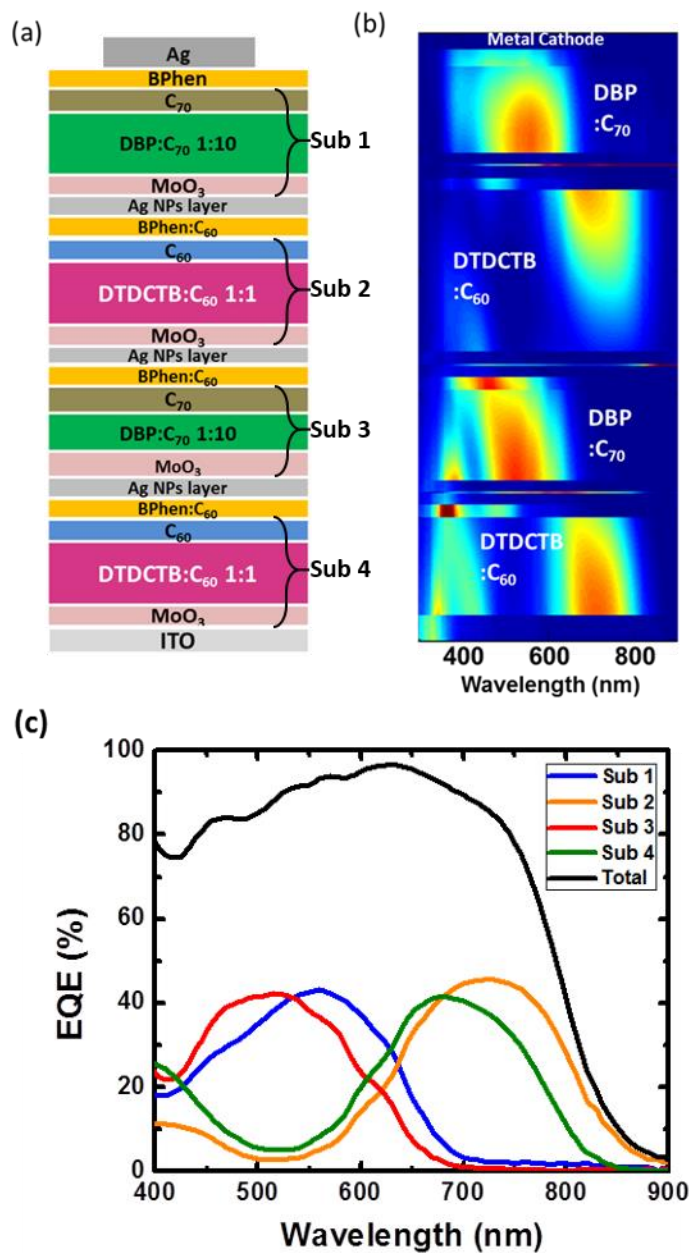
Figure A.3 (a) Schematics of a four-junction OPV cell; (b) Optical power distribution inside the four-junction cell; (c) Calculated *EQE* spectra of sub-cells inside the four-junction structure.

The process flow of the multi-junction OPV measurement is shown in Fig. A. 4. Input parameters include: (a) layer structures of multi-junction cells; (b) optical constants of all the layers; (c) exciton diffusion lengths of organic photoactive layers; (d) *J-V* characteristics of

single-cells under illumination at different light intensities; (e) source spectrum (AM 1.5G or solar simulator).

Input: layer structure of multi-junction cell; optical constants of each layer; exciton diffusion length; single-cell *I-V* under different light intensities; source spectrum (AM 1.5 G or solar simulator)	Calculate optical field distribution inside the multi-junction structure using transfer matrix method
Calculate *EQE* and J_{SC} of each sub-cell in the multi-junction cell under the illumination of light sources (AM 1.5G or solar simulator)	Calculate exciton distribution profiles of organic photoactive regions for each sub-cell
Calculate *I-V* characteristics of each sub-cell by interpolating *I-V* characteristics of single cells under different intensities	Calculate *I-V* characteristics of multi-junction cells based on *I-V* of each sub-cell and compute device parameters of the multi-junction cells

Figure A.4 Process flow chart of the multi-junction OPV modeling.

First, optical field distribution inside the multi-junction cell is calculated using the transfer matrix method[2, 60]. From this, exciton distribution profiles in the organic photoactive regions are calculated using the exciton diffusion model[2], and then *EQE* and J_{SC} of each sub-cell in the multi-junction structure are calculated accordingly. Next, the *J-V* characteristics of each sub-cell inside the multi-junction cell are interpolated from the measured single-cell *J-V* characteristics under the illumination at various light intensities. Finally, the *J-V* characteristics of the multi-junction cell is calculated by adding up the voltage of each sub-cell at every current

value so that each sub-cell generates the same photocurrent in the circuit. The device parameters

of the multi-junction cells are computed from the modeled *J-V* characteristics. The mismatch

factor (*M*) for the multi-junction cell is calculated as the ratio of η_p calculated using the solar

simulator spectrum and that using AM 1.5G as illumination sources.
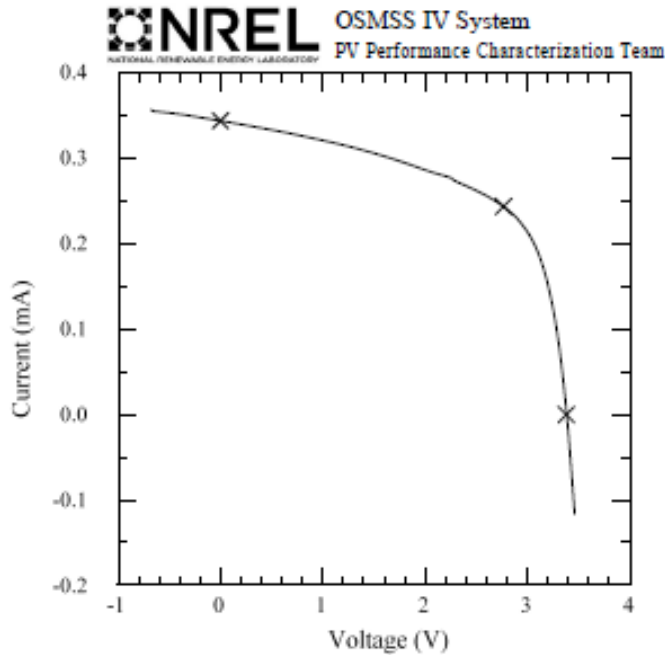
Figure A.5 *I-V* characteristics of a four-junction OPV cell measured by NREL. Courtesy of Tom Moriarty.

Table A.1 Comparison of device parameters for the same four-junction OPV cell measured in our lab and NREL

	J_{SC} (mA/cm^2)	V_{OC} (V)	FF (%)	η_p (%)
Our lab*	4.91	3.38	57.8	9.6
NREL	4.78	3.38	57.8	9.4

* Spectrally corrected using the method described above

To test the feasibility of our method, we measured a four-junction OPV cell as shown in Fig. A. 3(a) using the method described above. In addition, we sent the same device to NREL for the measurement using their newly built one-sun multi-source solar simulator. The *I-V* characteristics is shown in Fig. A. 5 with device parameters summarized in Table A. 1. We can see that device parameters of the same device measured in two labs are very close with a difference of 2% in J_{SC} and η_p which is likely due to the degradation during the device transportation.

To sum up, we demonstrated a method to accurately measure multi-junction OPV cells with no requirement of expensive and complicated multi-source solar simulators. We believe that this method should be useful for the further development of multi-junction OPV cells in the future.

List of Publications, Patents and Conference Presentations

Publications

1. X. Xiao, K. Lee and S. R. Forrest, 'Inverted, Semitransparent Small Molecule Photovoltaic Cells', submitted to Appl. Phys. Lett.

2. X. Xiao, K. Lee and S. R. Forrest, 'Scalability of Multi-junction Organic Solar Cells for Large Area Organic Solar Modules', Appl. Phys. Lett. **106**, 213301 (2015).

3. X. Xiao, K. J. Bergemann, J. D. Zimmerman, K. Lee and S. R. Forrest, 'Small Molecule Planar-mixed Heterojunction Photovoltaic Cell with A Fullerene-based Electron Filtering Buffer', Adv. Energy Mater. **4**, 1301557 (2014).

4. X. Che, X. Xiao, J. D. Zimmerman, D. Fan and S. R. Forrest, 'High-Efficiency, Vacuum-Deposited, Small Molecule Organic Tandem and Triple-Junction Photovoltaic Cells', Adv. Energy Mater. **4**, 1400568 (2014).

5. X. Xiao, J. D. Zimmerman, B. E. Lassiter, K. J. Bergemann and S. R. Forrest, 'A Hybrid Planar-mixed Tetraphenyldibenzoperiflanthene/C_{70} Photovoltaic Cell', Appl. Phys. Lett. **102**, 073302 (2013).

6. J. D. Zimmerman, B. E. Lassiter, X. Xiao, K. Sun, A. Dolocan, R. Gearba, D. A. V. Bout, K. J. Stevenson, P. Wickramasinghe, M. E. Thompson and S. R. Forrest, 'Control of Interface

Order by Inverse Quasi-Epitaxial Growth of Squaraine/Fullerene Thin Film Photovoltaics', ACS Nano **7**, 9268 (2013).

7. X. Xiao, G. Wei, S. Wang, J. D. Zimmerman, C. K. Renshaw, M. E. Thompson and S. R. Forrest, 'Small-Molecule Photovoltaics Based on Functionalized Squaraine Donor Blends', Adv. Mater. **24**, 1956 (2012).

8. J. D. Zimmerman, X. Xiao, C. K. Renshaw, S. Wang, V. V. Diev, M. E. Thompson and S. R. Forrest, 'Independent Control of Bulk and Interfacial Morphologies of Small Molecular Weight Organic Heterojunction Solar Cells', Nano Lett. **12**, 4366 (2012).

9. G. Wei, X. Xiao, S. Wang, K. Sun, K. J. Bergemann, M. E. Thompson and S. R. Forrest, 'Functionalized Squaraine Donors for Nanocrystalline Organic Photovoltaics', ACS Nano **6**, 972 (2012).

10. K. Lee, J. D. Zimmerman, X. Xiao, K. Sun and S. R. Forrest, 'Reuse of GaAs Substrates for Epitaxial Lift-off by Employing Protection Layers', J. Appl. Phys. **111**, 033527 (2012).

11. B. E. Lassiter, J. D. Zimmerman, A. Panda, X. Xiao and S. R Forrest, 'Tandem Organic Photovoltaics Using Both Solution and Vacuum Deposited Small Molecules', Appl. Phys. Lett. **101**, 063303 (2012).

12. N. Wang, J. D. Zimmerman, X. Tong, X. Xiao and S. R. Forrest, 'Snow Cleaning of Substrates Increases Yield of Large-area Organic Photovoltaics', Appl. Phys. Lett. **101**, 133901 (2012).

13. G. Wei, X. Xiao, S. Wang, J. D. Zimmerman, K. Sun, V. V. Diev, M. E. Thompson and S. R. Forrest, 'Arylamine-Based Squaraine Donors for Use in Nanocrystalline Organic Solar Cells', Nano Lett. **11**, 4261 (2011).

14. S. Wang, L. Hall, V. V. Diev, R. Haiges, G. Wei, X. Xiao, P. I. Djurovich, S. R. Forrest and M. E. Thompson, 'N,N-Diarylanilinosquaraines and Their Application to Organic Photovoltaics', Chem. Mater. **23**, 4789 (2011).

15. N. Li, K. Lee, C. K. Renshaw, X. Xiao and S. R. Forrest, 'Improved Power Conversion Efficiency of InP Solar Cells Using Organic Window Layers', Appl. Phys. Lett. **98**, 053504 (2011).

Patents

1. S. R. Forrest, M. E. Thompson, G. Wei, S. Wang, L. Hall, V. V. Diev, X. Xiao, 'Organic Photosensitive Devices comprising Aryl Squaraines and Methods of Making the Same', WO 2012109232 A2 (Aug. 2012).

2. S. R. Forrest, J. D. Zimmerman, X. Xiao, 'Hybrid Planar-Mixed Heterojunction for Organic Photovoltaics', WO 2014082006 A1 (May 2014).

3. S. R. Forrest, J. D. Zimmerman, X. Xiao, B. E. Lassiter, 'Hybrid Planar-Graded Heterojunction for Organic Photovoltaics', WO 2014085639 A1 (Jun. 2014).

4. S. R. Forrest, J. D. Zimmerman, B. E. Lassiter, X. Xiao, 'Use of Inverse Quasi-Epitaxy to Modify Order during Post-deposition Processing for Organic Photovoltaics', WO 2014082002 A3 (Jul. 2014).

Conference Presentations

1. X. Xiao, G. Wei, S. Wang, C. K. Renshaw, L. Hall, V. V. Diev, M. E. Thompson and S. R. Forrest, 'New Squaraine Donors for High Efficiency Small Molecule Solar Cells', *37th IEEE Photovoltaic Specialists Conference (PVSC)*, Seattle, WA (Jun. 2011).

2. X. Xiao, G. Wei, S. Wang, J. D. Zimmerman, M. E. Thompson and Stephen R. Forrest, 'High Efficiency Small Molecule Solar Cells based on Blending Two Squaraine Donors', *MRS 2011 Fall meeting*, Boston, MA (Nov. 2011).

3. X. Xiao, G. Wei, J. D. Zimmerman, S. Wang, M. E. Thompson and S. R. Forrest, 'Functionalized Squaraine Donors for Nanocrystalline Small Molecule Photovoltaics', *MRS 2012 Spring meeting*, San Francisco, CA (Apr. 2012).

4. X. Xiao**,** B. E. Lassiter, J. D. Zimmerman and S. R. Forrest, 'Small Molecular Weight SubPc:C_{70} Graded Heterojunction Photovoltaics'**,** *MRS 2012 Fall meeting*, Boston, MA (Nov. 2012).

5. X. Xiao, B. E. Lassiter, J. D. Zimmerman and S. R. Forrest, 'High Efficiency Tandem Organic Photovoltaics incorporating Small Molecule Blended Squaraine Donors and A Fullerene Acceptor', *39th IEEE Photovoltaic Specialists Conference (PVSC)*, Tampa, FL (Jun. 2013).

6. X. Xiao, J. D. Zimmerman, B. E. Lassiter, K. J. Bergemann and S. R. Forrest, 'A Hybrid Planar-mixed Tetraphenyldibenzoperiflanthene/C_{70} Photovoltaic Cell'**,** *MRS 2013 Fall meeting*, Boston, MA (Dec. 2013).

7. X. Xiao, K. Lee and S. R. Forrest, 'Area Scaling of Multi-junction Organic Photovoltaic Cells', *MRS 2015 Spring meeting*, San Francisco, CA (Apr. 2015).

BIBILOGRAPHY

[1] C.W. Tang, Appl. Phys. Lett. **48**, 183 (1986).

[2] P. Peumans, A. Yakimov, and S.R. Forrest, J. Appl. Phys. **95**, 2938 (2004).

[3] Y.Z. Lin, Y.F. Li, and X.W. Zhan, Chem. Soc. Rev. **41**, 4245 (2012).

[4] A.W. Hains, Z.Q. Liang, M.A. Woodhouse, and B.A. Gregg, Chem. Rev. **110**, 6689 (2010).

[5] A. Mishra and P. Bauerle, Angew. Chem. Int. Edit. **51**, 2020 (2012).

[6] G. Li, R. Zhu, and Y. Yang, Nat. Photonics **6**, 153 (2012).

[7] X. Che, X. Xiao, J.D. Zimmerman, F. D.*, et al.*, Adv. Energy Mater. **4**, 1400568 (2014).

[8] Z.C. He, B. Xiao, F. Liu, H.B. Wu, *et al.*, Nat. Photonics **9**, 174 (2015).

[9] J.B. You, L.T. Dou, K. Yoshimura, T. Kato, *et al.*, Nat. Comm. **4**, 1446 (2013).

[10] C.C. Chen, W.H. Chang, K. Yoshimura, K. Ohya, *et al.*, Adv. Mater. **26**, 5670 (2014).

[11] A.B. Yusoff, D. Kim, H.P. Kim, F.K. Shneider, *et al.*, Energ. Environ. Sci. **8**, 303 (2015).

[12] C.H. Peters, I.T. Sachs-Quintana, J.P. Kastrop, S. Beaupre, *et al.*, Adv. Energy Mater. **1**, 491 (2011).

[13] C. Lungenschmied, G. Dennler, H. Neugebauer, S.N. Sariciftci, *et al.*, Sols Energ. Mat. Sol. Cell **91**, 379 (2007).

[14] J. Kong, S. Song, M. Yoo, G.Y. Lee, *et al.*, Nat. Commun. **5**, 5688 (2014).

[15] Q. Burlingame, X.R. Tong, J. Hankett, M. Slootsky, *et al.*, Energ. Environ. Sci. **8**, 1005 (2015).

[16] M. Jorgensen, K. Norrman, and F.C. Krebs, Sols Energ. Mat. Sol. Cell **92**, 686 (2008).

[17] F.C. Krebs, N. Espinosa, M. Hosel, R.R. Sondergaard, *et al.*, Adv. Mater. **26**, 29 (2014).

[18] H. Jin, C. Tao, M. Velusamy, M. Aljada, *et al.*, Adv. Mater. **24**, 2572 (2012).

[19] S.K. Choi, Y.H. Zhou, W. Haske, J.W. Shim, *et al.*, Org. Electron. **17**, 349 (2015).

[20] M. Pope and C.E. Swenberg, *Electronic Processes in Organic Crystals and Polymers*. Oxford University Press, New York, 1999.

[21] S.R. Forrest, MRS Bull. **30**, 28 (2005).

[22] G. Yu, J. Gao, J.C. Hummelen, F. Wudl, *et al.*, Science **270**, 1789 (1995).

[23] S.M. Sze and K.K. Ng, *Physics of Semiconductor Devices*. Wiley-Interscience, Hoboken, New Jersey, 2006.

[24] N.C. Giebink, G.P. Wiederrecht, M.R. Wasielewski, and S.R. Forrest, Phys. Rev. B **82**, 155305 (2010).

[25] N.C. Giebink, B.E. Lassiter, G.P. Wiederrecht, M.R. Wasielewski, *et al.*, Phys. Rev. B **82**, 155306 (2010).

[26] G.D. Wei, X. Xiao, S.Y. Wang, J.D. Zimmerman, *et al.*, Nano Lett. **11**, 4261 (2011).

[27] J.D. Zimmerman, X. Xiao, C.K. Renshaw, S.Y. Wang, *et al.*, Nano Lett. **12**, 4366 (2012).

[28] J.G. Xue, B.P. Rand, S. Uchida, and S.R. Forrest, Adv. Mater. **17**, 66 (2005).

[29] R. Pandey and R.J. Holmes, Adv. Mater. **22**, 5301 (2010).

[30] P. Peumans, V. Bulovic, and S.R. Forrest, Appl. Phys. Lett. **76**, 2650 (2000).

[31] B.P. Rand, J. Li, J.G. Xue, R.J. Holmes, *et al.*, Adv. Mater. **17**, 2714 (2005).

[32] B.E. Lassiter, G.D. Wei, S.Y. Wang, J.D. Zimmerman, *et al.*, Appl. Phys. Lett. **98**, 243307 (2011).

[33] M. Hirade and C. Adachi, Appl. Phys. Lett. **99**, 153302 (2011).

[34] D. Fujishima, H. Kanno, T. Kinoshita, E. Maruyama, *et al.*, Sol Energ Mat Sol C **93**, 1029 (2009).

[35] R. Fitzner, E. Mena-Osteritz, A. Mishra, G. Schulz, *et al.*, J. Am. Chem. Soc. **134**, 11064 (2012).

[36] L.Y. Lin, Y.H. Chen, Z.Y. Huang, H.W. Lin, *et al.*, J. Am. Chem. Soc. **133**, 15822 (2011).

[37] S.W. Chiu, L.Y. Lin, H.W. Lin, Y.H. Chen, *et al.*, Chem. Commun. **48**, 1857 (2012).

[38] Y.M. Sun, G.C. Welch, W.L. Leong, C.J. Takacs, *et al.*, Nat. Mater. **11**, 44 (2012).

[39] A.K.K. Kyaw, D.H. Wang, V. Gupta, W.L. Leong, *et al.*, Acs Nano **7**, 4569 (2013).

[40] A.K.K. Kyaw, D.H. Wang, D. Wynands, J. Zhang, *et al.*, Nano Lett. **13**, 3796 (2013).

[41] Z. Li, G.R. He, X.J. Wan, Y.S. Liu, *et al.*, Adv. Energy Mater. **2**, 74 (2012).

[42] Q. Zhang, B. Kan, F. Liu, G.K. Long, *et al.*, Nat. Photonics **9**, 35 (2015).

[43] O.L. Griffith and S.R. Forrest, Nano Lett. **14**, 2353 (2014).

[44] K. Cnops, B.P. Rand, D. Cheyns, B. Verreet, *et al.*, Nat. Commun. **5**, 3406 (2014).

[45] D. Cheyns, B.P. Rand, and P. Heremans, Appl. Phys. Lett. **97**, 033301 (2010).

[46] M. Riede, C. Uhrich, J. Widmer, R. Timmreck, *et al.*, Adv. Funct. Mater. **21**, 3019 (2011).

[47] B.E. Lassiter, J.D. Zimmerman, and S.R. Forrest, Appl. Phys. Lett. **103**, 123305 (2013).

[48] Y.S. Liu, C.C. Chen, Z.R. Hong, J. Gao, *et al.*, Sci. Rep. **3**, 3356 (2013).

[49] R. Meerheim, C. Korner, and K. Leo, Appl. Phys. Lett. **105**, 063306 (2014).

[50] T.S. van der Poll, J.A. Love, T.Q. Nguyen, and G.C. Bazan, Adv. Mater. **24**, 3646 (2012).

[51]   D. Yokoyama, Z.Q. Wang, Y.J. Pu, K. Kobayashi*, et al.*, Sol. Energ. Mat. Sol. C. **98**, 472 (2012).

[52]   K.J. Bergemann and S.R. Forrest, Appl. Phys. Lett. **99**, 243303 (2011).

[53]   S. Pfuetzner, J. Meiss, A. Petrich, M. Riede*, et al.*, Appl. Phys. Lett. **94**, 223307 (2009).

[54]   N. Li, B.E. Lassiter, R.R. Lunt, G. Wei*, et al.*, Appl. Phys. Lett. **94**, 023307 (2009).

[55]   Y.M. Sun, C.J. Takacs, S.R. Cowan, J.H. Seo*, et al.*, Adv. Mater. **23** (2011).

[56]   J. Meyer, S. Hamwi, M. Kroger, W. Kowalsky*, et al.*, Adv. Mater. **24**, 5408 (2012).

[57]   A.K.K. Kyaw, X.W. Sun, C.Y. Jiang, G.Q. Lo*, et al.*, Appl. Phys. Lett. **93**, 221107 (2008).

[58]   D.W. Zhao, P. Liu, X.W. Sun, S.T. Tan*, et al.*, Appl. Phys. Lett. **95**, 153304 (2009).

[59]   D.W. Zhao, X.W. Sun, C.Y. Jiang, A.K.K. Kyaw*, et al.*, Appl. Phys. Lett. **93**, 083305 (2008).

[60]   L.A.A. Pettersson, L.S. Roman, and O. Inganas, J. Appl. Phys. **86**, 487 (1999).

[61]   B.E. Lassiter, J.D. Zimmerman, A. Panda, X. Xiao*, et al.*, Appl. Phys. Lett. **101**, 063303 (2012).

[62]   G. Chen, H. Sasabe, Z.Q. Wang, X.F. Wang*, et al.*, Adv. Mater. **24**, 2768 (2012).

[63]   R. Pandey, A.A. Gunawan, K.A. Mkhoyan, and R.J. Holmes, Adv. Funct. Mater. **22**, 617 (2012).

[64]   M.L. Zhang, H. Wang, H.K. Tian, Y.H. Geng*, et al.*, Adv. Mater. **23**, 4960 (2011).

[65]   P. Peumans and S.R. Forrest, Chem. Phys. Lett. **398**, 27 (2004).

[66]   M.Y. Chan, C.S. Lee, S.L. Lai, M.K. Fung*, et al.*, J. Appl. Phys. **100**, 094506 (2006).

[67]   X. Xiao, J.D. Zimmerman, B.E. Lassiter, K.J. Bergemann*, et al.*, Appl. Phys. Lett. **102**, 073302 (2013).

[68]   A.K.K. Kyaw, D.H. Wang, V. Gupta, J. Zhang*, et al.*, Adv. Mater. **25** (2013).

[69]   L.J.A. Koster, V.D. Mihailetchi, and P.W.M. Blom, Appl. Phys. Lett. **88**, 052104 (2006).

[70]   B. Verreet, P.E. Malinowski, B. Niesen, D. Cheyns*, et al.*, Appl. Phys. Lett. **102**, 043301 (2013).

[71]   J.M. Hodgkiss, S. Albert-Seifried, A. Rao, A.J. Barker*, et al.*, Adv. Funct. Mater. **22**, 1567 (2012).

[72]   A.N. Bartynski, C. Trinh, A. Panda, K. Bergemann*, et al.*, Nano Lett. **13**, 3315 (2013).

[73]   A. Miller and E. Abrahams, Phys. Rev. **120**, 745 (1960).

[74]   H. Bassler, Phys. Status Solidi B-Basic Res. **175**, 15 (1993).

[75]   I.I. Fishchuk, D. Hertel, H. Bässler, and A.K. Kadashchuk, Phys. Rev. B **65** (2002).

[76]   A.B. Walker, A. Kambili, and S.J. Martin, J. Phys.: Condens. Matter **14**, 9825 (2002).

[77]   U. Wolf, V.I. Arkhipov, and H. Bässler, Phys. Rev. B **59**, 7507 (1999).

[78]   B.P. Rand, J.G. Xue, S. Uchida, and S.R. Forrest, J. Appl. Phys. **98**, 124902 (2005).

[79]   M.A. Khan, W. Xu, Khizar-ul-Haq, Y. Bai*, et al.*, J. Appl. Phys. **103**, 014509 (2008).

[80]   P. Peumans and S.R. Forrest, Appl. Phys. Lett. **79**, 126 (2001).

[81]   K.J. Bergemann and S.R. Forrest, Appl. Phys. Lett. **99**, 243303 (2011).

[82]   C.H. Seaman, Sol Energy **29**, 291 (1982).

[83]   S.H. Wang, T. Sakurai, R. Kuroda, and K. Akimoto, Appl. Phys. Lett. **100**, 243301 (2012).

[84]   J.X. Tang, Y.C. Zhou, Z.T. Liu, C.S. Lee*, et al.*, Appl. Phys. Lett. **93**, 043512 (2008).

[85]   H.Y. Chen, J.H. Hou, S.Q. Zhang, Y.Y. Liang*, et al.*, Nat. Photonics **3**, 649 (2009).

[86]   H.X. Shang, H.J. Fan, Y. Liu, W.P. Hu*, et al.*, Adv. Mater. **23**, 1554 (2011).

[87]   G.D. Wei, S.Y. Wang, K. Sun, M.E. Thompson*, et al.*, Adv. Energy Mater. **1**, 184 (2011).

[88]   G.D. Wei, R.R. Lunt, K. Sun, S.Y. Wang*, et al.*, Nano Lett. **10**, 3555 (2010).

[89]   S.Y. Wang, E.I. Mayo, M.D. Perez, L. Griffe, *et al.*, Appl. Phys. Lett. **94**, 233304 (2009).

[90]   G.D. Wei, S.Y. Wang, K. Renshaw, M.E. Thompson, *et al.*, ACS Nano **4**, 1927 (2010).

[91]   B.E. Lassiter, G.D. Wei, S.Y. Wang, J.D. Zimmerman, *et al.*, Appl. Phys. Lett. **98**, 243307 (2011).

[92]   N.C. Giebink, G.P. Wiederrecht, M.R. Wasielewski, and S.R. Forrest, Phys. Rev. B **83**, 195326 (2011).

[93]   P. Peumans, S. Uchida, and S.R. Forrest, Nature **425**, 158 (2003).

[94]   V. Shrotriya, G. Li, Y. Yao, T. Moriarty, *et al.*, Adv. Funct. Mater. **16**, 2016 (2006).

[95]   B.P. Rand, D.P. Burk, and S.R. Forrest, Phys. Rev. B **75**, 115327 (2007).

[96]   K.L. Mutolo, E.I. Mayo, B.P. Rand, S.R. Forrest, *et al.*, J. Am. Chem. Soc. **128**, 8108 (2006).

[97]   N.C. Giebink, G.P. Wiederrecht, M.R. Wasielewski, and S.R. Forrest, Phys. Rev. B **82**, 155305 (2010).

[98]   R.R. Lunt, J.B. Benziger, and S.R. Forrest, Adv. Mater. **22**, 1233 (2010).

[99]   N.C. Giebink, B.E. Lassiter, G.P. Wiederrecht, M.R. Wasielewski, *et al.*, Phys. Rev. B **82**, 155306 (2010).

[100]   B.E. Lassiter, C.K. Renshaw, and S.R. Forrest, J. Appl. Phys. **113**, 214505 (2013).

[101]   N. Li, B.E. Lassiter, R.R. Lunt, G. Wei, *et al.*, Appl. Phys. Lett. **94** (2009).

[102]   M.Y. Chan, C.S. Lee, S.L. Lai, M.K. Fung, *et al.*, J. Appl. Phys. **100** (2006).

[103]   A.N. Bartynski, C. Trinh, A. Panda, K. Bergemann, *et al.*, Nano Lett. **13** (2013).

[104]   C. Trinh, K.O. Kirlikovali, A.N. Bartynski, C.J. Tassone, *et al.*, J. Am. Chem. Soc. **135** (2013).

[105]   D. Cheyns, M. Kim, B. Verreet, and B.P. Rand, Appl. Phys. Lett. **104** (2014).

[106] J.D. Zimmerman, B.E. Lassiter, X. Xiao, K. Sun, *et al.*, ACS Nano **7** (2013).

[107] Y. Liu, C.-C. Chen, Z. Hong, J. Gao, *et al.*, Sci. Rep. **3** (2013).

[108] R.F. Bailey-Salzman, B.P. Rand, and S.R. Forrest, Appl. Phys. Lett. **88**, 233502 (2006).

[109] R.R. Lunt and V. Bulovic, Appl. Phys. Lett. **98**, 113305 (2011).

[110] R. Betancur, P. Romero-Gomez, A. Martinez-Otero, X. Elias, *et al.*, Nat. Photonics **7**, 995 (2013).

[111] C.Y. Chang, L.J. Zuo, H.L. Yip, C.Z. Li, *et al.*, Adv. Energy Mater. **4**, 1301645 (2014).

[112] J.Y. Lee, S.T. Connor, Y. Cui, and P. Peumans, Nano Lett. **10**, 1276 (2010).

[113] F. Guo, X.D. Zhu, K. Forberich, J. Krantz, *et al.*, Adv. Energy Mater. **3**, 1062 (2013).

[114] H.W. Lin, Y.H. Chen, Z.Y. Huang, C.W. Chen, *et al.*, Org. Electron. **13**, 1722 (2012).

[115] H. Schmidt, T. Winkler, M. Tilgner, H. Flugge, *et al.*, Proc Spie **7416**, 741611 (2009).

[116] C.C. Chen, L.T. Dou, R. Zhu, C.H. Chung, *et al.*, ACS Nano **6**, 7185 (2012).

[117] C.C. Chen, L.T. Dou, J. Gao, W.H. Chang, *et al.*, Energy Environ. Sci. **6**, 2714 (2013).

[118] S. Salam, M. Islam, and A. Akram, Thin Solid Films **529** (2013).

[119] J. Meiss, T. Menke, K. Leo, C. Uhrich, *et al.*, Appl. Phys. Lett. **99**, 043301 (2011).

[120] S. Schubert, L. Muller-Meskamp, and K. Leo, Adv Funct Mater **24**, 6668 (2014).

[121] B.E. Lassiter, J.D. Zimmerman, A. Panda, X. Xiao, *et al.*, Appl. Phys. Lett. **101**, 063303 (2012).

[122] X. Xiao, J.D. Zimmerman, B.E. Lassiter, K.J. Bergemann, *et al.*, Appl. Phys. Lett. **102**, 073302 (2013).

[123] W.W. Li, A. Furlan, K.H. Hendriks, M.M. Wienk, *et al.*, J. Am. Chem. Soc. **135**, 5529 (2013).

[124] S. Choi, W.J. Potscavage, and B. Kippelen, J. Appl. Phys. **106**, 054507 (2009).

[125]   W.I. Jeong, J. Lee, S.Y. Park, J.W. Kang, *et al.*, Adv. Funct. Mater. **21**, 343 (2011).

[126]   J.D. Servaites, S. Yeganeh, T.J. Marks, and M.A. Ratner, Adv. Funct. Mater. **20**, 97 (2010).

[127]   A. Manor, E.A. Katz, T. Tromholt, B. Hirsch, *et al.*, J. Appl. Phys. **109**, 074508 (2011).

[128]   A.K. Pandey, J.M. Nunzi, B. Ratier, and A. Moliton, Phys. Lett. A **372**, 1333 (2008).

[129]   N.N. Wang, J.D. Zimmerman, X.R. Tong, X. Xiao, *et al.*, Appl. Phys. Lett. **101**, 133901 (2012).

[130]   B.P. Rand, D.P. Burk, and S.R. Forrest, Phys. Rev. B **75**, 115327 (2007).

[131]   S.Y. Park, W.I. Jeong, D.G. Kim, J.K. Kim, *et al.*, Appl. Phys. Lett. **96**, 173301 (2010).

[132]   Y.Q. Zheng, W.J. Potscavage, T. Komino, and C. Adachi, Appl. Phys. Lett. **102**, 153302 (2013).

[133]   Y.H. Chen, L.Y. Lin, C.W. Lu, F. Lin, *et al.*, J. Am. Chem. Soc. **134**, 13616 (2012).

[134]   A. Yakimov and S.R. Forrest, Appl. Phys. Lett. **80**, 1667 (2002).

[135]   B.P. Rand, P. Peumans, and S.R. Forrest, J. Appl. Phys. **96**, 7519 (2004).

[136]   X.H. Li, W.C.H. Choy, L.J. Huo, F.X. Xie, *et al.*, Adv. Mater. **24**, 3046 (2012).

[137]   K. Jung, H.J. Song, G. Lee, Y. Ko, *et al.*, ACS Nano **8**, 2590 (2014).

[138]   L.Y. Lu, Z.Q. Luo, T. Xu, and L.P. Yu, Nano Lett. **13**, 59 (2013).

[139]   D.M. O'Carroll, C.E. Hofmann, and H.A. Atwater, Adv. Mater. **22**, 1223 (2010).

[140]   B. Niesen, B.P. Rand, P. Van Dorpe, D. Cheyns, *et al.*, Adv. Energy Mater. **3**, 145 (2013).

[141]   J.D. Zimmerman, B. Song, O. Griffith, and S.R. Forrest, Appl. Phys. Lett. **103**, 243905 (2013).

[142]   C.H. Seaman, Sol. Energy **29**, 291 (1982).

[143] G.F. Virshup, *IEEE Photovoltaic Specialists Conference (PVSC),* **2**, 1249 (1990).

[144]   T. Moriarty, J. Jablonski, and K. Emery, *IEEE Photovoltaic Specialists Conference (PVSC),*1291 (2012).